Novel X-Ray Imaging Detectors

THE UNIVERSITY
of LIVERPOOL

Thesis submitted in accordance with the requirements of the University
of Liverpool for the degree of Doctor of Philosophy

by

Dominic Mark Duxbury

September 1997

Oliver Lodge Laboratory
University of Liverpool

Abstract

With the advent of the latest third generation synchrotron radiation sources it has become apparent that there is a considerable mismatch between the fluxes provided by the storage rings and the ability of x-ray detection systems to exploit them. This led to a European workshop on x-ray detectors for synchrotron radiation in 1991, which highlighted specific problems both for the detector and the readout system.

This thesis describes four different x-ray detectors which have been proposed as likely candidates to overcome some of the problems noted at the above mentioned workshop

In the first instance a detector is described which it is hoped will alleviate some of the problems associated with the parallax problem. Initial tests, performed at the Daresbury laboratory, with this detector are described and encouraging results have been obtained.

The remainder of this thesis then focuses on detectors based on the microstrip gas avalanche chamber (MSGC). Laboratory tests performed at Liverpool have focused on the high rate and ageing capabilities of these devices.

The imaging properties of these detectors have been tested using the multiwire linear (MWL) readout system at the Daresbury laboratory and have been compared to those obtained with a similar device, the microgap chamber (MGAP).

Finally a new detector is introduced, the microdot chamber (MDOT), which proves itself to be superior to the MSGC and MGAP and which has attracted great interest from detector scientists throughout the world.

Acknowledgements

There are many people that I would like to thank for their help and support during the course of my study. Prof. Erwin Gabathuler for giving me the opportunity and to my supervisor Prof. Joan Bordas for some very interesting discussions about politics, life and my research work. I am indebted to Drs. Stephen Biagi and Tim Jones at Liverpool and to Drs. Rob Lewis and Chris Hall at Daresbury for their day to day advice on all aspects of my work and for their patient handling of my ignorance. Its been a pleasure working with them. I would also like to thank the BBSRC for their financial support and the Daresbury laboratory for sponsoring me.

I am also grateful to the technical staff at both laboratories for helping me out on numerous occasions. In particular Andy Jones and Bill Helsby at Daresbury and Ted Orme, Ashley Greenhall and Dave Seddon at Liverpool. A very special thanks to Mike Wormald and Uncle Dave Muskett, both at Liverpool, for keeping me sane throughout my time spent there, and who I consider to be friends as opposed to technicians.

I would like to thank all my friends at Liverpool, as they've come and gone and in particular Mark Smith, Stuart Cocks, Chris Cormack, Balloni Galloni, Dave Milstead, Julia Davies, Danny le Hill, Ali Sheridan and Martin, Rog and James from NS. Without these and the Oxford I would have had no social life whatsoever.

Advances in physics follow advances in instrumentation
once the instruments are made, many people will make the discoveries.

- Abraham Pais,
Inward bound:
Of Matter and Forces
in the physical world

Contents

Chapter 1

Detectors for Time Resolved Non-Crystalline X-Ray Diffraction

1.1 Introduction

The use of synchrotron radiation as a tool in basic and applied science has grown tremendously over the last few decades. This is all the more remarkable considering the radiation was considered a drain on the energy of electrons in circular accelerators used by the high energy physicists.

Synchrotron radiation (SR) is generated when a highly relativistic charged particle experiences a large centripetal acceleration, as is produced when an electron is accelerated by a magnetic field in the bending magnet of a circular accelerator. SR can also be generated from insertion devices such as wigglers and undulators. These devices are inserted in straight sections of accelerators and produce a localised deflection of the beam trajectory resulting in the emission of SR. Particularly for light particles i.e. electrons or positrons, the emitted radiation has certain properties which make it useful as a scientific tool. These properties include:

1. Broad spectral range
2. High intensity
3. High degree of collimation
4. Linear polarisation
5. High brilliance of source
6. Pulsed time structure

Several of these properties make synchrotron radiation an unrivalled source of x-rays in the field of x-ray diffraction. X-ray diffraction is a technique which is generally thought of as being applied to crystalline substances. However, the technique may also be used in the study of semi-crystalline materials such as connective tissue and polymers. On of the strengths of x-ray diffraction is that it allows study, at the molecular level, of functionally intact samples that are being subjected to external stimuli. Hence, time dependent processes can be followed on a sample which is under conditions very similar to the natural environment of the sample. An example of such work is the study of 'live' muscle contraction [1]. To gain any knowledge from such techniques the scattered x-rays must be efficiently and accurately detected and its this detection process which will form the basis of this thesis.

1.2 Detector categories

A diffraction image consists of a number of scattered peaks of intensity superimposed on background scatter. Therefore only part of the detector will record signals of interest whilst all of the detector will record background. If the image consists of n peaks having an intensity i_s, the background intensity is i_b and the fraction of the incident intensity hitting the detector is s, then

$$sI_o = i_b + ni_s \tag{1.1}$$

where I_o is the incident beam intensity per unit time. If we define $I_b = i_b/A$ as the background intensity per unit area, where A is the detector area and similarly for i_s such that the signal intensity per unit area $I_s = i_s/a$ where a is the area over which the peak spreads, then the ratio of signal to background, r, is

$$I_s = I_b r \text{ and } i_b = {}^{i_s A}\!\big/_{ar} \tag{1.2}$$

If this is now combined with equation 1.1 then

$$\frac{i_s}{I_o} = \frac{ars}{(arn + A)} \tag{1.3}$$

which is the fraction of the incident intensity in a single peak. A survey of non-crystalline diffraction experiments on the Daresbury Synchrotron Radiation Source (SRS) [2], leads to the following typical values for the parameters in 1.3. Detector area $A = 4 \times 10^4 mm^2$, typical area of a peak $a = 8mm^2$, number of peaks $n = 10$, sample scattering power $s = 10^{-4}$ and the ratio of signal to background for a relatively weak peak $r = 5$. This tells us that only $\sim 10^{-7}$ of the incident flux goes into a single peak in the pattern. In other words an incident flux of 10^{11} photons s^{-1} is needed in order to measure a single peak to a 1% accuracy in a 1 second exposure. Such flux levels are firmly in the domain of SR sources. Flux levels of the order of 10^{14} photons per second per square mm are thus required for single shot measurements for millisecond time resolution to be achieved, which is currently at the limit of the very latest storage rings with insertion devices. If however, the detector and detection system can be framed and providing the experiment under study can be reliably repeated then the experiment can be strobed to yield the required resolution. All detectors used for such experiments fall into one of two categories which operate in different ways. These are integrating detectors and photon counting detectors.

1.2.1 Photon counting detectors

Photon counting detectors are digital devices which are capable of distinguishing between individual x-rays. They have some form of mechanism which enables them to locate each x-ray, during which at least some part of the detector will become insensitive to the detection of further x-rays. This deadtime thus sets a limit to the rate at which the detector can record x-ray photons. In the case of photon counting detectors it is the rate of arrival of x-rays which sets an upper limit to the intensity of exposure. The minimum detectable flux is set by the dark noise of the detector. In photon counting detectors this is generally very low. Because each photon is detected upon arrival, no inter frame readout time is required thus making their use in time resolved studies viable.

1.2.2 Integrating detectors

Integrating detectors are the most common type of detector in everyday use on SR diffraction experiments. As their name implies, integrating detectors integrate the amount of x-ray flux recorded at each location within the detector during some exposure time. This is achieved by measuring some quantity which changes in a well determined way when exposed to x-rays. For example in the case of a phosphor imaging plate it is the number of F centres created in the phosphor. These are metastable states created in the phosphor and a more detailed description will be given in section 1.4. This induced effect varies from photon to photon and this variance exhibits itself as noise, and is mostly evident for low fluxes. Noise is also introduced during the measurement of the induced effect. Again for a phosphor imaging plate, the number of F centres is indirectly implied from the measurement of the amount of blue luminescence induced by scanning the phosphor with a laser beam. Dark noise is inherent to all detectors and is the variation in signal whilst a detector is readout when no input flux is present. This varies greatly from detector to detector. The combination of these contributions is a noise level below which x-rays will not be detected. At the far end of the scale, integrating detectors are limited by their saturation level. Integrating detectors are completely insensitive to the instantaneous rate at which they are exposed and they can therefore handle enormous rates, provided that the saturation level is not exceeded. Once the detector has been exposed however, the readout cycle may take a considerable amount of time. Some examples of integrating detectors are x-ray film, CCDs and image plates.

1.3 Detector requirements

Table 1.1 (taken from [3]) gives a list of detector properties which an ideal detector would satisfy for use on diffraction experiments. The basic requirements specifically for time resolved diffraction will be set out in the following sections.

Resolution	$250\mu m \times 250\mu m$
Number of pixels	1800×1800
Global count rate	$10^8 s^{-1}$
Local count rate	$5 \times 10^5 s^{-1} mm^{-2}$
Dynamic range	$> 10^6$
Stability/Reproducibility	$10^{-3} ... 10^{-2} h^{-1}$
Sensitivity	$1 photon / pixel$
Number of frames	256
Number of cycles	1000
Frame rate	$10^5 s^{-1}$
Energy range	$2...35 keV$
Typical energy	$10 keV$
Energy resolution $\Delta E/E$	20%

Table 1.1: Guideline specifications for diffraction experiments

The detection efficiency of the detector should be as close to 100% as possible but an efficiency of about 80% is acceptable in most cases although for many experimenters it is often less. The stability/reproducibility quoted infers that the detector characteristics should not change by more than 1 to 0.1 % per hour of operational running which ultimately sets an upper limit on the detector lifetime. The number of frames, cycles and the frame rate are governed by the readout system used with the detector.

1.3.1 Size and spatial resolution

Although diffraction is an angular effect the actual size of the detector is quite important. The beams of x-rays used at synchrotrons have finite dimensions so for the majority of diffraction experiments there is little to be gained by having a resolution smaller than the beam size. Large detectors are capable of recording a large range of scattering angles and can also be placed further from the sample thus reducing the background scattering which is inversely proportional to the square of the distance from the sample. This can only be achieved because the scattering peaks of the sample are collimated by the incident beam. The diffraction patterns from non crystalline samples can often be very broad but his does not imply that a poor spatial resolution is acceptable. Although the features may be large, small shifts in their positions can be very significant. A reasonable minimum requirement is that detectors have at least several hundred resolution elements per dimension [2]. The shape of the point spread function (PSF) of a detector is also a crucial characteristic. The PSF of a detector is its response to illumination from an infinitely narrow beam and is related to the detectors position resolution. If this is poor then tails from intense diffraction peaks will mask out less intense features which is obviously detrimental to the experimenter.

1.3.2 Dynamic range

It is quite common for diffraction patterns to consist of intensity peaks which vary in magnitude by as much as 4 decades. For a detector to be useful in time resolved studies it has to be capable of handling such a wide range of intensities on a single frame whilst conserving its linearity over the range. This range is also dependent on the detector PSF for the reason given in section 1.3.1.

1.3.3 Time resolution

The time resolution required for time resolved diffraction studies also varies over many orders of magnitude. In the case of muscle dynamics this can be of the order of microseconds whilst in polymer setting processes it may be over the course of hours or even days. Both categories of detector have different consequences on the time resolution capability. In the case of integrating detectors deadtimes introduced at the end of a frame while the image is transferred. In photon counting devices the deadtime is on a photon by photon basis and so there is no intrinsic frame rate limitation. The required number of frames however can lead to vast amounts of data being produced and it is often computing limitations which determine the time resolution achievable.

1.3.4 Sensitivity

Diffraction from non-crystalline samples can lead to weakly scattered peaks. This means that the detector used must be sensitive to these weak peaks and must posses a very low noise level so as not to mask out the image taken. Also the amount of noise present will affect the exposure time required for an accurate measurement to be made. For instance if a detector has a high noise level then this can be compensated for by exposing the detector for a longer period of time but this can be detrimental to the scattering sample as it exposes it to greater radiation damage.

1.4 Presently used detectors

A variety of different detectors have been used in the field of time resolved non-crystalline diffraction including multiwire proportional chambers, image plates and CCD/TV devices. These all posses different strengths and weaknesses and the choice of a particular detector is often made on an experiment by experiment basis. A brief description of some of the devices used will now be given.

1.4.1 Image plates

The image plate can be thought of as an upgrade to the commonly used x-ray film. They have been described in detail elsewhere [4] and so only a brief description will be given. A typical image plate consists of a Europium doped BaFBr phosphor screen which is exposed to x-rays. The absorption of x-rays produces meta-stable states within the phosphor known as F centres. The readout of such a plate is achieved by scanning the phosphor with a red laser beam which causes the F centres to decay and emit blue light known as photo stimulated luminescence (PSL). The amount of PSL produced is proportional to the absorbed number of x-rays and is detected with a photo multiplier tube. Typical plate scanner systems can give image sizes of ~300 by 300 mm with a spatial resolution of ~200 microns FWHM and a dynamic range of $\sim 10^4$. Once readout the image plate is erased by exposure to optical light. All stages of the above mentioned process can induce noise into the final image. During the exposure, dark noise is introduced as the detector is completely passive. Noise can also be introduced from the significant variation in the number of F centres produced per x-ray and read noise is introduced due to the collection efficiency of the PSL.

The scanners available to readout image plates all have readtimes of roughly a minute or so, and erase times are generally of the same order. This obviously limits their use for time resolved studies but some systems have been produced [5,6] which enable a certain amount of time resolved studies to be undertaken. Such a system has been able to take 30ms muscle diffraction patterns at 200 ms intervals but only in 1 dimension. Despite these attempts image plates are not ideally suited for time resolved work due to their lack of real time readout and high noise levels.

1.4.2 CCD devices

Charge coupled devices (CCDs) are optical imaging devices which have revolutionised astronomy and various other fields. A CCD can be considered as an array of photosensitive capacitors coupled together where each capacitor represents a pixel. Photons incident on the array create charges which are stored on the capacitors. Once the exposure is completed the charges are transferred from each pixel to its neighbour and finally to an output amplifier. The rate at which this transfer occurs is determined by the capacitance of the electrodes which has the effect of rounding the high speed clock signals, necessary to readout the CCD. This causes the pixel to pixel charge transfer efficiency to be reduced with the loss of charge into adjacent channels. Although directly illuminated CCDs are sensitive to x-rays in the region used for diffraction, there exist several disadvantages of such a mode of operation. These include:

1. Their physical size; most are typically $1cm^2$. Large area CCDs exist $(6 \times 6cm)$ but they are difficult to manufacture and thus are expensive

2. To produce an electron-hole pair in silicon requires ~3.6eV of energy. So an 8keV x-ray will produce roughly 2000 electrons. The typical saturation level of a pixel is $\sim 2 \times 10^5$ electrons, so less than 100 photons can be accumulated before the device has to be readout.

3. The depth of the depletion region, which is effectively the absorption depth in CCDs, is very thin leading to very small detection efficiencies.

4. They are susceptible to radiation damage which causes an increase in the amount of dark noise and a reduction in the charge transfer efficiency.

These limitations have made them unacceptable as detectors for diffraction studies but by using some other method of converting the x-ray to optical photons, systems can be designed which are suitable for x-ray diffraction [7,8]. These include the coupling of phosphors to the CCD either directly or indirectly by using image intensifiers.

1.4.3 Multiwire proportional chambers

The multiwire proportional chamber (MWPC) was developed at CERN for particle detection and tracking in high energy physics experiments [9]. Since then many variants of the MWPC have been produced and used in a wide variety of fields including astronomy, nuclear physics and medicine.

In its basic form the MWPC consists of a set of electrodes capable of producing large electric fields enclosed within a gas volume. Incoming x-rays are absorbed within the gas causing photo or Auger electrons to be emitted, see section 2.2. A charge cloud is produced with a magnitude proportional to the energy of the incident x-ray. The number of electron ion pairs produced is governed by the gas, but for commonly used gases such as Ar and Xe about 30eV is required to produce each pair, yielding about 250 electrons for an 8keV photon. This is a factor of ten lower than the number produced in a silicon CCD, but the MWPC can amplify the number produced by factors of $10^5 - 10^6$ as a result of avalanches created from the high electric field, see section 2.3.3. As long as this gas gain is kept below the saturation level, the size of the signal produced remains proportional to the deposited energy. The avalanche is also localised about its initial position which allows positional information to be determined from the detected signal. Thus the signals from a MWPC are large enough to detect individual photons with high spatial resolution and with reasonable spectral resolution. A more in depth description of the MWPC is given in [10]. The noise level in a MWPC is determined by the number of spontaneous discharges induced by thermionic emission. This is typically [2] 10 counts a second for an entire detector which leads to a noise rate of $\sim 10^{-5}$ counts per pixel per second for a 1000×1000 pixel readout.

The major disadvantages of the use of MWPCs for x-ray diffraction experiments are their count rate performance and the fact that they suffer from the effects of parallax broadening. The first point is due to the low mobility of the ions created in the avalanche, as compared to electrons, which leads to the so called space charge effect. This limits their local rate performance to $\sim 10^4$counts $mm^{-2}s^{-1}$. This can be improved upon by decreasing the anode cathode separation. One such way is to use wire technology with a small ($300\mu m$) anode cathode gap. One such device is the wire microgap detector which has been developed at the Daresbury laboratory [11]. A further way is to use photolithography techniques to produce an electrode structure on an underlying substrate [12]. Using such techniques very small electrode spacings can be produced allowing high rate operation to be achieved. Such devices are called microstrip gas chambers (MSGC). Both of the above mentioned devices are capable of local count rates $\sim 10^6$counts $mm^{-2}s^{-1}$ and for time resolved diffraction the main limitation for these detectors is in the readout system. Because these detectors are operated in photon counting mode, their global count rate performance is set by the speed of the data acquisition system. There exist a variety of methods to readout the detectors, and perhaps the most commonly used for time resolved studies is the delay line method [13]. The major limitation of this method is set by a parameter known as the event confusion time. This time interval is set by the delay line length and is typically of the order of 100ns. If a second event is incident on the detector during the delay line propagation time, position encoding errors are introduced which leads to both events being rejected. A solution to this problem has been proposed [14] where the event confusion time has been reduced to ~6ns which is nearing the limit of modern digital systems.

The parallax effect, which is due to the low density and finite thickness of the absorbing region, is a problem when x-rays are incident on a detector at high angle. This will be discussed further in chapter 3.

A further problem of gas detectors is that of ageing. These effects are generally due to the formation of deposits on the electrodes leading to a drastic decline in the performance of the detector. Any prospective detector candidate for x-ray diffraction at a synchrotron source must be able to withstand the high radiation environment present.

1.5 Summary

Time resolved x-ray diffraction requires a detector system with a very low noise performance and rapid frame rate capability whilst being able to withstand very high flux levels. Although integrating devices exist which can handle the flux levels the noise levels for these systems is too high to observe many weakly scattering features. Also time resolutions below 10ms are unattainable with these systems.

With the advent of the new photon counting detectors such as the wire microgap and the MSGC and with the faster readout systems developed a complete detection system could be available within the near future for the demanding field of time resolved x-ray diffraction.

Bibliography

[1] R.Lewis, I.Sumner, A.Berry, J.Bordas, A.Gabriel, G.Mant, B.Parker. K.Roberts. J.Worgan. *Multiwire X-ray Detector Systems At The Daresbury SRS* Nucl. Instr. and Meth. A273 (1988) 773-777

[2] R.Lewis, Private Communication

[3] A.H.Walenta. *X-ray detectors for synchrotron radiation* Proceedings of the European Workshop on X-ray Detectors for Synchrotron Radiation Sources

[4] J.Miyahara, K.Takahashi, Y.Amemiya, N.Kamiya, Y.Satow. *A new type of x-ray area detector utilising laser stimulated luminescence* Nucl. Instr. and Meth A246 (1986) 572-578

[5] Y.Amemiya. *Imaging Plate- X-ray area detector based on photostimulable phosphor* Syn. Rad. News Vol 3 No. 2 (1990) 21-26

[6] N.Yagi, S.Takemori, M.Watanabe. *An x-ray diffraction study of frog skeletal muscle during shortening near the maximum velocity* J. Mol. Biol. 231 (1993) 668-677

[7] Y.Amemiya, K.Ito, N.Yagi, Y.Asano, K.Wakabayashi, T.Ueki, T.Endo. *Large aperture TV detector with a beryllium-windowed image intensifier for x-ray diffraction* Rev. Sci. Instr. 66 (2) (1995) 2290-2294

[8] N.Yagi, Y.Amemiya, K.Wakabayashi. *A real time observation of x-ray diffraction from frog skeletal muscle during and after slow length changes* Japanese Journal of Physiology 45 (1995) 583-606

[9] G.Charpak, R.Bouclier, T.Bressani, J.Favier, C.Zupancic. *The use of multiwire proportional chambers to select and localise charged particles* Nucl. Instr. and Meth. 62 (1968) 202-226

[10] F.Sauli. *Principles of Operation of Multiwire Proportional and Drift Chambers*, CERN 77-09 1977

[11] R.A.Lewis, N.S.Fore, W.Helsby, C.Hall, A.Jones, B.Parker, I.Sumner, J.S.Worgan, C.Budtz-Jorgensen. *High Counting Rate Gaseous X-ray Detectors for Synchrotron Radiation Applications,* Rev. Sci. Instr. 63(1) (1992) 642-647

[12] A.Oed. *Position-sensitive detector with microstrip anode for electron multiplication with gases,* Nucl. Instr. and Meth. A263 (1988) 351-359

[13] V.Perez-Mendez, M.Greenstein, D.Ortendahl. *Evaluation of factors contributing to position accuracy in delay line readout of MWPC* IEEE Trans. Nucl. Sci. 24 No.1 (1977) 209-212

[14] R.A.Lewis, C.J.Hall, W.Helsby, A.Jones, B.Parker, J.Sheldon. *A 10MHz photon counting detector system for time resolved x-ray diffraction* SPIE 2521 (1995) 290-300

Chapter 2

Principles of operation of Gas detectors

2.1 Introduction

The basic principles of the operation of gas detectors will be discussed in this chapter. Initially the various interactions of photons within matter will be considered followed by sections on gas ionisation, the various gas parameters and avalanche processes.

2.2 The interaction of photons with matter

Photons can interact with matter in many different ways depending on their energy, Eγ. The three main ways are: the photoelectric effect, which dominates to Eγ~200keV; Compton scattering, which dominates from ~200keV to ~10MeV; and pair production, which is present at energies above 1.022MeV. The result of such an interaction is not a degradation in the photon energy but a reduction in the beam intensity as the photon is entirely removed from the beam either by absorption or scattering. The intensity of a beam of photons as they traverse a medium of thickness X having N molecules per unit volume is:

$$I = I_0 e^{-\sigma NX} = I_0 e^{-\mu x} \tag{2.1}$$

where I_0 is the incident beam intensity, σ is the photon interaction cross section, μ is the mass attenuation coefficient and $x = \rho X$ is the reduced thickness of the medium where ρ is the density of the medium. For the photon energies used in dynamic muscle diffraction experiments, E γ~10keV, and also for the energies of x-rays used in the results of this thesis, the photoelectric effect is the dominant mechanism and this will looked at more closely in the next section.

2.2.1 The Photoelectric effect

The photoelectric effect is a quantum process involving the absorption of an incoming photon by an atom with the subsequent ejection of an atomic electron. If we denote E_k to be the energy of the k^{th} shell, photoelectric absorption can only occur for photon energies, $E\gamma$, greater than or equal to E_k and for a given photon energy the contributions of all levels with $E<E\gamma$ add up.

At energies above the highest electron binding energy of the atom (the K-shell), absorption is relatively small but increases as the K-shell energy is approached and is a maximum at the edge. After this point the absorption drops since K-shell electrons are no longer contributing to photoelectric absorption. This is known as the K absorption edge. At energies less than the K edge, absorption rises again until the L and M absorption edges are reached. At any given energy, lighter elements have the smallest absorption coefficients and, except for the heavier noble gases, at energies above a few keV, K edge absorption dominates [1].

Absorption of a photon of energy $E\gamma$ in a shell of energy E_k results in the emission of a photoelectron with energy $E_e=E\gamma-E_k$ and the excited atom can return to its ground state by one of two mechanisms:

1. Fluorescence, the transition of an electron from a shell with energy $E<E_k$ into the K shell with the subsequent emission of a photon of energy E_k-E or

2. Radiationless transition, or Auger effect, which is an internal rearrangement of electrons from lower energy shells with the emission of one or more electrons with total energy ~ E_k.

The fraction of de-excitations producing the emission of a photon is called the fluorescence yield, and for the K shell this increases with atomic number. If we consider argon, which is commonly used in gas detectors, 15% of the photoelectric absorption's in the K shell are followed by fluorescence while for the remaining 85%, two or more electrons, one with energy $E\gamma-E_k$ and others with energy smaller than E_k are produced [1]. The secondary photon resulting from the transition to the K shell is emitted at an energy just below the K edge and since it has a very long mean free path for absorption, ~36mm in argon at STP [1], it can escape from the volume of detection. This produces the so called argon escape peak at an energy $E\gamma-E_k$. In argon the shell energies are (in keV): $E_k=3.20$, $E_l=0.29$, $E_m=0.04$. If an Fe^{55} source is used to illuminate the detector, the main peak occurs at $E_{main}=5.966$ keV with the escape peak at 2.766 keV (see for example figure 2.1).

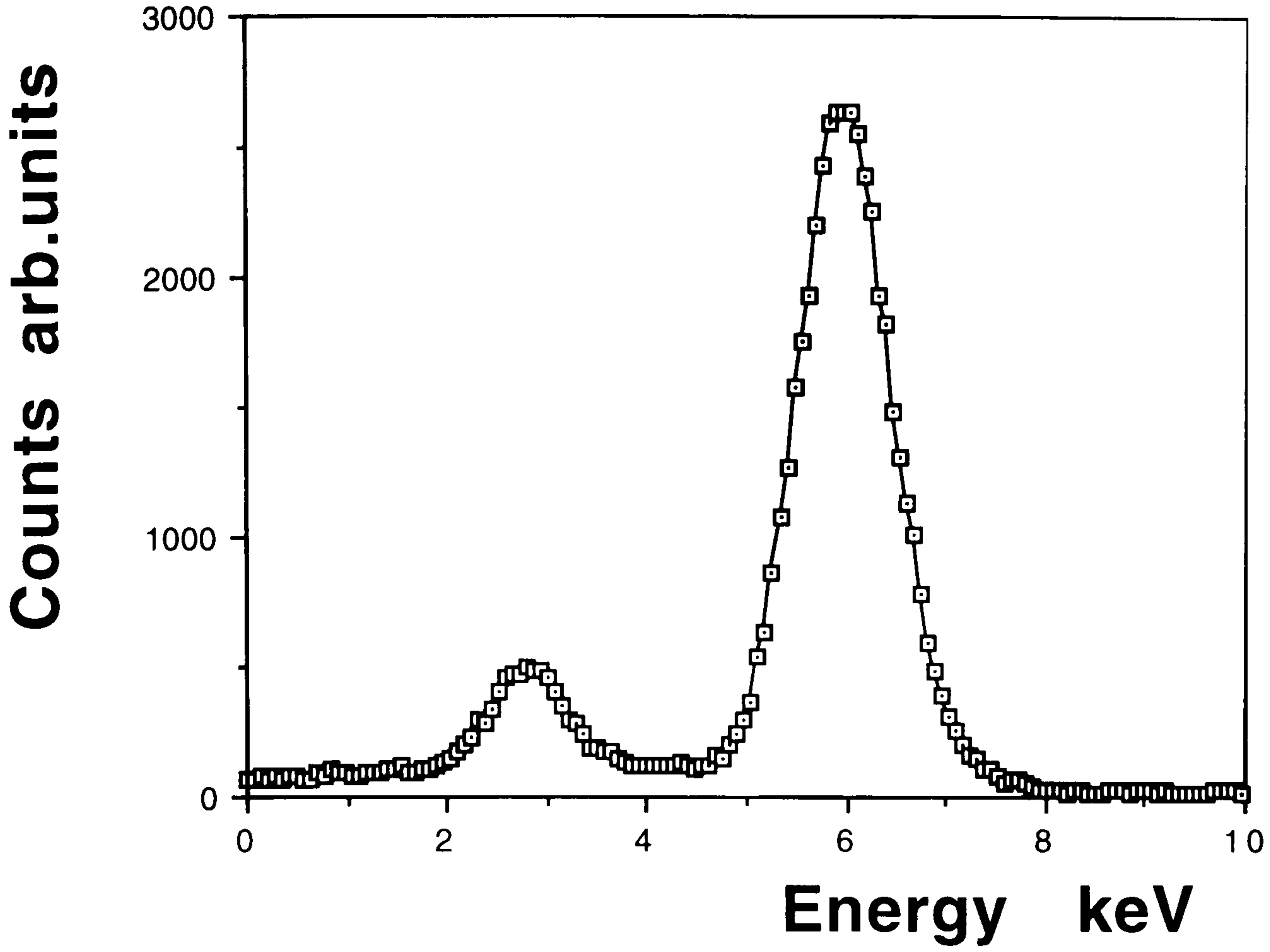

Figure 2.1: Schematic of and Fe^{55} spectrum with main peak occurring at ~6keV and escape peak at ~3keV. The ratio of counts in each peak is ~5:1.

2.3 Ionisation mechanisms and avalanche multiplication

A brief discussion concerning ionisation and recombination processes in gases will first be given before turning to the avalanche multiplication process

2.3.1 Primary and total ionisation

When ionisation occurs in a gas through the interaction with a photon, unlike excitation, no exact energy requirement has to be satisfied. In the ionisation of an atom or molecule X a free electron and ion are created by the process:

$$X + \gamma \rightarrow X^{+} + \gamma + e^{-}$$

with a cross section typically of the order of $\sigma \approx 10^{-16} cm^{-2}$ [2]. The electron and ions created by the incident radiation itself are called primary ionisation. If a large enough energy is transferred to the ejected electron, this can also create further ionisation, provided its energy is greater than the ionisation potential of the medium. This is known as secondary ionisation, and the process can continue if the secondary electrons have sufficient energy to further ionise the medium, until the threshold for ionisation is reached.

A second mechanism for ionisation in gases is the so called Penning effect. In the gas metastable states may be created which, because of a large spin-parity difference or quantum forbidden states, are unable to de-excite immediately to their ground state but may do so after a collision with a second atom. This results in the ionisation of this atom and the effect is common to molecular gases on noble gases and noble gases on noble gases, e.g.:

$$Ar + Ne^{*} \rightarrow Ar^{+} + Ne + e^{-}$$

A third mechanism which occurs in noble gases is the formation of molecular ions. In this, a positive ion interacts with a neutral atom of the same species to form a molecular ion, i.e.:

$$Ar^{*} + Ar \rightarrow Ar_2^{+} + e^{-}$$

The sum of all the different processes for ionisation is called total ionisation, and the average total number of ion pairs produced, n_t, is then:

$$n_t = \frac{\Delta E}{w_i} \qquad (2.2)$$

where ΔE is the total energy lost in the gas volume and w_i is the effective average energy to produce one electron ion pair. In most gases the average energy to produce an electron ion pair is between 22 and 35eV and as a photon deposits all its energy during an interaction ΔE is simply the photon energy. In fact for a 5.966keV x-ray interacting in an argon-hydrocarbon gas mixture roughly 235 electron ion pairs are created.

2.3.2. Recombination and electron attachment

Once electron ion pairs are created, it is important that they remain in a free state long enough to be collected at the electrodes of a detector. Two mechanisms exist which hinder this: recombination and electron attachment. Recombination occurs between ions and electrons because of their mutual coulomb attraction but generally only occurs when there is no electric field present. The rate of recombination depends on the concentration of the electrons and ions and when it takes place a photon is emitted in the process, e.g.

$$X^+ + e^- \rightarrow X + h\nu$$

Electron attachment on the other hand, is a process involving the capture of a free electron by an electronegative atom resulting in the formation of a negative ion, and is described by:

$$X + e^- \rightarrow X^- + h\nu$$

Hence the presence of any electronegative gas in the detection volume will severely degrade the resulting pulses on the electrodes and are therefore generally considered as pollutants. Common examples of electronegative gases are O_2, N_2O and CF_4. As an example of the seriousness of this problem if we consider a 1% level of air pollution in argon it will remove about 33% of the migrating electrons per cm of drift due to electron attachment [1].

2.3.3 The avalanche process

Avalanche multiplication occurs in a gas detector when the primary ionisation electrons gain sufficient energy from the accelerating field to cause further ionisation. The resulting secondary electrons then produce tertiary ionisation and so on giving rise to the formation of an avalanche. As will be covered in the next section, the mobility of the electrons formed is much greater than that of the ions and the developing avalanche assumes the form of a liquid drop with the electrons at the head and the slower ions at the rear.

If λ is defined as the mean free path of the electron for a secondary ionising collision, then $\alpha = 1/\lambda$ is the probability of an ionisation per unit length and is known as the first Townsend coefficient. If there are n electrons, then in a path dx there will be

$$dn = n\alpha dx \qquad (2.3)$$

new electrons created . Integrating 2.3 yields the total number of electrons created in a path x

$$n = n_0 \exp(\alpha x) \text{ and } \overline{M} = \frac{n}{n_0} = \exp(\alpha x) \qquad (2.4)$$

where n_0 is the original number of electrons, n the total number of electrons in the path x and $\overline{M}$ is the multiplication factor or gas gain. For non-uniform fields α is a function of x and 2.4 becomes:

$$\overline{M} = \exp\left[\int_{x_1}^{x_2} \alpha(x)dx\right] \tag{2.5}$$

While $\overline{M}$ can increase without limit, practically it is limited to about $\overline{M}<10^8$ or $\alpha x<20$ before breakdown occurs. This is known as the Raether limit [3].

2.4 Transport of charges in gases

An understanding of the motion of electrons and ions is important for ionisation detectors as these can influence many operational characteristics of the detector. In the first instance this motion will briefly be discussed for the case of zero electric field and then the effect of an applied field will be considered.

2.4.1 Diffusion of electrons and ions

If no electric field is present, electrons and ions produced by an ionising collision will diffuse uniformly about their point of creation. After suffering multiple collisions with the gas molecules they loose their energy and quickly reach thermal equilibrium where they will eventually recombine. The average energy assumed is ~0.04eV from simple kinetic theory, at normal conditions, and the energy of the charges is described by the Maxwell distribution function [1] which gives a mean speed of:

$$v = \sqrt{\frac{8kT}{\pi m}} \tag{2.6}$$

where k is Boltzmans constant, T the temperature and m the mass of the particle. It is obvious from 2.6 that the average speed of the electrons produced will be of the order of a 1000 times greater than that of ions due to their smaller mass. The distribution of charges after diffusing a time t can be shown [1] to be Guassian:

$$\frac{dN}{dx} = \frac{N_0}{\sqrt{4\pi Dt}}\exp\left(-\frac{x^2}{4Dt}\right) \tag{2.7}$$

where N_0 is the total number of charges, x the distance from the point of creation and D the diffusion coefficient. The rms spread in x is thus:

$$\sigma(x) = \sqrt{2Dt} \text{ for linear diffusion or } \sigma(r) = \sqrt{6Dt} \text{ for spherical diffusion} \qquad (2.8)$$

The diffusion coefficient for an atom can be calculated using Kinetic theory and is given by:

$$D = \frac{1}{3} v\lambda \qquad (2.9)$$

where λ is the mean free path of the charge in the gas. Again because of their smaller size than ions, electrons have a larger mean free path than ions in the same gas and for a classical gas :

$$\lambda = \frac{1}{\sqrt{2}} \frac{kT}{\sigma_0 P} \qquad (2.10)$$

with σ_0 the total cross section for a collision in the gas and P the gas pressure. Substituting 2.6 and 2.10 into 2.9 gives:

$$D = \frac{2}{3\sigma_0 P} \sqrt{\frac{(kT)^3}{\pi m}} \qquad (2.11)$$

The dependence of the diffusion coefficient on the various gas parameters can now be seen.

2.4.2 Drift velocity and mobility of electrons and ions

In the presence of an electric field, W, the electrons and ions produced by ionisation will be accelerated towards the anodes and cathodes. This acceleration is impaired by collisions with the gas molecules which limits the average velocity attainable by the electrons and ions. This average velocity is known as the drift velocity, u, of the charge and is superimposed on its normal random movement. One can also define the mobility μ of a charge such that:

$$\mu = \frac{u}{W} \text{ or } \mu = u\left(\frac{W}{P}\right)^{-1} \qquad (2.12)$$

where P is the gas pressure and W/P is known as the reduced electric field. For positive ions up to relatively high fields, the drift velocity is linearly dependent on the reduced electric field and therefore under constant pressure, the mobility is constant. In thermal equilibrium the mobility and the diffusion coefficient D are related by the Einstein expression [2]:

$$\frac{D}{\mu} = \frac{kT}{e} \approx 0.026eV \tag{2.13}$$

In section 2.4.1 the rms spread of ions diffusing over a length x for a time t was given by equation 2.8 and substituting 2.13 and 2.12 in 2.8 gives:

$$\sigma = \sqrt{\frac{2kTuPt}{eW}} = \sqrt{\frac{2kTPx}{eW}} \tag{2.14}$$

and as can be seen the rms linear diffusion is independent of the species of ions in the gas.

Electrons, however, have been found to have a mobility which is much greater than that of the ions and which is dependent upon the applied electric field. This being due to their smaller mass which allows them to increase their energy between collisions [4]. The drift velocity for electrons can be expressed as:

$$u = \frac{e}{2m} W\tau \tag{2.15}$$

where τ is the mean time between collisions and is in general a function of the electric field. It has been found that the collision cross section, and therefore τ, varies greatly with electric field, going through maxima and minima (Ramsauer effect). This is due to the fact that the electron wavelength approaches those of the shell electrons of the gas molecule and complex quantum mechanical processes occur. Cross sections for dimethyl-ether (DME) are shown in figure 2.2 [5]. In the figure; I represents ionisation cross section; V vibration cross section; El elastic cross section and Ex excitation cross section. The energy distribution will therefore change from the original Maxwellian distribution and the average energy can exceed the thermal value by several orders of magnitude at high fields. The energy distribution is described by [1]:

$$F(E) = C\sqrt{E}\exp\left[-\int \frac{3\Lambda(E)EdE}{\left[eW\lambda(E)\right]^2 + 3EkT\Lambda(E)}\right] \tag{2.16}$$

where $\Lambda(E)$ is the fraction of energy lost on each impact, in other words the amount of

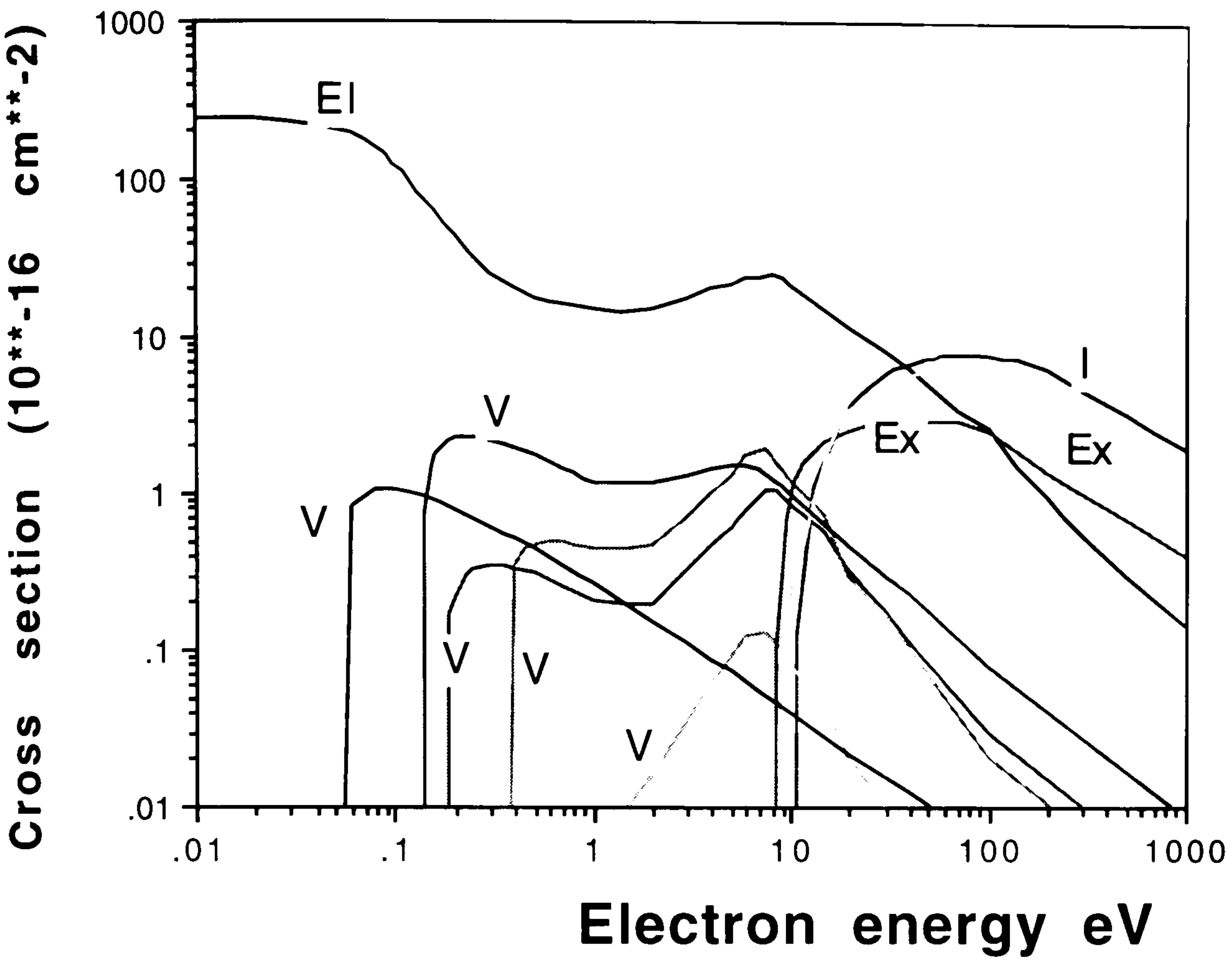

Figure 2.2: Electron scattering cross sections for DME from [5]. I represents ionisation cross section; V vibration cross section; El elastic cross section and Ex excitation cross section.

energy spent in processes like vibrational and rotational excitations and $\lambda(E)$ is the mean free path between collisions which is given by:

$$\lambda(E) = \frac{1}{N\sigma(E)} \tag{2.17}$$

where N is the number of molecules per unit volume and $\sigma(E)$ is the electron scattering cross section which is determined from curves like the one given in figure 2.2.

This electron gain in velocity also effects the diffusion rate. The factor kT in equation 2.10 is replaced by this mean energy and the diffusion coefficient D also increases accordingly causing a greater spread of the electron cloud than that given by 2.9 and can be expressed as:

$$D(W) = \int \frac{1}{3} u\lambda(E)F(E)dE \tag{2.18}$$

where $u = \sqrt{2E/m}$ is the instant velocity of electrons of energy E.

2.5 The choice of gas filling

Since avalanche multiplication occurs in practically all gases or gas mixtures in a proportional chamber, the choice of gas used is generally determined by the particular application in which the detector will be used. In noble gases this multiplication occurs at a much reduced field than in complex molecules due to the many non-ionising energy dissipation modes available in polyatomic molecules. This therefore suggests the use of one of the noble gases. In synchrotron radiation work, or in any field where the photon needs to be absorbed in a relatively small drift gap, this dictates the use of one of the heavier noble gases so as to be able to efficiently absorb the incoming photon. Due to the high costs of xenon and krypton the choice naturally falls on argon. However, if argon alone is used gains in excess of ~100 cannot generally be exceeded without the occurrence of continuous discharges. This is due to the following reasons. During avalanche multiplication excited and ionised atoms are formed. The excited noble gases can only return to their ground state through a radiative transition and the minimum energy of the emitted photon, the excitation potential of argon which is 11.6eV, is well above the ionisation potential of any metal constituting the electrodes (7.7eV for Cu, 6.0eV for Al, 9.2eV for Au). Hence photoelectrons can be extracted from the electrodes which will initiate further avalanches. On the other hand argon ions can migrate to the cathodes where they are neutralised resulting in the extraction of an electron. The balance of energy is then either radiated as a photon or by secondary emission, i.e. the extraction of another electron from the cathode surface. Both of these processes can result in the formation of avalanches, and since they occur after the initial avalanche the counter will enter a permanent discharge mode.

The addition of a polyatomic gas molecule to the noble gas can counteract this problem because polyatomic gases posses non-radiative excited states (rotational and vibrational). These states absorb the emitted photons over a large energy range thus preventing spurious avalanches. The molecule then dissipates the excess energy either through elastic collisions or by dissociation into simpler species. Similarly when these ions are neutralised at the cathode they either dissociate or polymerise. Gases possessing such characteristics are known as quenchers and most examples are organic compounds like alcohol's and hydrocarbons. There are also a few inorganic compounds like CO_2, BF_3, CF_4 and some freons. The addition of a quencher to a noble gas thus allows much higher gains to be achieved without the onset of breakdown.

The use of organic quenchers can, however, seriously affect the detector's lifetime characteristics, especially under intense particle fluxes. The polymers and dissociation products formed in the avalanche can cause the detector to "age". See chapter 5.

2.5.1 Experimental operation requirements

The gases considered for use in MSGCs are similar to the ones which have given the best results for MWPCs. They are mostly mixtures of noble gas-hydrocarbon where the noble gas tends to be argon or xenon and the hydrocarbon is isobutane, DME and in some cases CO_2. Table 2.1 lists some of the commonly used gases along with their most important characteristics such as atomic and mass numbers, ionisation potential and the effective energy required to produce an ion pair in the gas. The gas mixtures used for much of the work reported in this thesis are mostly mixtures of argon and DME. They have been specifically chosen for use at future high energy physics colliders and have therefore been optimised in terms of drift velocity, high primary ionisation density, high total ionisation density, small gas gaps, high gain etc. For synchrotron work these requirements are slightly different such as the need for a thick enough gas volume to efficiently absorb the photons, a gain high enough to allow unambiguous x-ray detection which is dependent on the electronics used to readout the detector and a rate capability which far exceeds that needed in high energy physics. But valuable information can be obtained from these gas mixtures.

Gas	Atomic No.	Mass No.	Ionisation potential (eV)	Average energy to produce an ei pair, w_i
H_2	2	2	15.4	36.3
Ar	18	39.9	15.8	26.3
Xe	54	131.3	12.1	21.9
CO_2	22	44	13.8	32.8
CH_4	10	16	13.1	27.1
iso-C_4H_{10}	34	58	10.8	23.2
DME	26	46	10.0	-

Table 2.1: Some of the properties of gases used in gas detectors. A w_i for DME has not been published. Dimethly-ether has the chemical formula $(CH_3)_2O$. The values of w_i have been obtained from [6].

Bibliography

[1] F.Sauli, *Principles of Operation of Multiwire Proportional and Drift Chambers,* CERN 77-09 1977

[2] W.R.Leo, *Techniques for Nuclear and Particle Physics Experiments,* Springer-Verlag, Berlin 1987

[3] H.Raether, *Electron Avalanches and Breakdown in Gases,* Butterworths Scientific Publications, London 1964

[4] J.Townsend, *Electrons in gases,* Hutchinson, London 1947

[5] S.F.Biagi, private communication.

[6] S. Kiourkos. *Development of Microstrip Gas Chambers for High Energy Physics Experiments* University of Liverpool, PhD thesis, 1995

Chapter 3

The Parallax Free Detector

3.1 Introduction

An undesirable feature of x-ray imaging gas chambers is the parallax effect. For non-normal x-ray incidence to the plane of the detector, the variation in the photon path as it interacts in the detection volume causes a broadening of the point spread function (PSF) of the detector. There is a resultant uncertainty in the detected position of interaction. (A detectors' response to illumination from an infinitely narrow beam is called its point spread function) See figure 3.1. The extent of this effect will depend on the interaction path length distribution behind the detector entrance window up to the

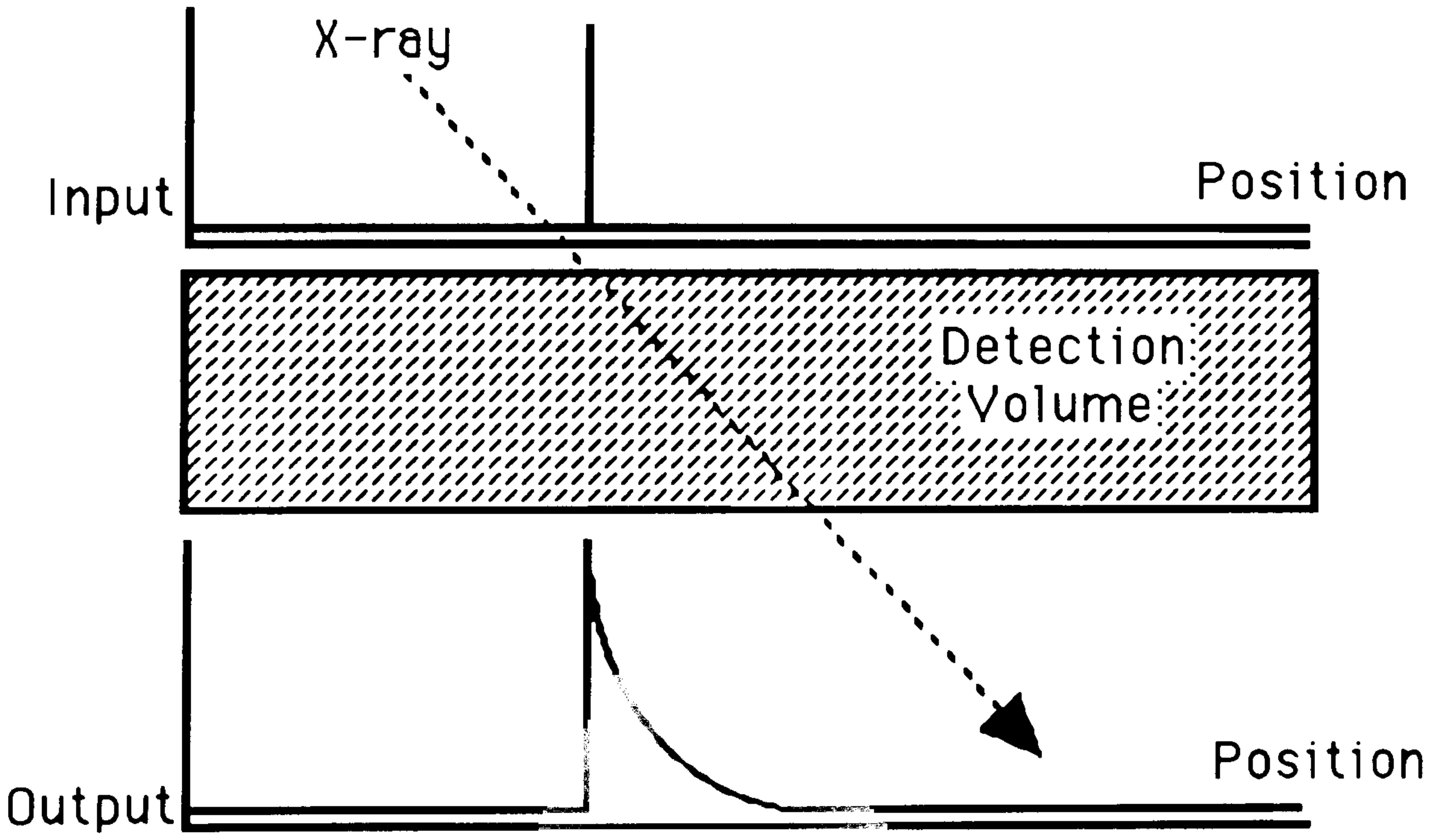

Figure 3.1: The parallax error in recording the position of interaction of non-normal x-ray

detection plane. There are several methods currently being pursued, utilising a gas detection region, in which the effects of parallax may be reduced. These are:

1. The creation of a spherical drift field in the detection volume
2. Increasing the gas pressure
3. The use of a high density photoconverter coupled to a gas detector

All three proposals have been or are being presently investigated [1,2,3]. Both creating a spherical drift field and increasing the gas pressure work well, but the detectors are still limited by the count rate capability of the MWPC part of the detector. The use of a photoconverter has also successfully been used but such detectors are limited by the relatively low detection efficiency. Detectors exist which do not suffer from the effects of parallax i.e. image plates, but these devices are not suitable for every application, see section 1.4.

In reference 3, a detector is described which utilises a photon converter coupled to a MWPC. The converter in this case being evaporated onto the entrance window of the gas enclosure. The detector described in section 3.3 is very similar to this but instead of the photoconverter coating being on the entrance window, a coated microchannel plate (MCP) is used. Theoretically the coated MCP should be more efficient at converting photons than a solid sheet of photoconverter, see next section, and this is the driving force behind this investigation. One could then foresee coupling a coated MCP to an MSGC so that the benefits of the photoconverter and MSGC could be utilised.

3.2 Description of the Microchannel Plate

Microchannel plate detectors have been extensively used in astronomical applications and as image intensifiers over the last 20 years or so. They are effectively miniaturised photomultipliers. Research into CsI coated MCPs has been carried out by the X-ray Astronomy group at Leicester University by G.W. Fraser et al [4,5] and this group have kindly supplied the coated MCP for the purpose of this test. A detailed description of how a microchannel plate works is beyond the scope of this thesis so only a brief description will be given before going on to describe the coupled detector. Excellent descriptions of how MCPs work can be found in the literature [6,7].

In essence, the MCP is an array of channel electron multipliers (CEM)[6] and it works in the same way i.e. it consists of a length of resistive tubing, which is long compared to its diameter. A potential difference is applied across the ends of the tube, in vacuum, thereby producing a positive and negative terminal at the ends. Electrons or other energetic particles which strike the wall of the tube at the negative potential end will produce secondary electrons with some initial energy which carries them across the channel. The applied electric field accelerates the electrons axially while the electrons traverse the tube, until they strike the wall where the electrons will have sufficient energy to create further secondaries. This process is repeated several times so that a large number of electrons emerge from the positive terminal of the tube. This is shown schematically in figure 3.2. The gain obtainable from such a system is governed by a number of parameters: applied voltage, residual gas pressure, resistance

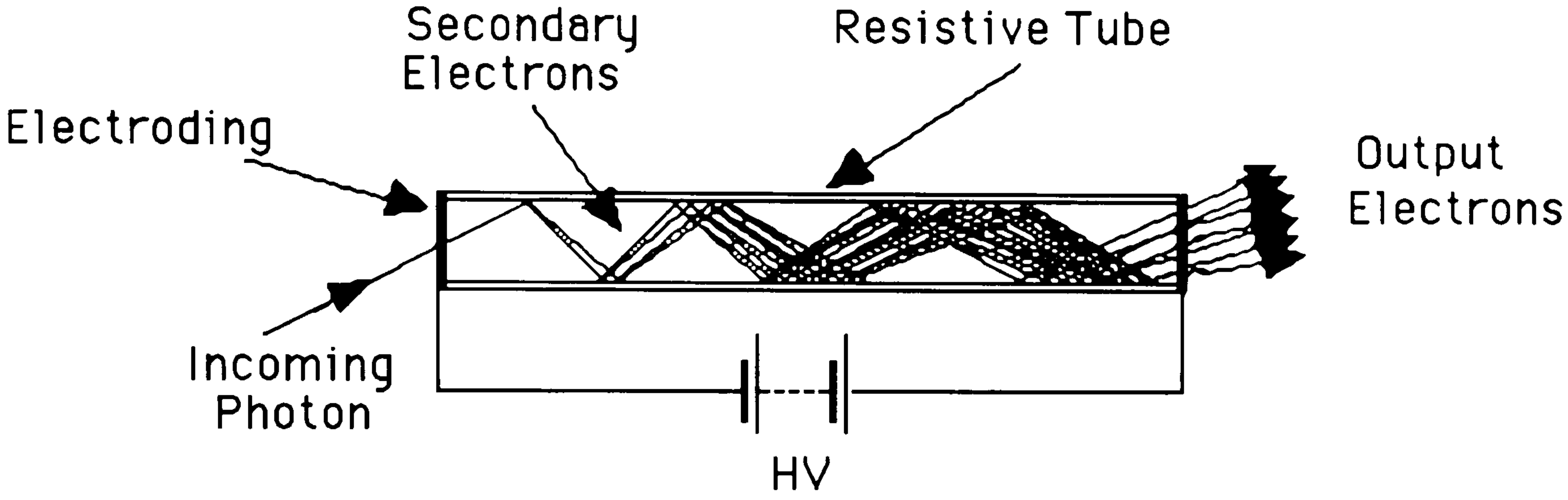

Figure 3.2: Schematic of a Channel Electron Multiplier

and length to diameter ratio of tube and the incident flux rate. A microchannel plate is a collection of a large number of such tubes which are manufactured by glass fibre drawing techniques. Each tube in the MCP array can be considered to be a continuous dynode structure which acts as its own dynode resistor chain. (Analogous to a photomultiplier) A schematic diagram of a MCP is shown in figure 3.3. The MCP is usually manufactured with the pores at some angle to the normal. This is known as the bias angle and is typically 6^0. Thus incoming photons will strike the inside of the pores at near grazing incidence. If the pores are coated with a photocathode material, such as CsI, there will consequently be an increase in the number of photoelectrons produced over a solid sheet of photocathode due to the cosec(θ) photoyield dependence [8]. If the primary photoelectrons deposit their energy close enough to the surface of the pore, the resulting secondaries will escape into the pore and be accelerated down the pore by the applied electric field.

3.3 Description and assembly of chamber

The dimensions of the pores of the MCP supplied for this investigation are diameter 12.5 microns, length of pore 0.5mm giving a length to diameter ratio of 40. The MCP was CsI coated by Leicester University by vacuum evaporation to a thickness of 14000Å. As given in reference 5 this corresponds to a thickness of CsI on the channel

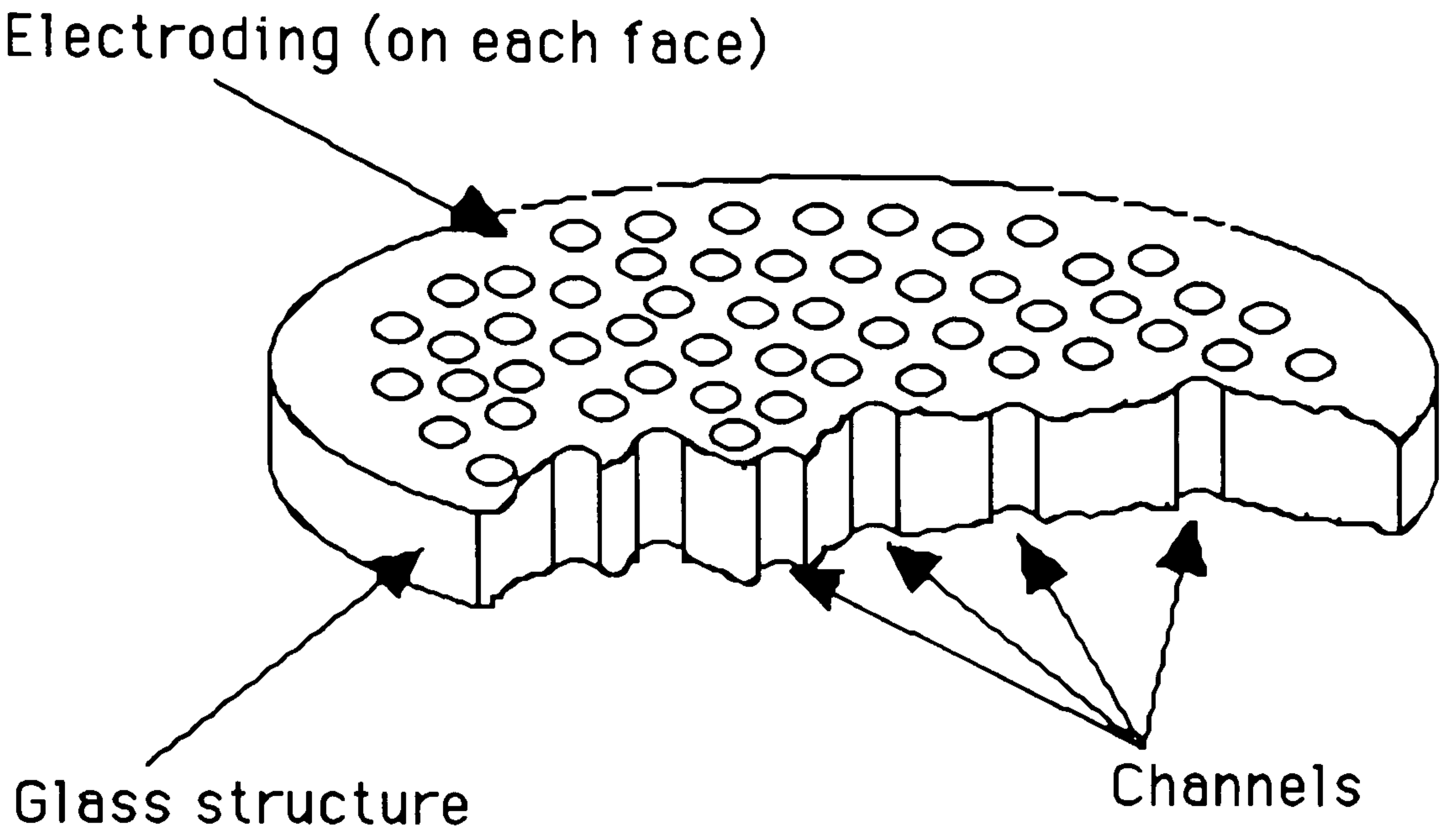

Figure 3.3: Schematic cutaway of Microchannel Plate

walls of between 310Å and 550Å. The active photocathode area had a diameter of 25mm. The bias angle of the plate was 13°. As CsI is hygroscopic, care was taken so that the coated MCP did not come into contact with any moisture, and all handling of the MCP was undertaken in a dry nitrogen atmosphere. A special holder for the MCP was made at Daresbury and a schematic diagram of this is shown in figure 3.4. As well as supporting the MCP, it also had to make electrical contact with the two surfaces of the

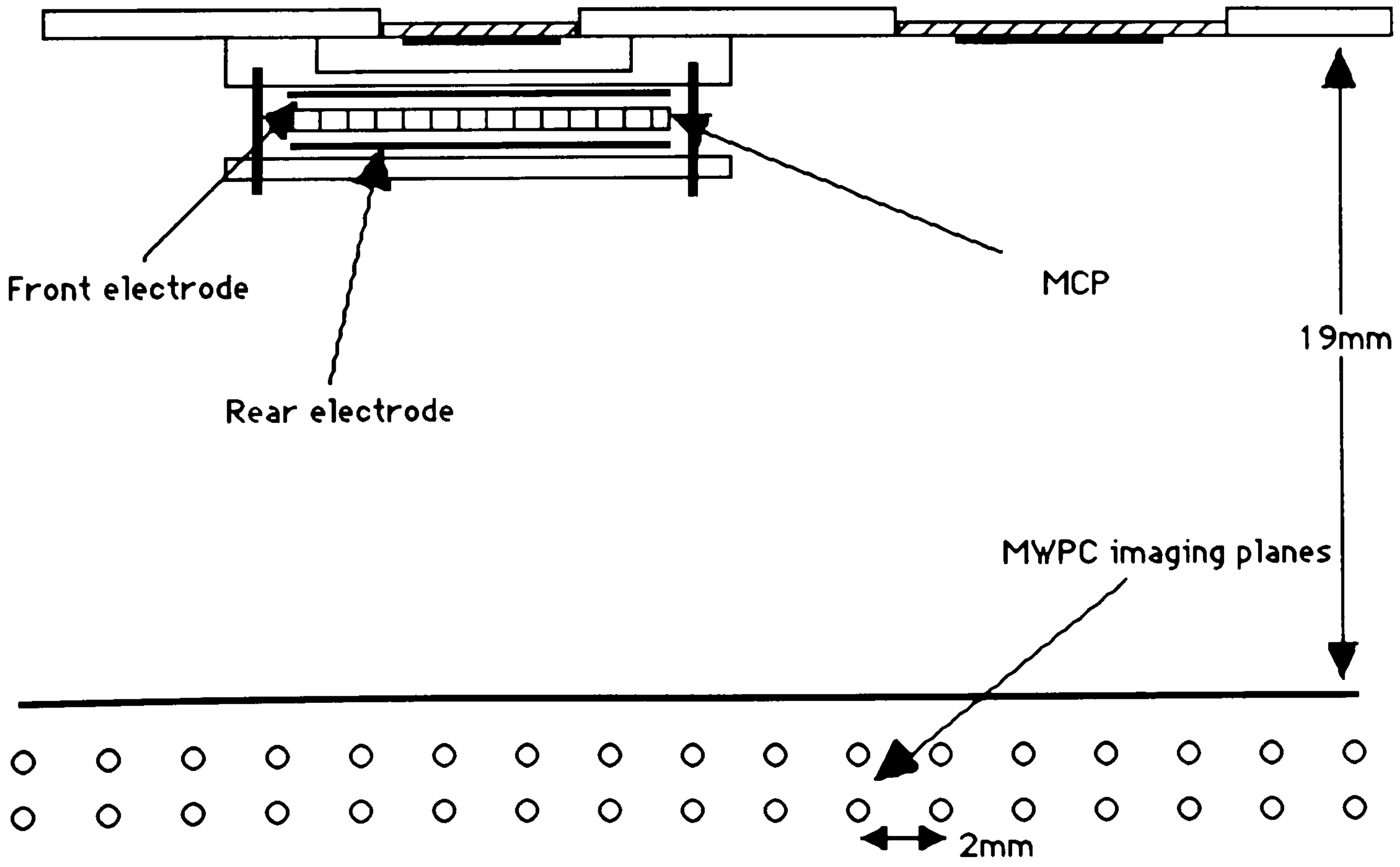

Figure 3.4: Schematic cross section through the chamber

MCP, and the electrodes were incorporated into the holder. The MCP holder was then fixed to the window of a modified Daresbury area detector, again in a dry nitrogen atmosphere. Once inside, the housing was sealed via a pneumatic valve. The dimensions and specifications for the area detectors have been adequately described elsewhere [9]. In addition to the MCP, a region of the window plate was formed into a drift cathode to allow a comparison to be made between the MCP coupled to the MWPC and just the MWPC. The signals from the cathodes were readout using delay line techniques and the system and preamplifiers are described in [9].

3.3.1 Principles of Operation of coated MCP coupled to MWPC

The basic operating principles behind the chamber are as follows. The incoming x-ray photon interacts with the CsI coating of the microchannel plate inducing secondary electron emission from the layer. With a suitable electric field applied across the two faces of the MCP, the secondary electrons created will be accelerated down the channel. Once the electrons reach the rear face of the MCP they then drift towards the wire frames under the action of the drift field set up by the rear face voltage and the ground plane of wires. Then as they drift closer to the wires, avalanche multiplication dominates, due to the applied potential on the anode wires. Thus the incoming photon is localised once it strikes the coated MCP. MCPs are normally operated at pressures of approximately 10^{-6} torr with a potential difference across the plate of the order of 1 to 2kV. The reason for working at low pressures are the problems associated with ion feedback. This occurs when working at high gains where the high charge density region at the output of a channel produces positive ions which can drift back up the channel and induce after-pulses. However, in this case where the role of the MCP is just to localise the photon, the intention is to operate the MCP at unity gain thereby avoiding the high ion currents that a large electron gain would induce. A further problem that should be alleviated by running the MCP at unity gain is the very poor rate performance. Again this is attributed to working at large gains where a substantial current is drawn and the channels take a long time to recharge. Thus by working at unity gain these large currents are avoided. So the hypothesis to be tested was that provided the MCP could be made to operate, the gas needed for the operation of the MWPC should not influence the MCPs behaviour.

3.4 Experimental Technique

A schematic of the apparatus used is shown in figure 3.5. The chamber was first evacuated to a pressure of 1 $\times 10^{-4}$ mbar to remove the majority of gas present. Once the desired pressure was reached the chamber was back filled with gas, for the majority of this work pure DME, to the required working pressure. This was between 1 and 30 mbar following the work of [3]. In the first instance the MWPC section of the chamber was characterised, and the count rate as a function of the anode and drift plane voltages was measured. Figure 3.6 shows the count rate versus the drift voltage for this section of the chamber at an anode voltage of 450 volts and at a pressure of 1 mbar. From this it was determined that a sufficient gain could be obtained to provide large enough signals for imaging purposes. A very intense source of 8 keV Cu x-rays was used as the probability of an x-ray interacting in such a low pressure gas is very low. Following this the MCP/MWPC part of the chamber was also illuminated. It was found that at the higher pressure of 30 mbar that the dark noise was considerably greater than at the lower pressure of 1 mbar and for all subsequent tests the chamber was operated at this lower pressure. This was assumed to be due to back flow of gas ions in the pores of the MCP. Figure 3.7 shows the anode count rate obtained with the MCP/MWPC section of

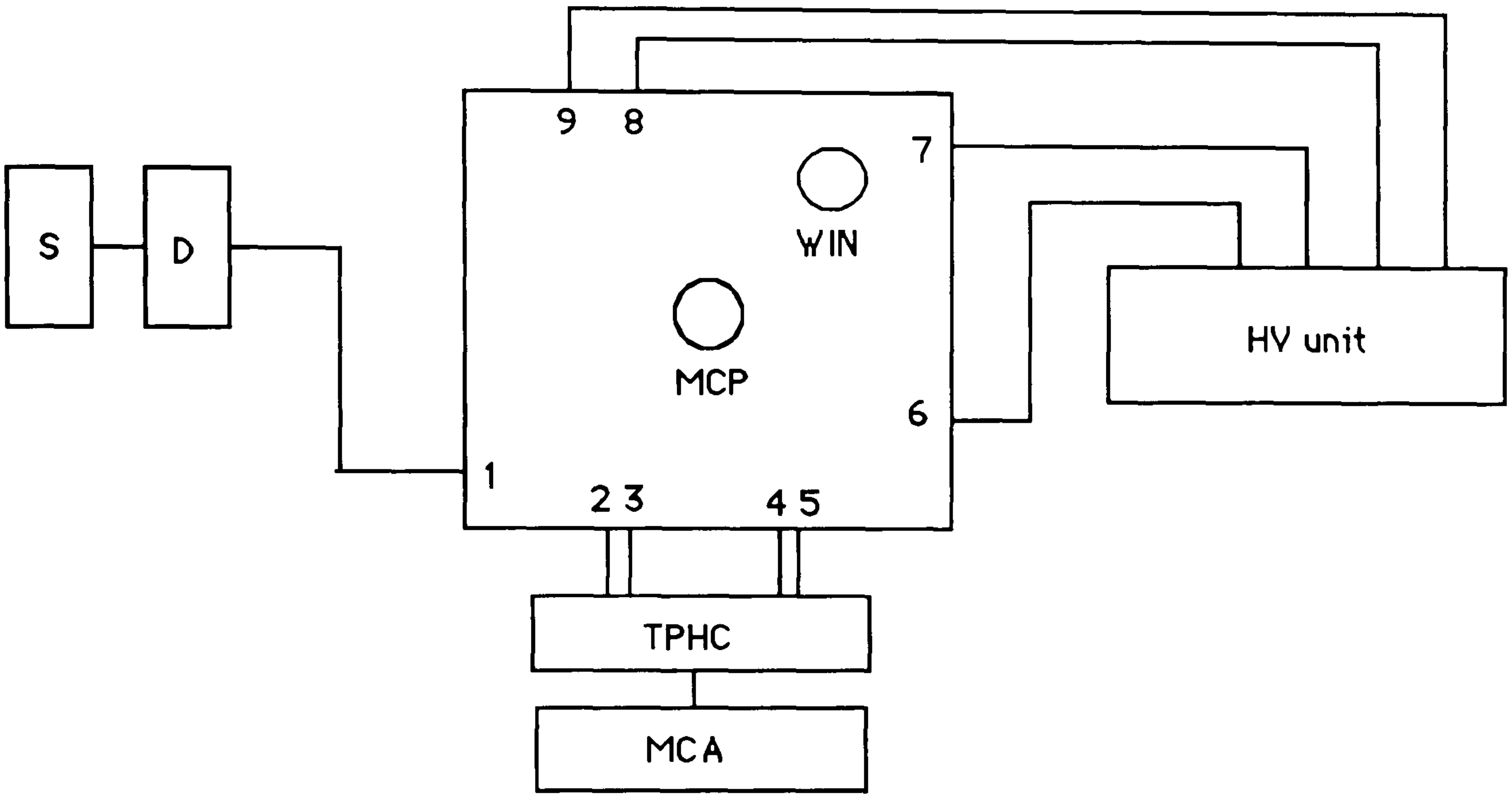

Figure 3.5: Schematic of apparatus used. The following abbreviations have been used: S scaler; D discriminator; TPHC time to pulse height converter; MCA multi channel analyser; HV high voltage supply. The numbers 1 to 9 signify: anode signal, x1,y1,x2,y2 cathode signals, anode terminal, window terminal, rear MCP terminal and front MCP terminal respectively.

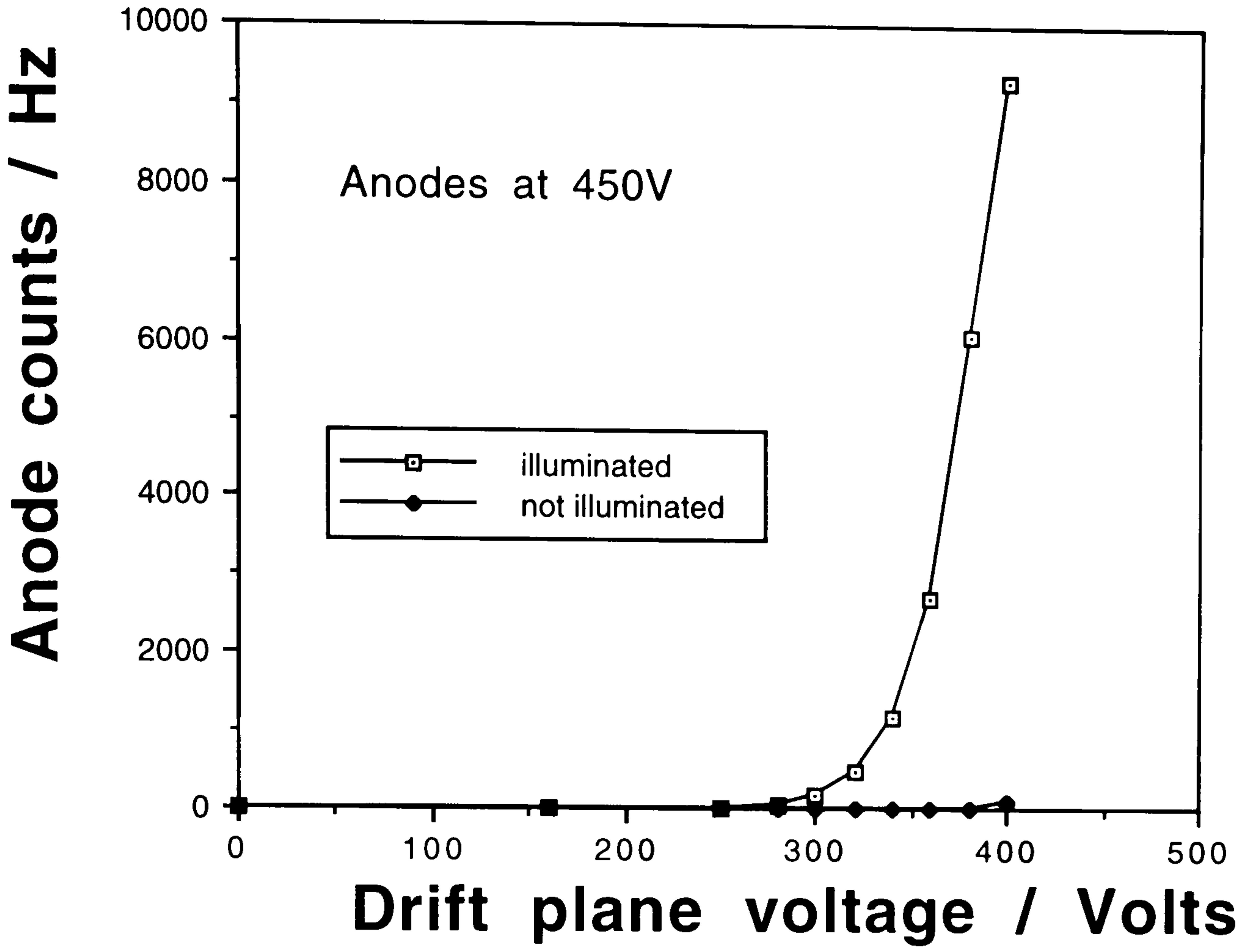

Figure 3.6: Count rate as a function of drift voltage for the MWPC section of the chamber at a fixed anode voltage

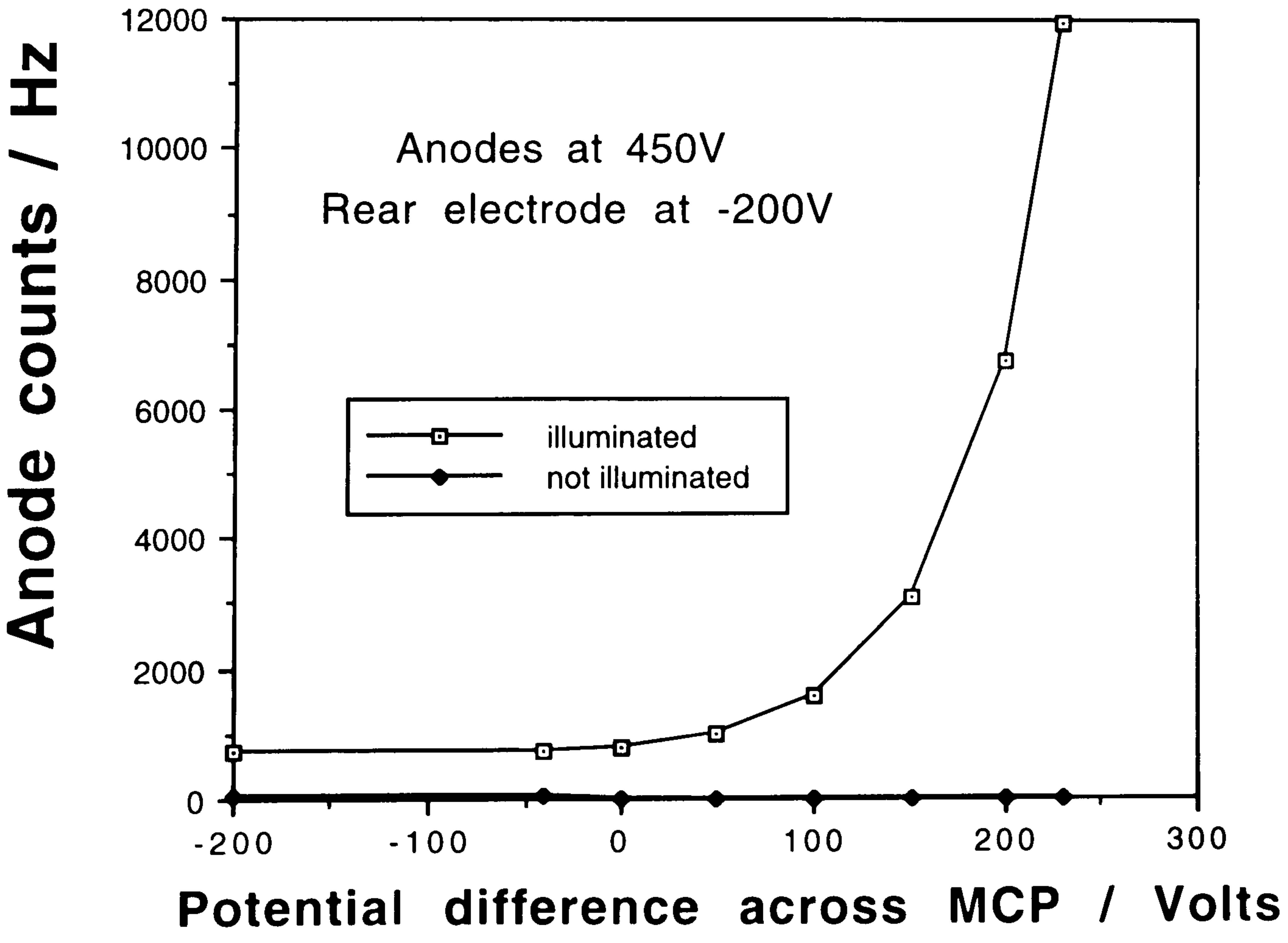

Figure 3.7: Anode count rate versus the potential difference across the MCP

the chamber versus the difference in potential across the MCP. The anodes were at 450 volts and the rear electrode of the MCP was kept constant at -200 volts. The figure shows the effect of varying the front electrode potential and clearly shows the effect of x-ray interactions within the MCP. The upper limits of the curves are determined by a current trip of greater than 5 μA on any of the three electrodes.

3.4.1 Imaging tests

Once it was determined that the chamber was operating at a sufficient level, imaging tests were performed. The system was first calibrated in the following way. The start and stop signals from one dimension of the cathode plane, either 'x' or 'y', were fed into a time to pulse height converter (TPHC) which was then used as the input to a multichannel analyser (MCA). The time difference between the start and stop signal then gives the positional information required to determine where in the detector an event has occurred. A 100 μm collimated beam of x-rays was then used to illuminate the chamber at 1mm intervals across the detector area. From this one can calculate the number of MCA channels equivalent to 1mm. This also enables one to determine the full width at half maximum (FWHM) of the point spread function (PSF) of the chamber for normal incidence. This was found to be 2.1 ±0.3mm which is quite poor for an imaging device. This was due to the poor signal to noise ratio obtained with this chamber. If one now illuminates the chamber at some angle relative to the normal one can determine whether there is any error due to parallax. Figure 3.8 shows the PSF of the chamber both normally and at 18° to the normal, and from this graph one can determine that the FWHM of the PSF for non-normal incidence is 2.6 ±0.3mm. The width increase can be partially explained by the increase in the beam projection onto the MCP surface, and the parallax at 18° caused by the 500 μm thick interaction depth (the thickness of the MCP). Also no guard electrodes were used at the rear of the MCP to make the drift field uniform so the natural electric field would tend to defocus the image. However, these results were encouraging as the PSF broadening obtained with a standard 1atm MWPC would have been much greater [10].

3.5 Discussion

Although the results obtained were encouraging the PSF of the coupled chamber is not good enough to determine whether it is a viable solution to the parallax problem. One of the reasons thought to be responsible for this was the CsI layer on the MCP. If we define the efficiency as the number of output pulses above the noise detected at the anodes over the number of x-ray photons hitting the MCP. By comparing the response of the coupled chamber to that of a calibrated MWPC, the efficiency was measured to

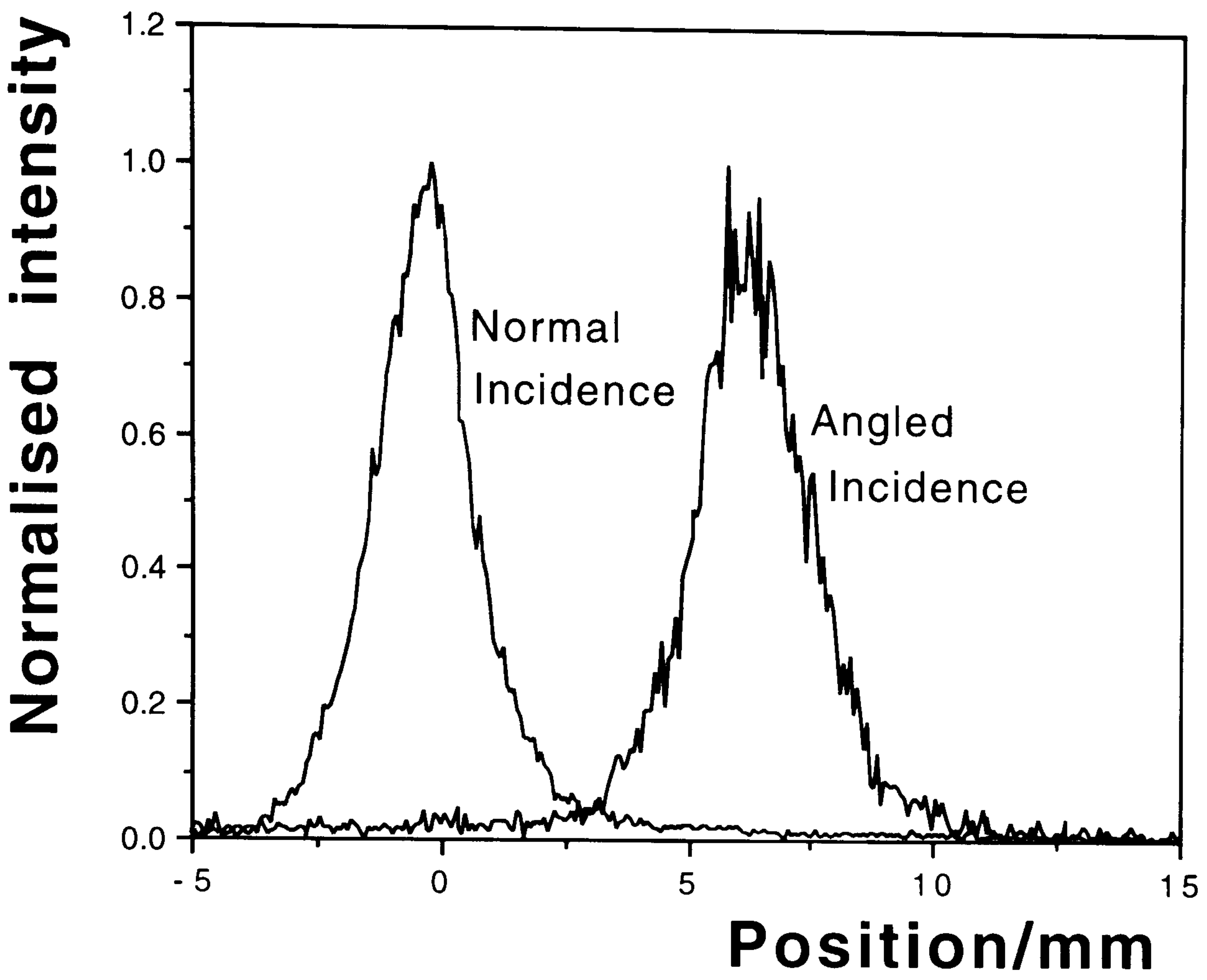

Figure 3.8: Normalised chamber response to both normal and non-normal illumination

be 0.2%. A test on the secondary electron emission (SEE) from the aluminium electrode material inside the window of just the MWPC also showed a similar efficiency. Hence we can determine that the CsI layer on the MCP was not increasing the SEE yield and was therefore not behaving as expected. A possible reason was thought to be atmospheric contamination. On at least three occasions the vacuum rig 'tripped' which allowed the chamber up to atmosphere. Now because CsI is hygroscopic there is a distinct chance that the layer will have been contaminated in some way which will change its characteristics. However in the next section further modifications to the chamber are proposed which may improve the situation.

3.5.1 Future Developments

Modifications to the chamber which may improve the results given in the preceding sections include a larger coated MCP - the present MCP had an active area of only 300mm^2. This should alleviate some of the problems with the electric field behind the MCP making for a more uniform drift field. A lower working pressure to improve the performance of the MCP and to increase the poor signal to noise ratio - great care will need to be taken in lowering the pressure as when the pressure is lowered there are less gas molecules to ionise and the multiplication factor becomes less. Also as the pressure is lowered, the diffusion of the electrons becomes greater so localising the photon interaction point becomes increasingly uncertain. A more gas tight housing for the detector is also required as over the course of 8 hours in the present design, the pressure of the DME inside the chamber decreased by a factor of two and the chamber ceased to operate, making refilling of the chamber necessary on a daily basis.

Bibliography

[1] R.Kahn, R.Fourme, R.Bosshard, V.Saintagne *An area-detector diffractometer for the collection of high resolution and multiwavelength anomalous diffraction data in macromolecular crystallography* Nucl. Instr. and Meth. A246 (1986) 596-603

[2] C.J.Hall, A.Bazzano, R.A.Lewis, B.Parker, P.Ubertini, J.S.Worgan *Preliminary results from a high-pressure imaging spectroscopic proportional counter* Rev. Sci. Instr. 63(1) (1992) 660-663

[3] A.Breskin, R.Chechik, A.Akkerman, A.Gibrekhterman, V.Elkind, I.Frumkin, A.Notea *Recent developments in secondary emission gaseous x-ray imaging detectors* Nucl. Instr. and Meth. A348 (1994) 207-215

[4] G.W.Fraser *The soft x-ray quantum detection efficiency of microchannel plates* Nucl. Instr. and Meth. 195 (1982) 523-538

[5] G.W.Fraser, J.F.Pearson *Soft x-ray energy resolution with microchannel plate detectors of high quantum detection efficiency* Nucl. Instr. and Meth. 219 (1984) 199-212

[6] P.Lecomte, V.Perez-Mendez *Channel electron multipliers: properties, development and applications* IEEE Trans. Nucl. Sci. NS-25(2) (1978) 964-973

[7] J.Wiza *Microchannel plate detectors* Nucl. Instr. and Meth. 162 (1979) 587-601

[8] G.W.Fraser *The characterisation of soft x-ray photocathodes in the wavelength band 1-300 Å* Nucl. Instr. and Meth. 206 (1983) 251-263

[9] R.Lewis, I.Sumner, A.Berry, J.Bordas, A.Gabriel, G.Mant, B.Parker, K.Roberts, J.Worgan. *Multiwire X-ray Detector Systems At The Daresbury SRS* Nucl. Instr. and Meth. A273 (1988) 773-777

[10] C.J.Hall, R.A.Lewis, G.Fraser, D.Duxbury, J.Pearson, W.Helsby, A.Jones, J.W.Sheldon, B.Parker *An investigation into the use of a microchannel plate as the photocathode for a SEE x-ray detector* Nucl. Instr. and Meth. A392 (1997) 330-335

Chapter 4

Gas Microstrip Type Detectors

4.1 Introduction

The Microstrip Gas Chamber (MSGC) was first introduced in 1988 by A.Oed [1], as a neutron detector, and was further developed by F.Angelini et al [2] to be used for detecting minimum ionising particles (mip's). The development of the detector was an attempt to overcome some of the problems encountered with the Multi-Wire Proportional Chamber (MWPC) such as:

1. The count rate capability, which is governed by the ion collection time.

2. A significant reduction in the spacing between electrodes obtained using precise microelectronics technology

By using very thin wires (10-20 microns), and by reducing the anode-cathode gap, it is possible to improve the performance of the MWPC. In a non-standard design, such as the wire microgap detector developed at the Daresbury Laboratory [3], a significant improvement over conventional wire chambers has been achieved.

The MSGC operates in a similar way to the MWPC but without the electrostatic instabilities that plague MWPCs with very small spacings between electrodes.

4.2 Description of the MSGC

In its basic form, the MSGC consists of an insulating substrate with thin anode and cathode strips on one surface. Typical dimensions of the electrodes are 6-20μm wide anodes, and 30-100 μm wide cathodes. At a distance of 3mm away from the electrode surface there exists a drift cathode which defines the active volume of the detector. On the rear surface of the substrate is often a back cathode (or backplane). A schematic diagram of an MSGC in cross section is shown in figure 4.1.

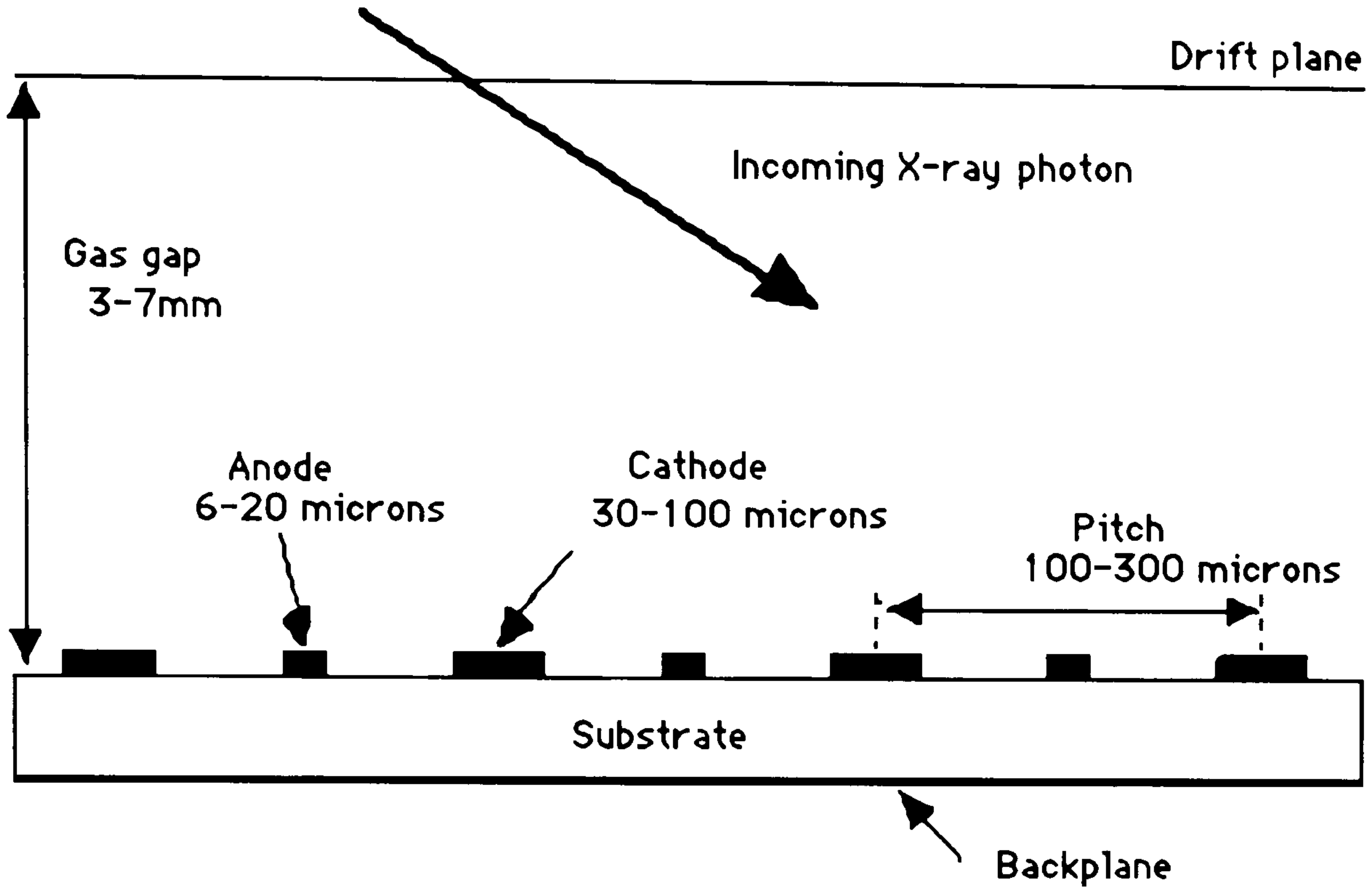

Figure 4.1: Schematic of MSGC.

The surface cathodes are typically 0.5-1.5μm thick and made of either aluminium, gold or chromium. The pitch of these electrodes is of the order of 100-300μm. The drift cathode, which is typically 3-7mm from the surface cathodes is generally made from some aluminised material like mylar or polyester. The backplane is usually of the same material as the surface electrodes or is part of the substrate (see next section). The active volume between the drift plane and surface electrodes is filled with an appropriate gas mixture, dependent upon the detector application. As an example of the different applications let us consider two cases.

1. X-ray imaging applications.

2. Tracking in a high energy physics experiment.

In the first case where the absorption of the majority of the x-rays is necessary, a gas or gas mixture with a high absorption coefficient i.e. a large atomic number, is required so that the detector has a high efficiency of detection. In the second case a large atomic number is not crucial, but a gas mixture with a fast ion collection time is required.

4.3 Detector Operation

The detector operation can be visualised in the following way. When an x-ray photon enters the gas volume it collides with gas atoms losing all of its energy through ionisation processes in the gas, see section 2.2. The electrons created then drift towards the surface electrodes under the influence of an applied drift field (generally set at 3-10kVcm^{-1}) supplied by the drift plane cathode. By suitable application of potentials on the surface electrodes (typically anode voltage 0 V and cathode voltage -400-700 V) a dipole field is created above the surface. At about 200 μm above the surface of the substrate the dipole field becomes dominant, see figure below, and avalanche multiplication of the electrons occurs. By choosing the electrode potentials carefully proportional gains of the order of a few thousand can be realised. A schematic diagram of the electric field in the MSGC is shown in figure 4.2, showing both the drift field and the dipole field. The electrons formed in the avalanche induce a signal on the anodes, whereas the positive ions created in the avalanche, due to their smaller mobility, take a longer period of time to drift towards the surface cathode (100 to 1000 times more). This movement of charge induces a signal on both the anodes and the cathodes and it is this signal which enables one to detect the incoming photon.

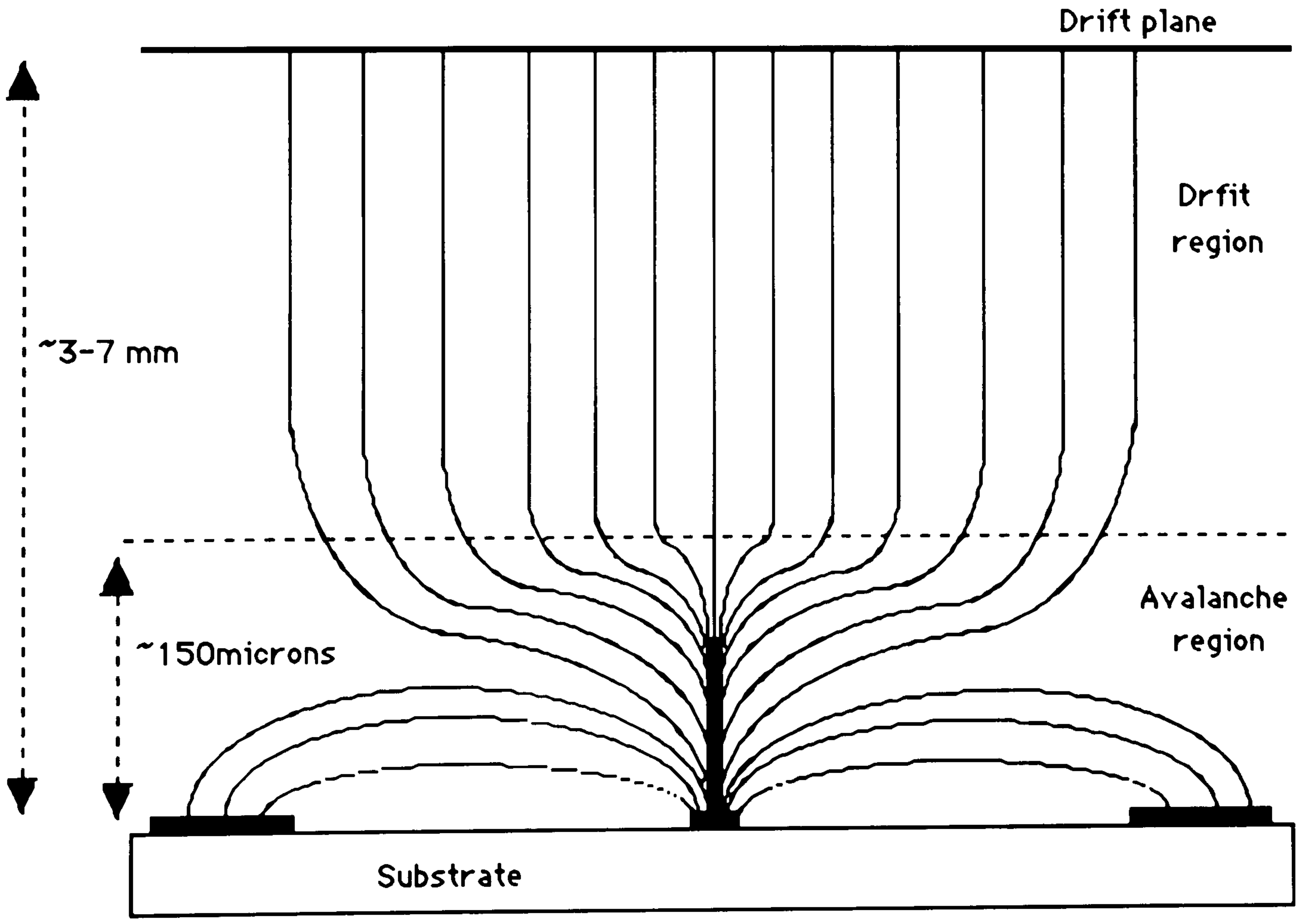

Figure 4.2: Schematic of typical electric field in an MSGC.

4.4 Multilayer MSGCs on silicon substrates

The choice of substrate for MSGCs has seen the most extensive amount of research carried out on such detectors in order to solve the problems caused by unstable operation. Early in the development of the MSGC [1] it was found that insulating substrates charged up due to positive ion accumulation on the substrate surface. This had the effect of reducing the gain of the chamber and ultimately led to unstable operation. In order to combat this effect, substrates were made with conducting surfaces to sweep away any ions which were deposited on the surface. These substrates can be of two distinct designs: homogeneous or multi-layer. The homogeneous substrate, or bulk substrate, is usually a suitable glass and can be divided further into categories according to the dominant conduction mechanism:

1. ionic - where the conducting elements are mobile alkali ions like Na, K etc.

2. electronic/semi-conducting with low alkali concentration such as S8900 glass [4]

The multi-layer substrates represent attempts to achieve the desired surface conductivity's whilst not increasing the conductivity of the substrate bulk. These can also be classified according to when the metallisation took place i.e. pre-photolithography where the conductive layer is produced before the metal strip is deposited and post-photolithography where the conductive layer is added after the metal deposition. The MSGCs developed at Liverpool and described in this thesis are of the multi-layer, pre-photolithography type and their design and fabrication is described in the next section.

4.4.1 Detector design, fabrication and assembly

The first step in the design of a device using microelectronics technology is the design of the electrode pattern to be produced. This is carried out at Liverpool using CAD facilities. The design is subsequently made into a mask (which is effectively a stencil with the desired electrode pattern) and is then used at the manufacturers' to produce the device. Various electrode geometries, including radial (keystone) [5] and split cathodes [6] have been tested at Liverpool over three processing runs. However, in this thesis only two processing runs will be considered and one mask design consisting of five different structures. Table 4.1 shows the specifications for the electrode geometries. Also included in the design of the mask are various test structures which are used for measuring strip capacitance, strip resistance and surface resistivity. The masks are made using electron beam lithography techniques on a soda lime or borosilicate glass plate. (In fact these masks formed the actual detector substrate in the early days of research on MSGCs). The masks used for the fabrication of the detectors described in this thesis were manufactured by Compugraphics International Ltd [7]. The detectors tested at Liverpool were manufactured on a standard industry silicon wafer by Hughes Microelectronics Europa Ltd (HMEL [8]), and the advantages of using silicon over other substrates are listed below :

Structure	**Pitch** (μm)	**Anode width** (μm)	**Cathode width** (μm)	**Anode-Cathode Gap** (μm)
S1	200	10	70	60
S2	200	8	70	61
S3	200	6	70	62
S4	200	8	78	57
S5	100	6	26	34

Table 4.1: Electrode geometries for Liverpool MSGC.

1. Standard industry techniques are used so there are no extra costs in the processing as compared to glass substrates

2. The processing technique is well understood, controllable and reproducible

3. More options are available to achieve the desired properties i.e. doping and implantation

4. There is profit from advancement in silicon technology in size and cost

5. The process produces what are effectively very thin detectors, making implementation of 2d readout possible (however extra processing steps are required)

6. There is potential for the front end electronics to be incorporated onto the same wafer.

The various steps required for the creation of the substrate are shown schematically in figure 4.3. The substrate is formed on a 100mm diameter 500 μm thick silicon wafer.

A layer of SiO_2 is then deposited by means of chemical vapour deposition (CVD). In order to achieve a faster deposition rate, plasma enhanced CVD (PECVD) was used for the growth of the SiO_2 layer on the wafers to a thickness of the order of 3 μm. The

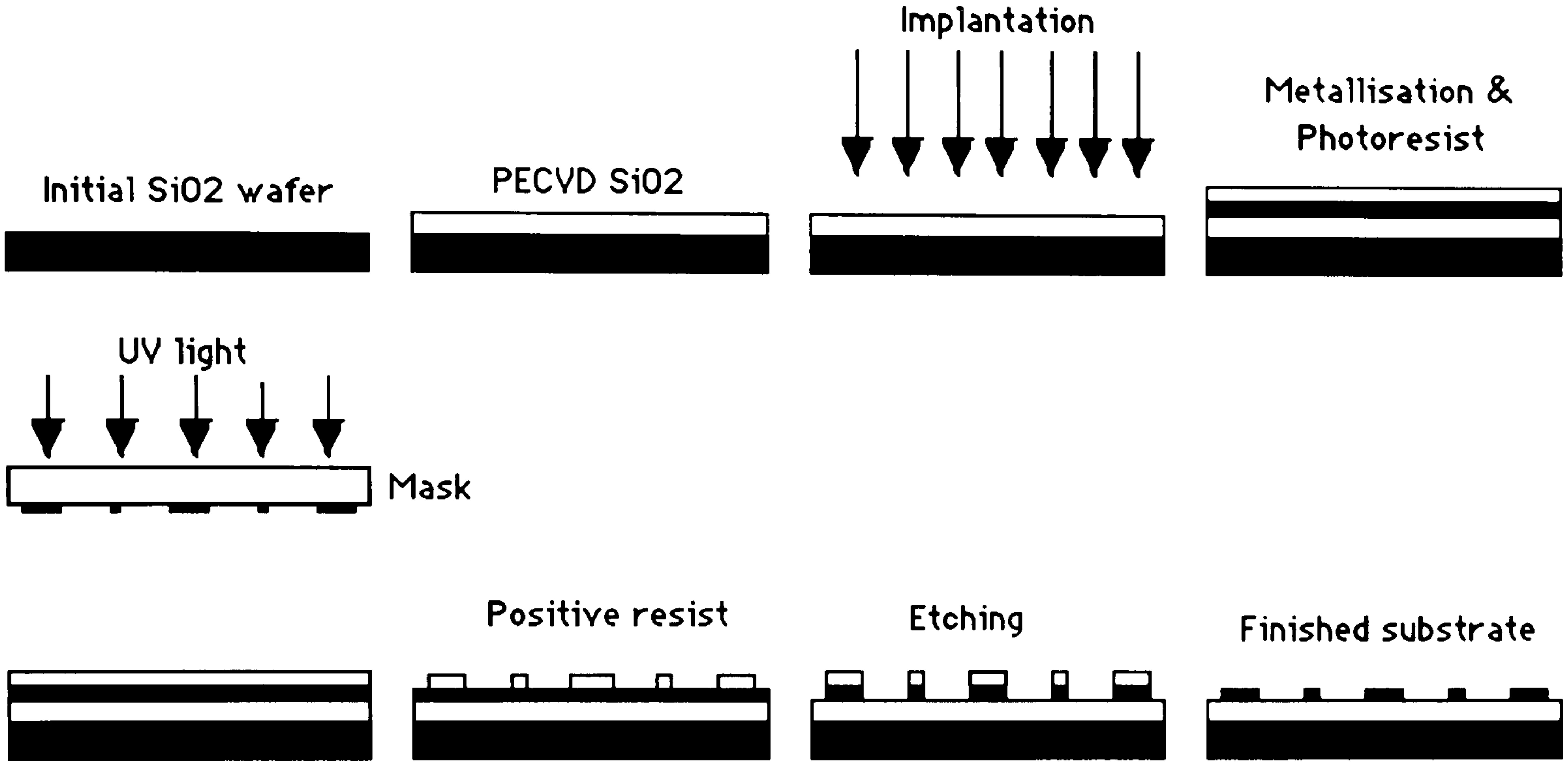

Figure 4.3: Schematic diagram of the substrate manufacturing process for the silicon multilayer MSGC

surface resistivity of the oxide layer is high enough for charging of the substrate to occur due to charge flow along field lines terminating on the anode-cathode gap [6]. In an attempt to avoid this surface charging the top layer of the oxide is doped to make it more conducting. Boron ions are used in this process as it is a standard procedure in the semiconductor industry, and the boron ion implantation energy and concentration can be well controlled. The dopant atoms are introduced into the material by accelerating them to a high velocity and implanting them by virtue of their kinetic energy. For the wafers used at Liverpool, the boron ions used had an energy of 80 keV and from [9] we can determine that the projected range of the boron ions is $0.25\mu m$. The ion concentration was varied between 2×10^{16} and 6×10^{16} ions/cm^2. A summary of the various implant doses is given in table 4.2. A cheaper alternative to ion implantation, suggested by HMEL, is to deposit a thin film of phosphorous doped silica glass (PSG) on to the oxide, which is achieved by altering the composition of the reacting gases during the CVD process. Several wafers were produced with the PSG layer so a comparison between the two could be undertaken. The thickness of the PSG layer was of the order of 1 μm. Once the conductive layer is added the wafer is coated with $1.4\mu m$ thick aluminium. Following the metallisation, a layer of photoresist is then added. The resist is then exposed to UV light through the electrode defining mask. Hence a photoresist structure is defined on the wafer which is identical to the required electrode structure. The wafer is then etched to remove unwanted metal and diced producing a central substrate with the electrode pattern and several test structures which can be used for capacitance and resistivity measurements. They are then cleaned to remove the remaining photoresist and sent to Liverpool. It is important to keep the wafers as clean as possible to avoid getting dust or dirt on the surface of the substrate which could adversely effect the performance of the detector. Once the wafers arrive at Liverpool they are stored in a clean room under a dry nitrogen atmosphere to await assembly which is performed in a custom built clean room. The procedure for the assembly is outlined below :

Batch	**Wafer number**	**Implant Dose** (Boron ions/cm^2)
B2	N2-N4	PSG
B2	N6-N8	4×10^{16}
B2	N9,N10,N12	6×10^{16}
B3	N1-N5	4×10^{16}
B3	N6-N7	PSG
B3	N8-N10	4×10^{16}

Table 4.2: Details of implant doses for batch 1 and batch 2 wafers.

1. Separation of active electrode region from test structures and cut-offs

2. Cleaning of wafers in an ultrasonic cleaner to remove any loose flakes of silicon produced from the dicing

3. Cleaning of wafer with propan-2-ol, methanol and de-ionised water

4. Scanning of wafer under microscope for any defects

5. Gluing of wafer on to printed circuit board (PCB) using in house built jigs and microscope for alignment

6. Baking of wafer in oven at 120^{0}C to remove excess moisture

7. Application of passivation layer (Epotek 905 [10]) over the ends of the electrodes to increase resistance to breakdown

8. Wire bond chosen region and readout electronics with manual ultrasonic wire bonder

9. Perform final checks and re-clean using alcohol's and de-ionised water if necessary

10. Clean and place drift plane in position inside gas windows.

The PCB used in the laboratory tests has been described elsewhere [11], but for the tests undertaken at Daresbury the PCB was redesigned so that it would be compatible with the multiwire linear data acquisition system used at Daresbury [3]. The main difference between the two PCBs is that in the laboratory tests groups of 10-20 anodes are ganged together and read out whereas in the new PCB the anodes are read out individually. In redesigning the PCB a new housing was also made and both designs can be found in section 7.4. Throughout the remainder of this thesis the following naming convention shall be used: "B" refers to the batch number (2 or 3); "N" refers to the wafer number; "S" refers to the structure used (1 to 5). So, B3N2S1 refers to a batch number 3 substrate, boron ion implanted (4×10^{16} ions/cm^2) and structure number 1 (200 μm pitch, 10 μm wide anodes, 7 μm wide cathodes).

4.5 The Silicon Microgap Detector

As was mentioned in section 4.4 extensive research has been carried out in trying to determine the optimum substrate for MSGCs. [12,13,14]. The microgap detector (MGAP), introduced by Angelini et al [15], represents an attempt to construct an MSGC type detector with as small an insulator as possible between anode and cathode. In this way the insulator plays little or no part in the operation of the detector and so the problems associated with substrate charging are completely removed. A cross section of the microgap structure is schematically shown in figure 4.4. The significant differences compared to the microstrip structure are threefold.

1. The anode and cathode are separated by a very thin ~2-4 μm, insulating oxide.

2. The surface cathode covers the whole of the substrate surface

3. The substrate material is now completely irrelevant to the operation of the detector, the only criterion which needs to be satisfied is that the substrate be compatible with the manufacturing process.

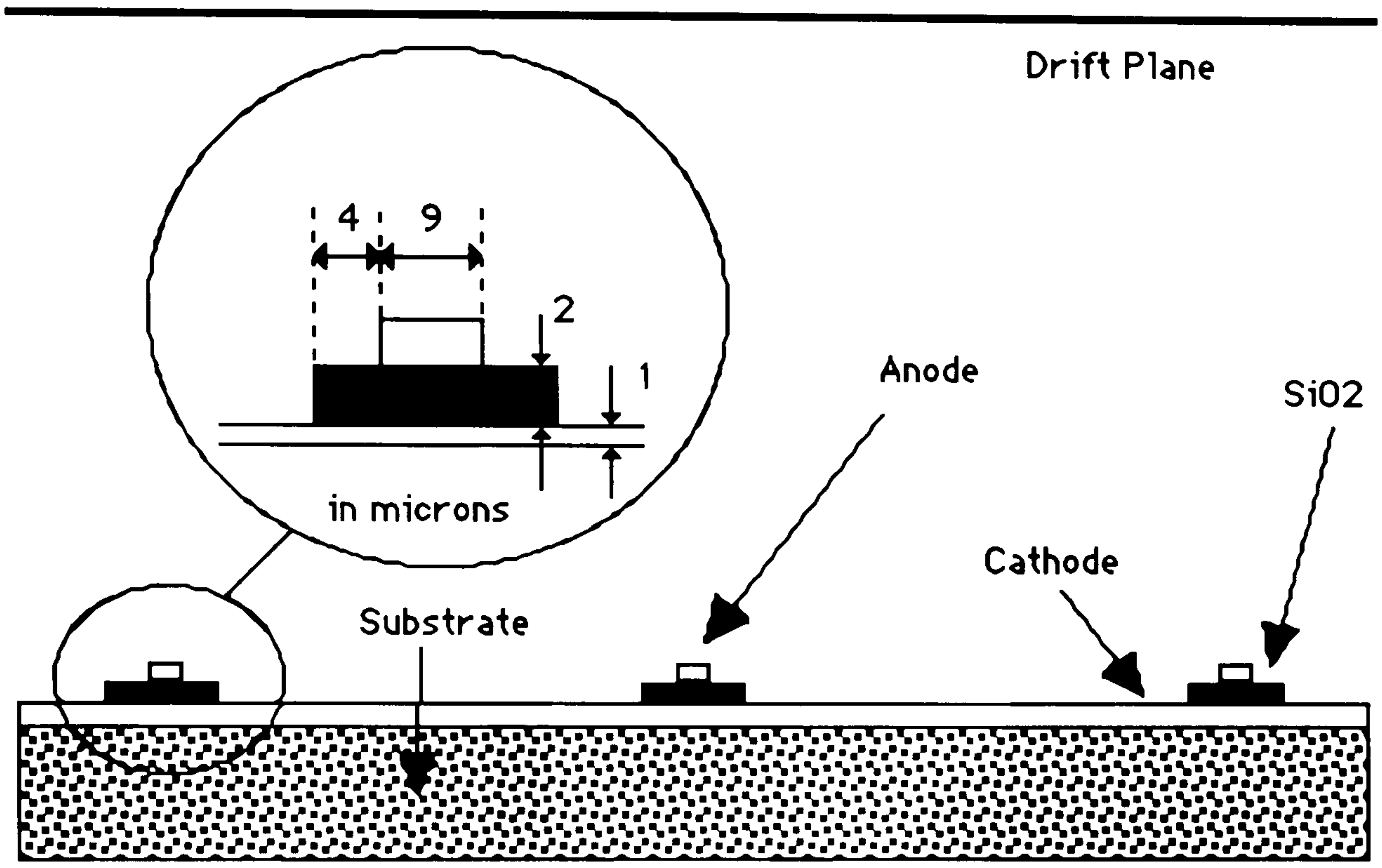

Figure 4.4: Schematic diagram of Microgap structure.

The detector is also manufactured on a silicon processing line in a similar fashion to the SiO_2 MSGC. In essence the microgap detector can truly be thought of as an ultra-miniaturised MWPC. The advantages of such a structure are obvious. In the first case because of the very close proximity of the cathode to the anode practically all the ions created in the avalanche region will be collected on the surface cathode in a much reduced time so the count rate will not be space-charge limited up to extremely high fluxes. Because the surface cathode is in such close vicinity of the anode, a region of very high electric field surrounds the anode. Hence the gain of the detector should greatly be increased as compared to an MSGC for the same electrode potentials. However a major disadvantage of the MGAP detector arises due to the proximity of the anode to the cathode. UV photons produced in the avalanche can reach the cathode and extract electrons. Therefore to reduce the UV photons mean free path a large amount of quenching gas has to be used.

The microgap detector works in exactly the same way as the MSGC, i.e. a drift region followed by a high dipole field amplification region operated in the proportional mode. The typical electrode potentials are drift cathode -1 to-2.5 kV and potential difference between anode and cathode of between 350 and 450 Volts. The microgap detectors investigated in this thesis were kindly supplied by the INFN Pisa group.

4.6 The Microdot Detector

The microdot detector (MDOT), introduced by S.F.Biagi and T.J.Jones [16] at the University of Liverpool, is a new geometry proposed to provide greater operational stability at higher gains than both the MSGC and MGAP detectors. In MSGC and MGAP detectors, the maximum avalanche gains are limited to below gains of 5×10^3 by the onset of breakdown due to geometrical properties. This breakdown is observed primarily at the ends of the anodes and cathodes where the electric fields are much greater than in the main body of the detector. Normally, this is compensated by some form of passivation layer or shaping of the ends of the electrodes to suppress breakdown. The theory is that the MDOT detector should not suffer from this due to its intrinsically circular geometry. Extensive numerical simulations of this new geometry have shown that the MDOT offers several advantages over the existing MSGC and MGAP geometries [16] and these will be discussed in section 4.6.2. In section 4.4.1 it was mentioned that one of the advantages of producing MSGCs on a silicon processing line was the benefit from the advancement in silicon technology. This is crucial in the MDOT design as it exploits these capabilities through the use of a buried readout bus (see next section).

4.6.1 The Microdot Geometry

The basic geometry of the microdot structure is shown schematically in figure 4.5. The anode dots vary between 12-20μm in diameter and the cathodes are between 20 and 40μm wide. The cathode ring starts at a radius of 85 μm. The dots are assembled in a hexagonal packing structure and read out on a pitch of 200 or 100μm. The anode dots are connected by a via to the readout bus which is buried in the oxide layer. The surface of the insulating substrate is doped to a higher conductivity than the bulk to reduce charge up effects and the currents flowing in this layer control the field gradients across the substrate. There are some obvious similarities between the geometry of this structure and that of the gaseous pixel chamber [17,18], however the microdot is smaller in surface area by about a factor of a hundred. The processing steps used in the manufacture of the substrate are outlined below:

1. The first oxide layer is deposited onto the silicon bulk to a depth of 2μm

2. Metal 1 is deposited and etched to define the readout bus structure

3. A second layer of oxide is deposited to a depth of 1.8 μm

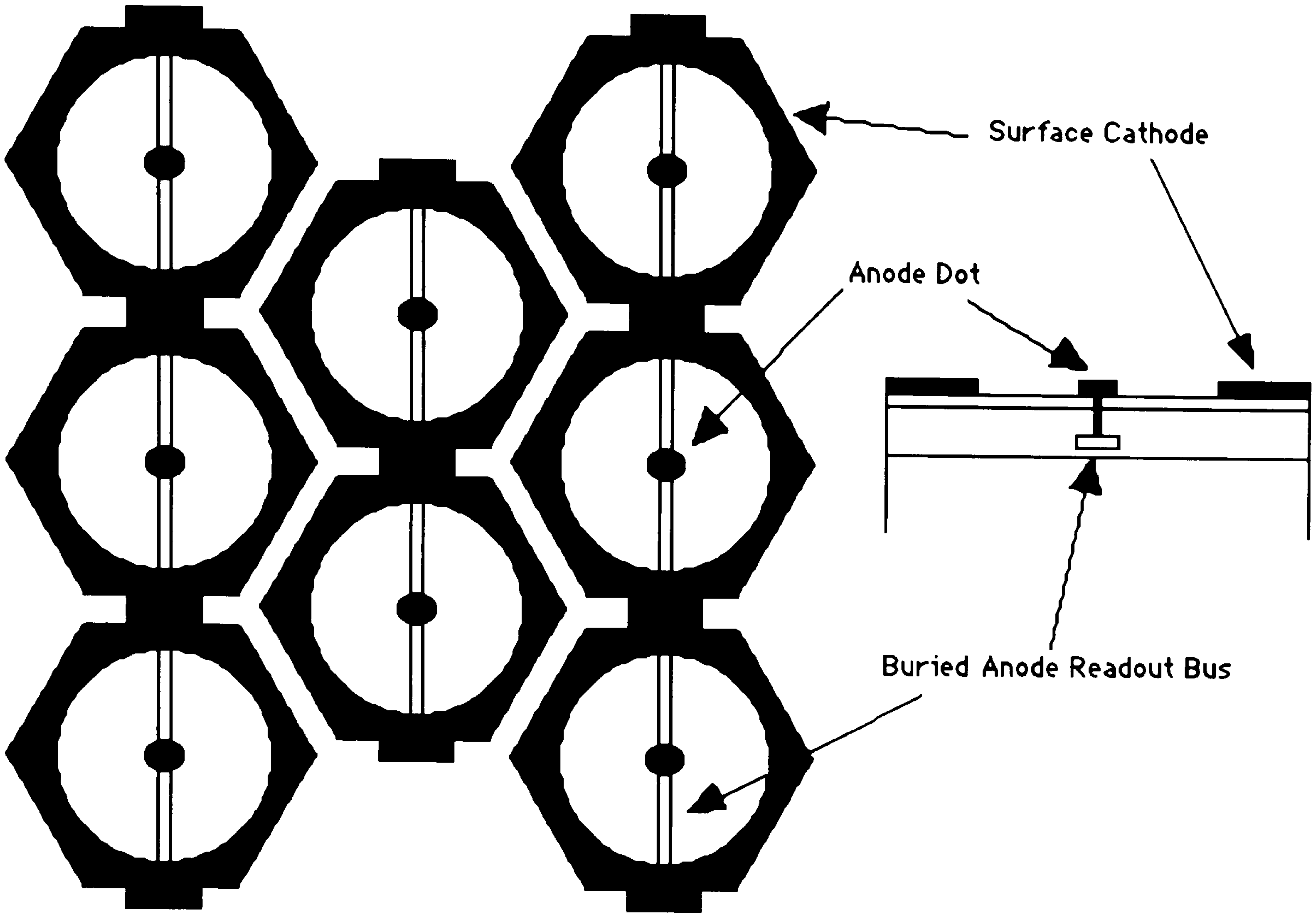

Figure 4.5: Schematic view of MDOT detector in cross section and in plan view

4. The surface is ion implanted
5. The oxide is via etched
6. Metal 2 is deposited and etched defining the electrode structure

The microdot structures were manufactured by HMEL [8]. The same procedures for cleaning and assembly were followed as for the MSGC outlined in section 4.4.1. Summaries of the implant doses and the various geometries are given in tables 4.3 and 4.4 and abbreviations for the various structures are also given. In the case of the structures "H16" the H signifies that instead of a circular shaped cathode, a hexagonal cathode structure is used. The maximum electrode separation therefore corresponds to the distance from the anode edge to the vertex of the hexagonal cathode. Similarly the minimum separation corresponds to the midpoint between two vertices. The "a" and "b" at the end of the abbreviation indicate the difference between the radii of the "back dot", see figure 4.6.

Wafer Number	**Implant Dose** (Boron ions/cm^2)	**Floating Rings?**
1	PSG	No
2	PSG	Yes
3,4	2×10^{16}	No
5,7,9	4×10^{16}	No
6,8,10	4×10^{16}	Yes

Table 4.3: Implant doses for first batch of MODTs

Structure	**Readout pitch** (μm)	**Anode Diameter** (μm)	**Anode-Cathode Gap** (μm)
D20V6a	200	20	75
D20V6b	200	20	75
D16V6a	200	16	77
D16V6b	200	16	77
D12V6	100	12	28.5
H16V6a	200	16	max 88.4, min 75.5
H16V6b	200	16	max 88.4, min 75.5

Table 4.4: Electrode geometries for various MDOT structures

4.6.2 Expected Operation of the Microdot

As noted in [17] the electric potential around a dot or pixel falls off as 1/r whereas in the MSGC the field falls off like a wire as log(r/R). This is true if the electrodes are on an insulating substrate, however if the substrate is conducting, it tends to act as a potential divider between the anode and cathode. In the case of the MSGC there is a mismatch between the field driven by the geometry and that of the linear potential divider [19]. In the case of the microdot, the field from the geometry and that of the quadratic potential divider are much better matched. It might be expected therefore that the instabilities due to the accumulation of electrons or ions on the substrate surface would be much reduced compared to that expected in an MSGC. The gain stability of the microdot may therefore be superior to that of the MSGC.

However, further simulation [20] showed that the buried anode readout bus created a high field region between the bus and the surface cathode at the point where they intersected. This showed that there was insufficient shielding current flowing in the conductive layer and a modification to the substrate design was incorporated to compensate for this effect. This modification was the placing of a metal ring in the gap between anode and cathode. The potential of this ring is not fixed but is allowed to 'float'. The effect of the ring is to compress the field lines further on to the anode dots which helps to focus the electrons formed in the avalanche on to the dots as opposed to the surface of the substrate directly above the underlying bus. We should therefore expect to achieve higher gains for the substrates produced with these floating rings. Results from these detectors and a more detailed explanation will be given in chapter 7. In the abbreviations for the different structures in table 4.4, those substrates which had the floating ring incorporated into their structures are signified with an R, i.e. D12V6R where the V indicates the diameter of the via to the readout bus. Figure 4.6 shows a typical structure of one of the dots with a floating ring. The width of the ring in the first batch of detectors was 5 μm. The position of the ring, with respect to the centre of the dot is given in table 4.5.

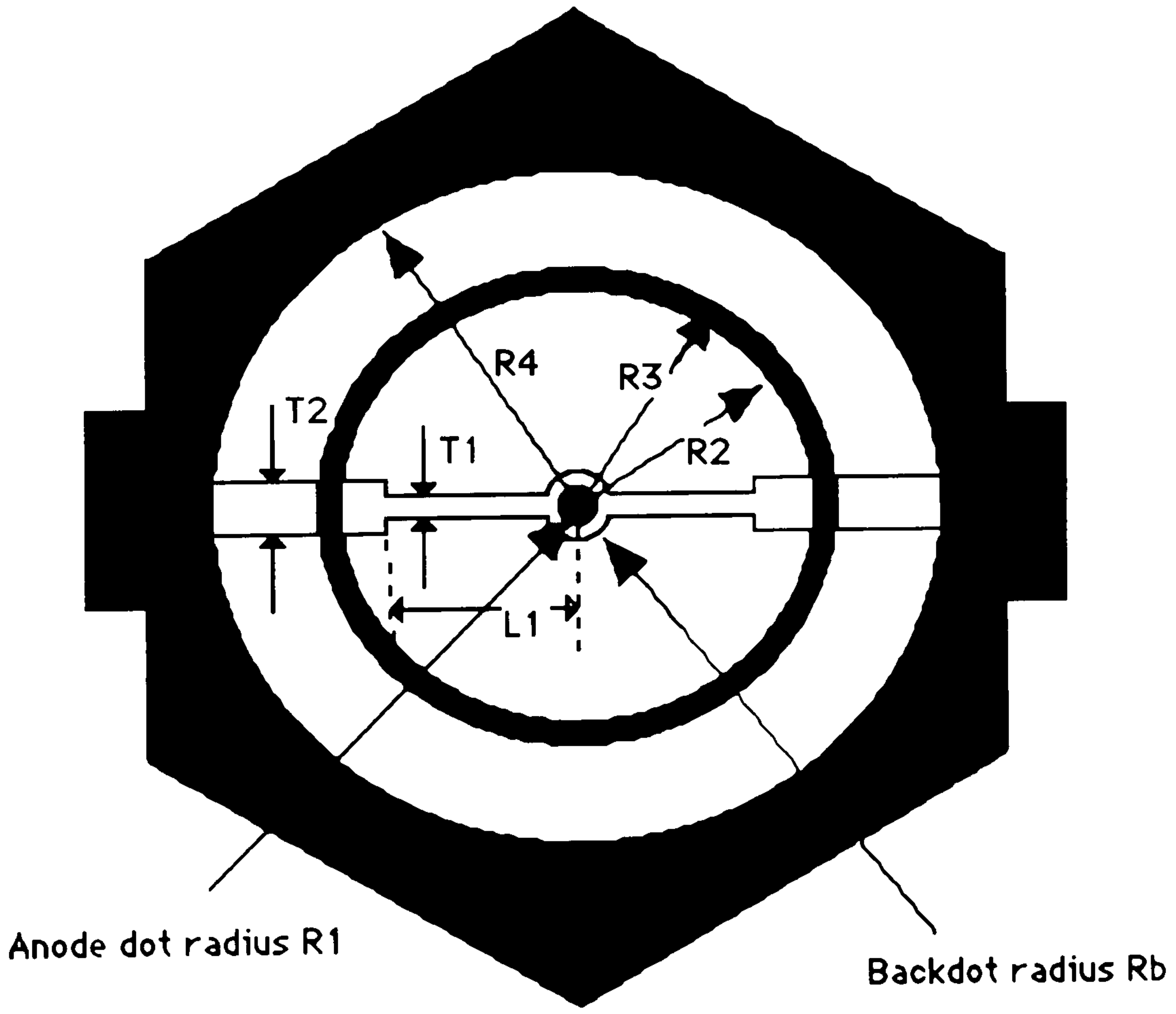

Figure 4.6: Detailed picture of MDOT structure with floating ring.

Structure	**R_v** (μm)	**R_b** (μm)	**R_1** (μm)	**R_2** (μm)	**R_3** (μm)	**R_4** (μm)	**T_1** (μm)	**T_2** (μm)	**L_1** (μm)
D20V6R	3	7	10	46	51	85	6	12	42.5
D24V6R	3	13	12	51	56	85	6	12	42.5
D16V6Ra	3	6	8	51	56	85	6	12	42.5
D16V6Rb	3	11	8	46	51	85	6	12	42.5
D12V6R	3	4.5	6	26.5	31.5	42.5	6	8	34.5
H16V6Ra	3	6	8	51	56	*	6	12	42.5
H16V6Rb	3	11	8	46	51	*	6	12	42.5

Table 4.5: Variations in structures for wafers with rings. * because of hexagonal cathode varies from 83.5 to 96.4. R_v indicates the radius of the via; R_b the radius of the back dot; R_1 the radius of the anode dot; R_2 the distance from the centre to the inner edge of the ring; R_3 the distance to the outer edge of the ring; R_4 the distance to the inner edge of the cathode; T_1 the width of the inner part of the readout bus; T_2 the width of the outer part of the readout bus and L_1 the distance from the centre of the dot to the transition from thin to thick readout bus (see figure 4.6).

Bibliography

[1] A.Oed *Position sensitive detector with microstrip anode for electron multiplication with gases* Nucl. Instr. and Meth. A263 (1988) 351-359

[2] F.Angelini, R.Bellazzini, A.Brez, M.M.Massai, G.Spandre, M.R.Torquati *A microstrip gas avalanche chamber with two-dimensional readout* Nucl. Instr. and Meth. A283 (1989) 755-761

[3] R.A.Lewis, N.S.Fore, W.Helsby, C.Hall, A.Jones, B.Parker, I.Sumner, J.S.Worgan, C.Budtz-Jorgensen *High counting rate gaseous x-ray detectors for synchrotron radiation applications* Rev. Sci. Instr 63(1) 1992 642-647

[4] T.McMahon, J.Wilson, T.Jones, I.Duerdoth, N.Lumb, J.Baines, D.Botterill, R.Edgecock, R.English, B.Payne, P.Bignall, G.Crone, M.Esten *A study of the rate dependence of the gain of gas microstrip detectors with glass substrates in high intensity particle beams* Nucl. Instr. and Meth. A348 (1994) 361-364

[5] S.Kiourkos, S.F.Biagi, T.J.V.Bowcock, T.J.Jones, J.N.Jackson *Comparison of experimental measurements and electrostatic simulations of keystone geometry microstrip gas chambers* Nucl. Instr. and Meth. A348 (1994) 351-355

[6] S.F.Biagi, J.N.Jackson, T.J.Jones, S.Taylor *Initial investigations of the performance of a microstrip gas-avalanche chamber fabricated on a thin silicon-dioxide substrate* Nucl. Instr. and Meth. A323 (1992) 258-262

[7] Compugraphics International Ltd., Glenrothes, Scotland, UK

[8] Hughes Microelectronics Europa Ltd., Glenrothes, Scotland, UK

[9] K.A.Picker *Ion-implantation silicon physics, processing and microelectronic devices* in *Applied solid state science*, vol.5, Academic, N.Y. 1975

[10] Epoxy Technology Inc., Billerica, MA, U.S.A.

[11] S. Kiourkos. *Development of Microstrip Gas Chambers for High Energy Physics Experiments* University of Liverpool, PhD thesis 1995

[12] R.Bouclier, J.J.Florent, J.Gaudaen, G.Million, A.Pasta, L.Ropelewski, F.Sauli, L.I.Shekhtman *High flux operation of microstrip gas chambers on glass and plastic supports* Nucl. Instr. and Meth. A323 (1992) 240-246

[13] J.E.Bateman and J.F.Connolly *Substrate-induced instability in gas microstrip detectors* Rutherford Appleton Laboratory, RAL-92-085

[14] R.Bouclier, G.Million, L.Ropelewski, F.Sauli, Yu.N.Pestov, L.Shekhtman *Performance of gas microstrip chambers on glass substrata with electronic conductivity* Nucl. Instr. and Meth. A332 (1993) 100-106

[15] F.Angelini, R.Bellazzini, A.Brez, M.M.Massai, R.Raffo, G.Spandre, M.A.Spezziga *The micro-gap chamber* Nucl. Instr. and Meth. A335 (1993) 69-77

[16] S.F.Biagi and T.J.Jones *The microdot gas avalanche chamber: an investigation of new geometries* Nucl. Instr. and Meth. A361 (1995) 72-76

[17] D.Mattern, M.C.S.Williams, A.Zichichi *A new approach for constructing sensitive surfaces: the gaseous pixel chamber* Nucl. Instr and Meth A300 (1991) 275-280

[18] D.Mattern, M.C.S.Williams, A.Zichichi *First tests of the gaseous pixel chamber fabricated on a ceramic substrate* Nucl. Instr. and Meth. A310 (1991) 78-81

[19] S.F.Biagi, T.J.V.Bowcock, D.Duxbury, J.N.Jackson, T.J.Jones, S.Kiourkos *A study of the response of thin-oxide MSGCs to minimum ionising particles and low energy x-rays* Nucl. Instr. and Meth. A367 (1995) 193-197

[20] S.F.Biagi, J.Bordas, D.Duxbury, E.Gabathuler, T.J.Jones, S.Kiourkos *First experimental results from a microdot gas avalanche detector integrated onto a silicon wafer* Nucl. Instr and Meth. A366 (1995) 76-78

Chapter 5

Characterisation of the MSGC detector

5.1 Introduction

The behaviour of the MSGC was characterised in terms of its energy resolution, gain behaviour and stability, high rate performance and ageing characteristics. All the results presented for the MSGC have been obtained using the laboratory test set-up which is schematically shown in figure 5.1. Two different readout systems were used depending on the rate at which the MSGC was illuminated. In both cases the signal from a group of neighbouring anodes was input into an Ortec 142AH charge sensitive preamplifier [1] and then fed into a post amplifier. For low rate illumination (less than 100kHz) the Tracor pulse height analyser was used in conjunction with an Ortec 571

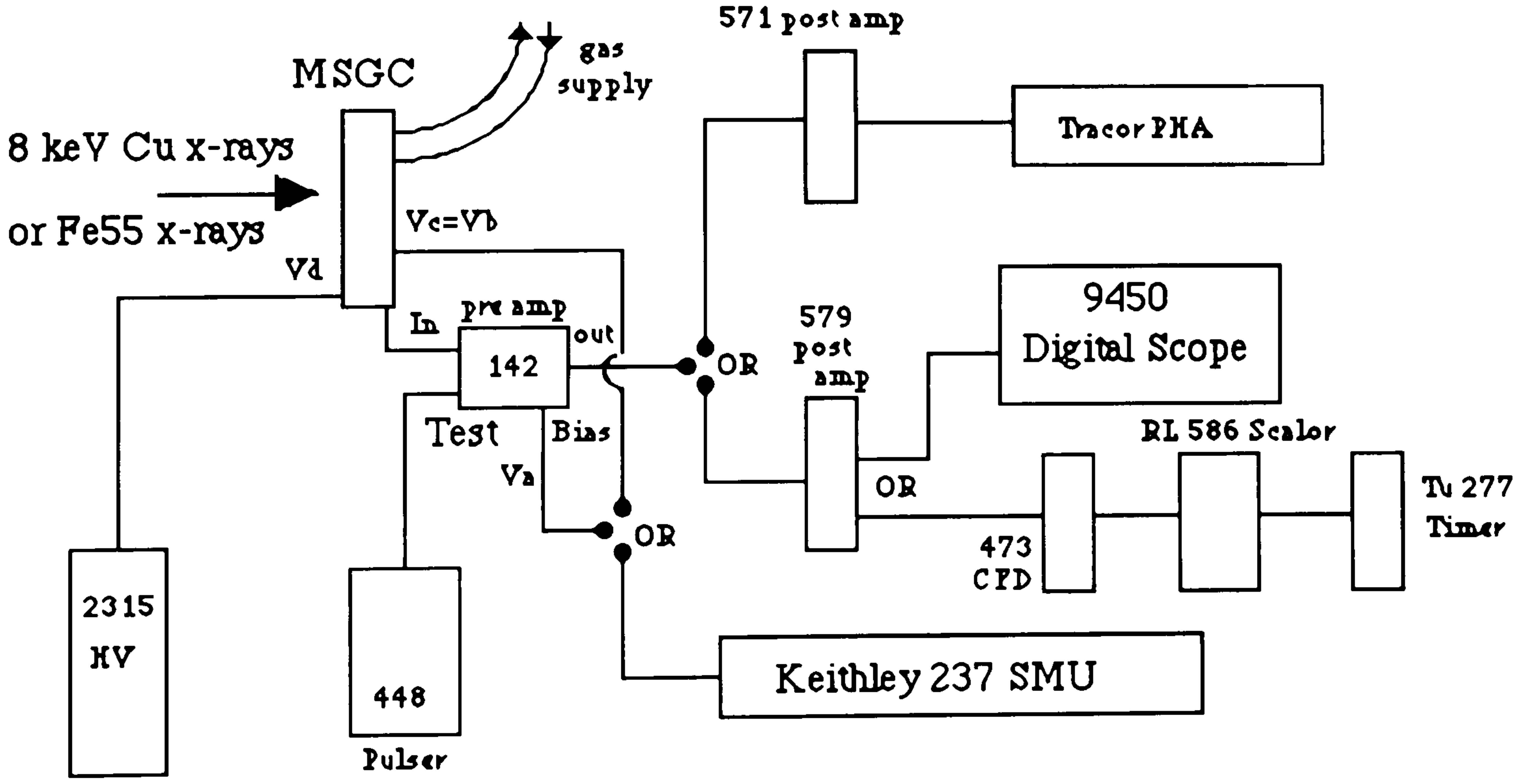

Figure 5.1: Schematic of laboratory test set-up

post amplifier [1]. For higher rates an Ortec 579 post amp [1] and the Lecroy 9450 digital oscilloscope [2] were used because the internal amplifier of the Tracor PHA saturates above 100kHz. Alternatively an Ortec 473 constant fraction discriminator in conjunction with an RL 586 scalar were used to monitor the rate. The negative cathode and backplane voltages were supplied by a Keithley 237 high voltage Source Measure Unit (SMU) [3] which is capable of measuring currents from 0 to 1 μA with an accuracy of 0.04% to 100 nA and 0.1% to 1 μA, and which also allows the setting of a current limit. Alternatively the anodes can be set to a positive voltage and the cathodes and back plane grounded. The drift plane voltage is supplied by a Lecroy 2415 HV supply.

5.2 Energy resolution

Figure 5.2 shows a typical energy spectrum obtained from the MSGC using 8 keV Cu $K\alpha$ x-rays in an Ar:DME 80:20 gas mixture. The spectrum shows that the detector was operating in proportional mode as the escape peak corresponds to an energy of ~5keV. The resulting energy resolution was 17.6% FWHM/peak channel (Full Width at Half Maximum), and was typical of the values obtained using the laboratory setup shown in figure 5.1, for both 8 keV x-rays and Fe^{55} 5.9 keV x-rays (of the order of 15-25%).

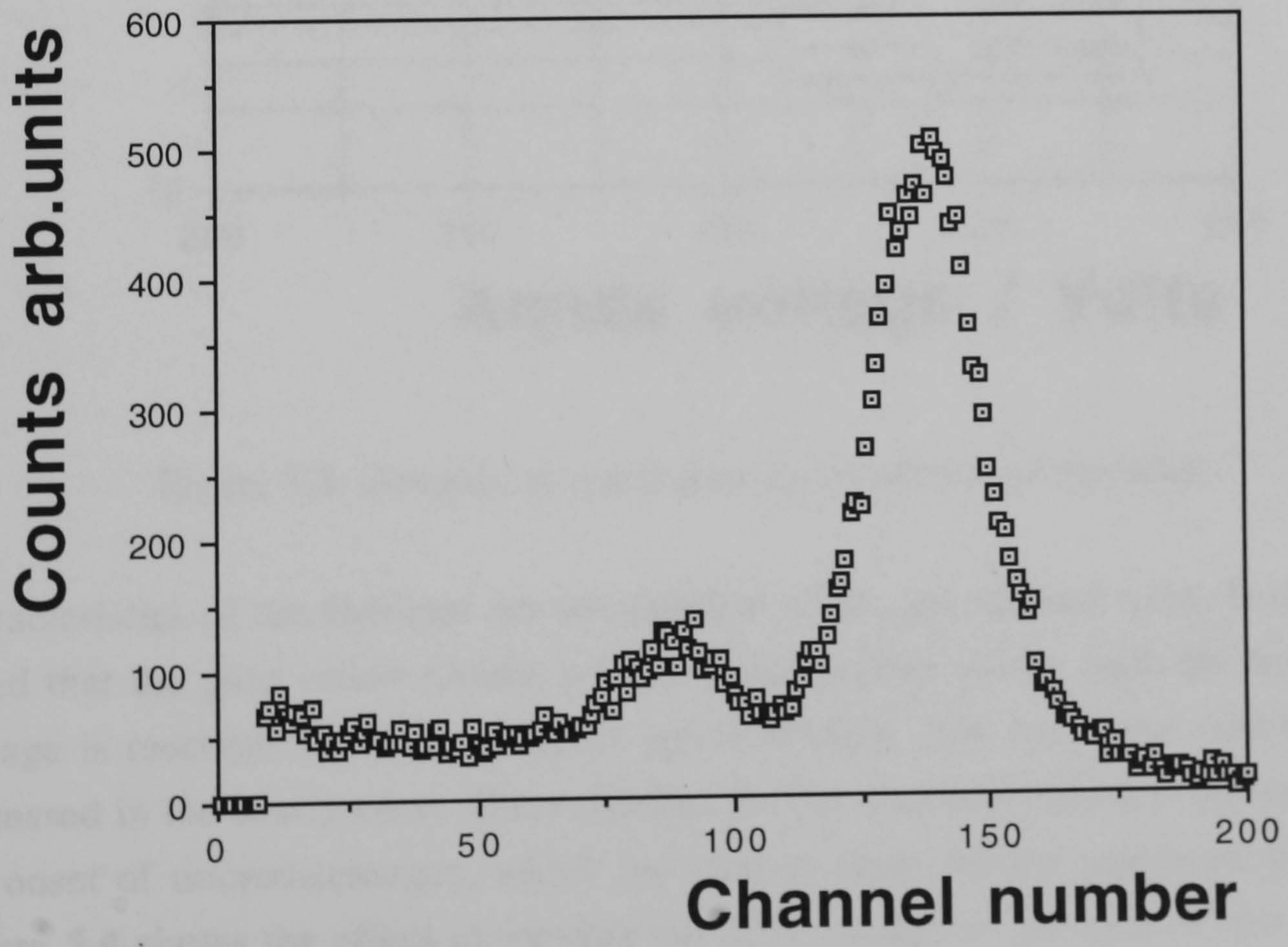

Figure 5.2: Energy spectrum of thin oxide MSGC using 8keV Cu x-rays

5.3 Gain characteristics

The gain characteristics of the MSGCs were investigated using an Fe^{55} source. The gas gain for various cathode voltages of the chamber is compared to a calibration pulser. This pulser injects a known number of electrons into the preamplifier and the signal is then sent through the postamplifier to the PHA. This known number of electrons gives a calibration channel for which the MSGC response can be compared to. Figure 5.3 illustrates the variation of gas gain for argon with various amounts of quencher, in this case dimethyl-ether (DME, chemical formula $(CH_3)_2O$). For the different gas mixtures the slope can be seen to be constant, implying that the gain slope characteristics of the chamber are independent of the gas mixture used. It should be noted that the gain values plotted are the instantaneous values once the full supply voltage is reached. There is a drop of approximately 30% over time which will be discussed in the next section. The endpoints for the Ar:DME mixtures are defined by the onset of microdischarges, which are seen as large current jumps on the SMU. Figure 5.4 shows the effect of varying the drift voltage on the gain of the chamber which clearly shows that there is a contribution to the gain from the drift region. The gain values after the 30% fall are plotted.

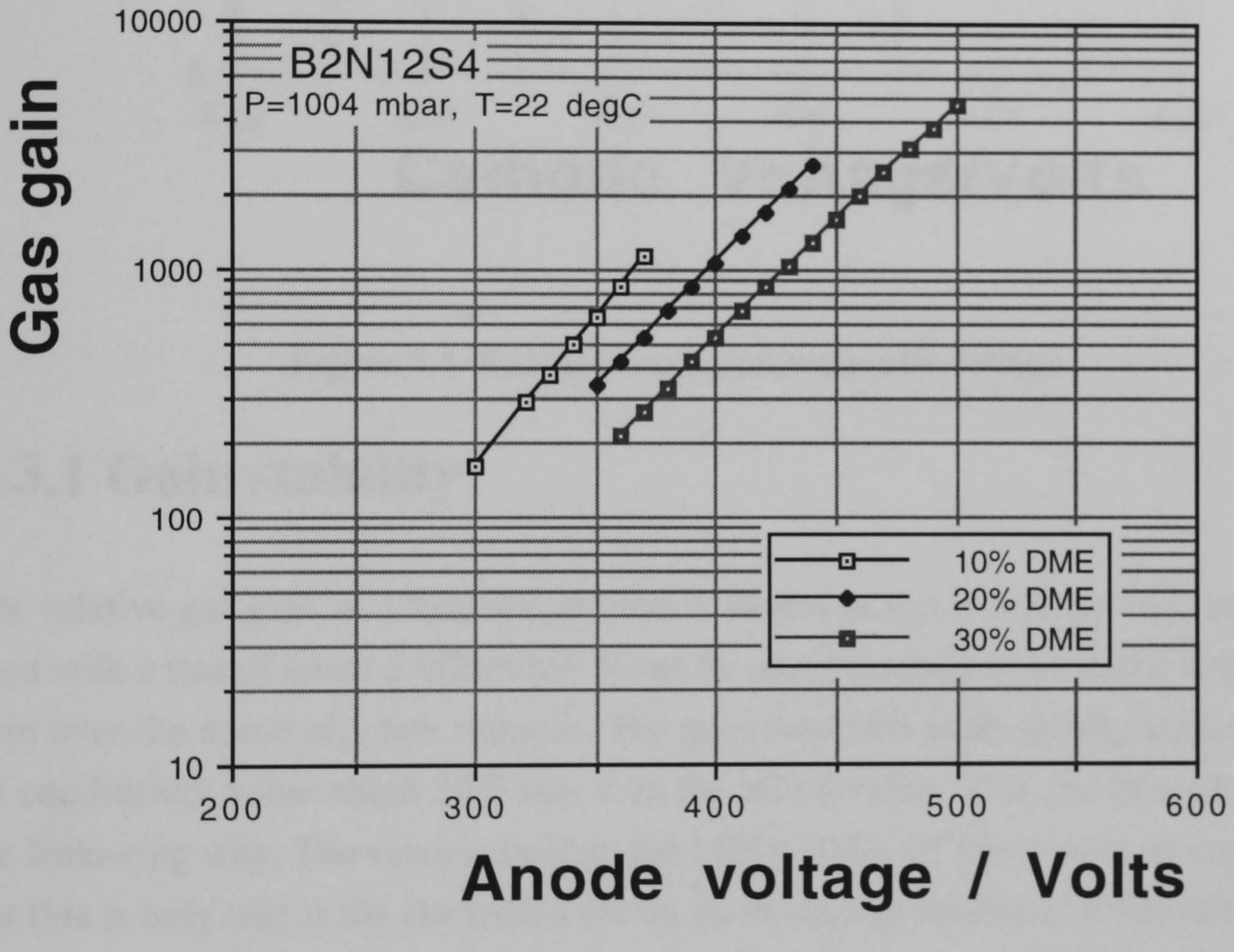

Figure 5.3: Gas gain in argon plus stated amount of quencher

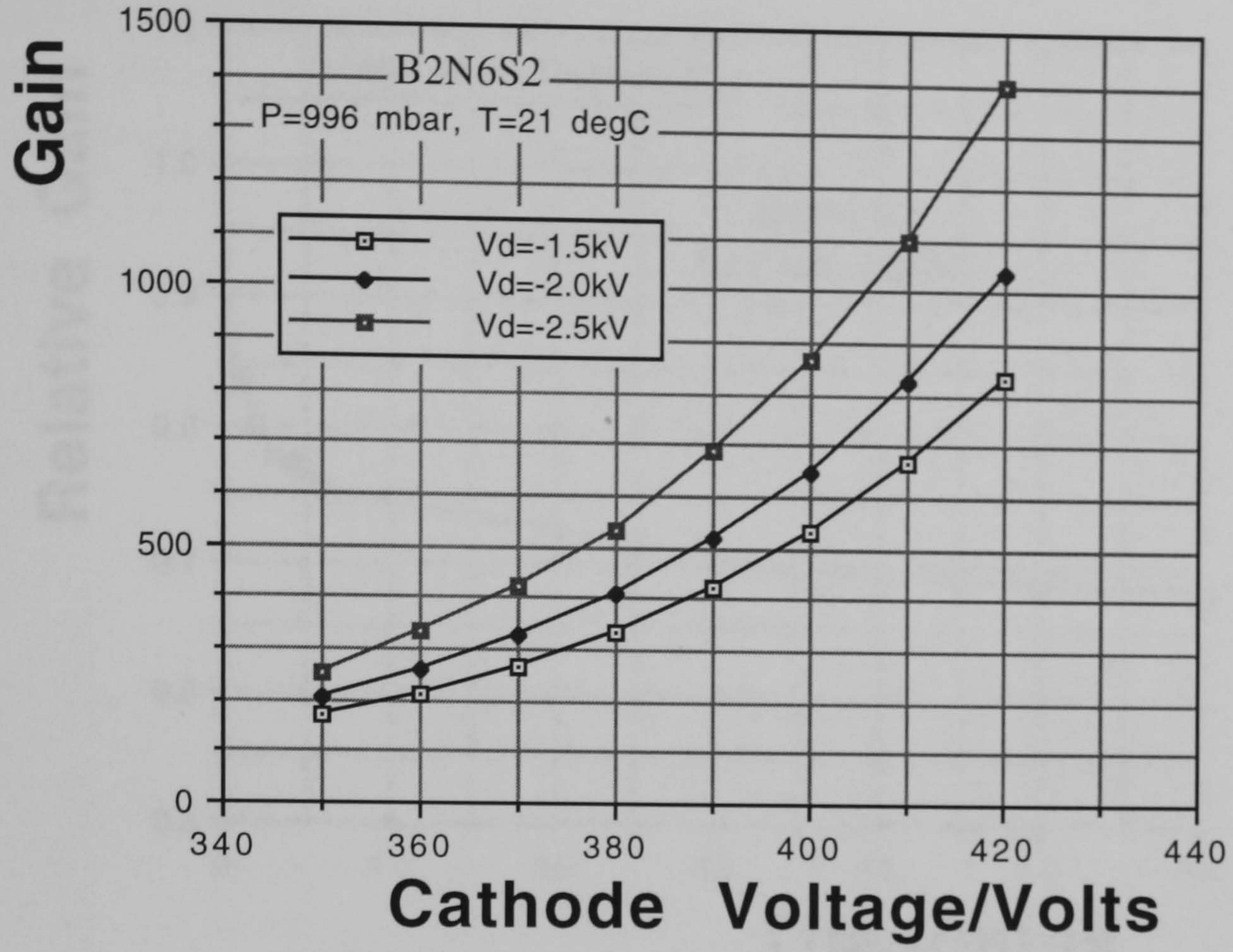

Figure 5.4: Gas gain variation with drift voltage

5.3.1 Gain stability

The relative gas gain as a function of time is shown in figure 5.5. An Fe^{55} source was used with a rate of about 5 kHz/mm^2. It can be seen that there is an initial large drop in gain over the space of a few minutes. The gain then falls more slowly until it reaches an equilibrium value about 30% less than the initial value. This can be understood in the following way. The electric field in the MSGC falls off like a wire as log(r/R) [4], but this is only true if the electrodes are on an insulating substrate. If the substrate has a non zero conductivity then it tends to act as a potential divider across the gap between anode and cathode. In the case of the MSGC there is a mis-match between the field driven by the electrode geometry and that of the linear potential divider [5]. Therefore field lines will cross the gas-substrate interface and electrons or ions will accumulate on the substrate surface. Figure 5.5 shows that after a period of about 60 minutes, at a flux of 5kHzmm^{-2}, a dynamic equilibrium is achieved between the field configuration and the flowing surface current. Figure 5.6 shows that once this equilibrium is established the gain remains nearly constant, with a 6% fall, following further increases in rate up to moderately high rates. If we now compare this behaviour to that of a phosphate glass (PSG) wafer, figure 5.7, we can see that there are considerable differences between the

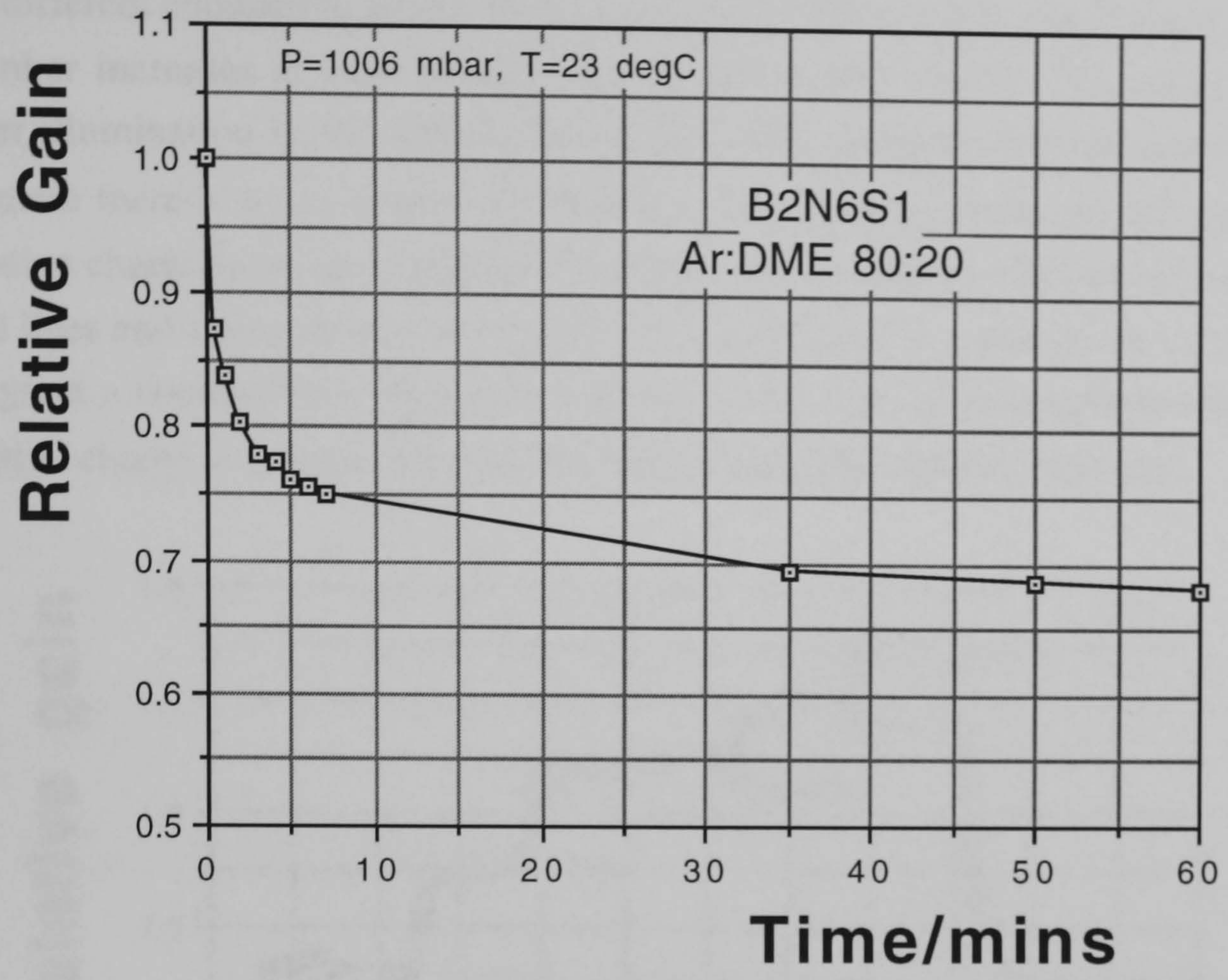

Figure 5.5: Initial gain behaviour of the thin oxide MSGC. Cathode voltage -400V.

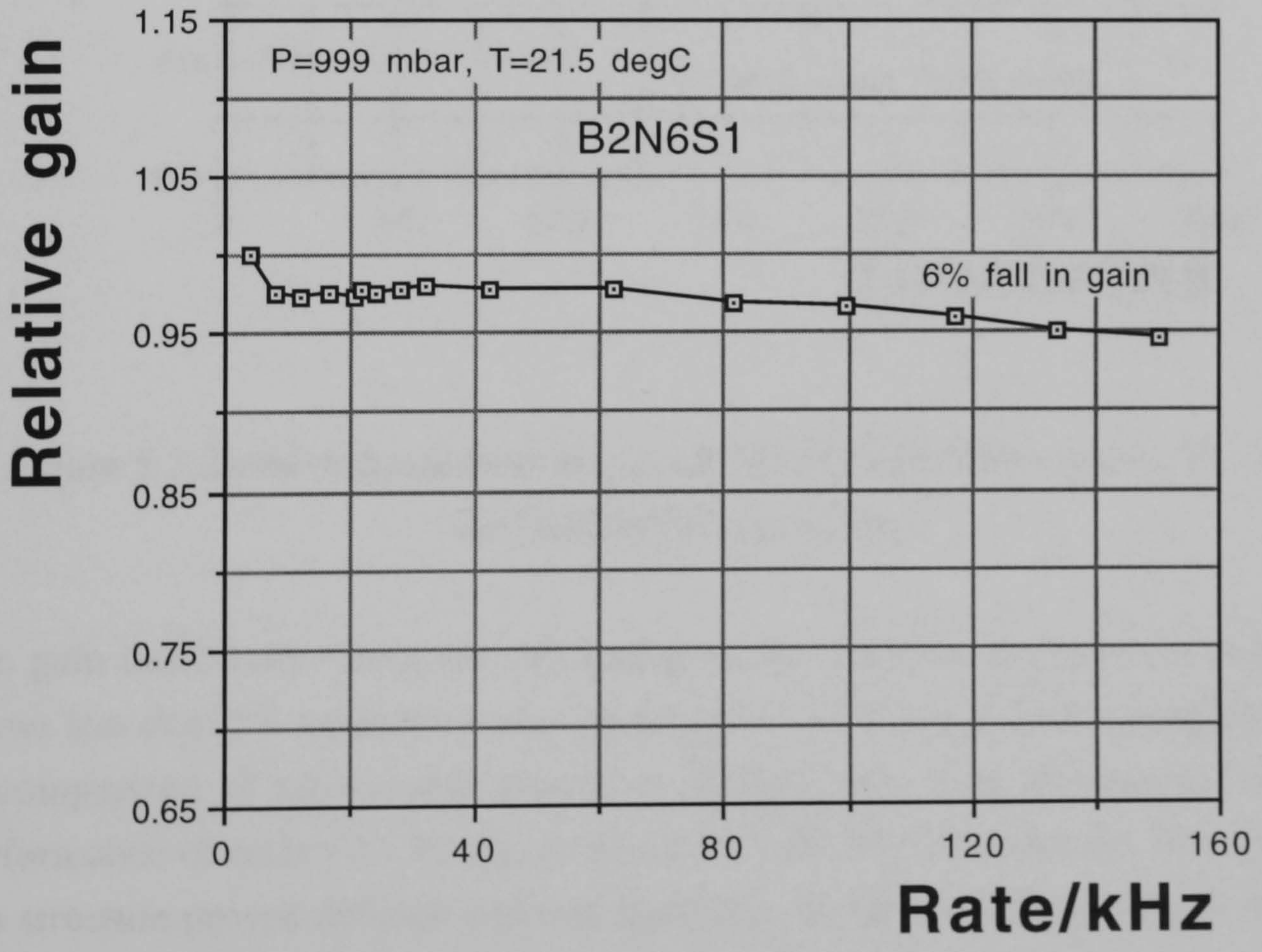

Figure 5.6: Stability of the thin oxide MSGC gain after 'charge up'. Ar:DME 80:20 mixture

two different conductive layers. In the case of the PSG substrate the relative gain of the chamber increases at each increase in rate and is then stable. The initial behaviour under illumination is also different from the SiO_2 substrate. For the case of the PSG substrate there is a rise in gain and then it remains stable. From this we can infer that negative charge is being accumulated on the surface which would reinforce the electric field lines and cause an increase in gain. This behaviour is symptomatic of a layer with too great a conductivity. This is in contrast to the case of the implanted SiO_2 where positive charge is accumulating on the surface causing a reduction in gain.

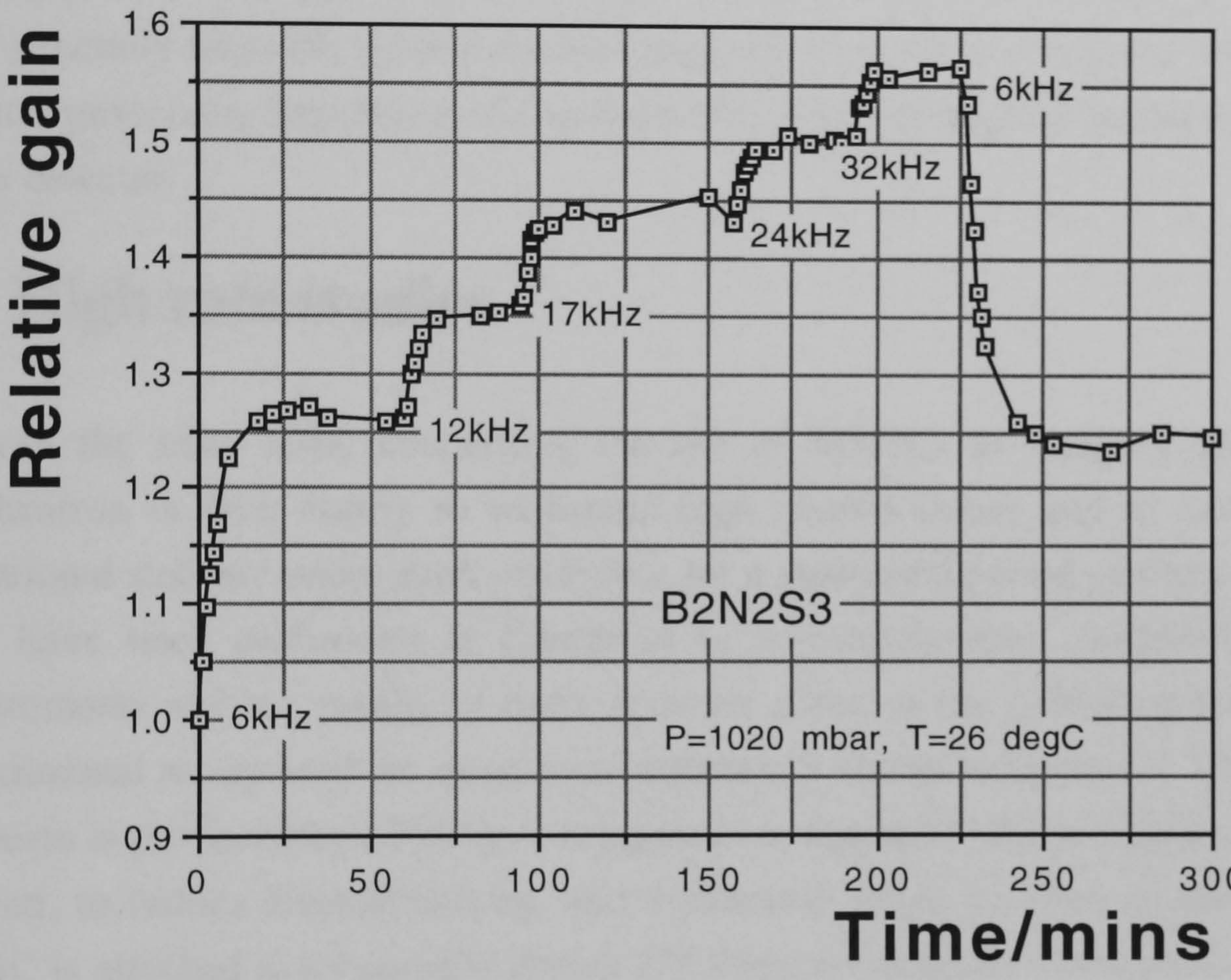

Figure 5.7: Initial behaviour of thin oxide MSGC with PSG coating. Vc=-400V, Ar:DME 80:20 gas mixture.

The gain uniformity along the full length of the detector has been investigated and shows less than 5% variation across its length which is adequate for imaging purposes. A comparison of the various structures showed very little difference between the performance of each with the exception of the 100 micron structure. The operation of this structure proved difficult and was thought to be due to bad lithography making the edges of the strips very coarse which ultimately leads to a greater susceptibility to breakdown.

5.4 Microdischarges and electrical breakdown

When high voltages are applied to the electrodes in order to achieve high gains sudden gas discharges or sparking may occur, resulting in the worst case. to a complete break in the electrode. The spark rate can be reduced by the addition of a gas with high electron affinity such as a freon to the mixture. A further problem in the case of MSGCs and MGAP detectors, is the high field regions which occur at the anode and cathode ends. Attempts to combat discharge at the electrode ends include electrode shaping [6,7] or the application of a protective layer across the ends. This passivation layer generally takes the form of an insulating polymer or epoxy and can be made to be an extra processing step during the manufacture or can be applied during the assembly of the detector.

5.5 High rate studies

Perhaps the main issue concerning the use of MSGCs as imaging devices on a synchrotron is their ability to withstand high photon fluxes and to maintain their operational stability under such conditions for a prolonged period of time. Laboratory tests have been performed at Liverpool to investigate their suitability for such requirements and the results of these tests are given in the following sections. The experimental set-up used for these measurements is shown in figure 5.1. The 8 keV x-ray beam is produced by a Philips x-ray generator equipped with a copper target and is filtered, to reduce Bremstrahlung, and collimated down to 1mm in diameter. The MSGC is attached to a manually driven XY stage allowing for horizontal and vertical scans to be performed in steps of 0.25mm. To allow for variations in the gas mixture, pressure and temperature a single wire proportional chamber (SWPC) is connected in the gas line before the MSGC. A Nanochem^{TM} [8] purification system was also incorporated into the gas line to further clean impurities from the gas. The gas was mixed using a standard CERN rack and distributed to the chamber via polyurethane tubing.

5.5.1 High rate results

In order to evaluate the performance of the detector at high rate it became necessary to monitor the chamber's performance by the current drawn on the anodes. This reading is then normalised to the reading on the SWPC to obtain a relative value of the gain. This is due to a lack of readout system which would cope with the high rates of illumination. Figure 5.8 shows the relative gain of the chamber versus the converted photon rate. The chamber was operated in an 80:20 Ar:DME mixture with the cathodes at -400V and the drift plane voltage at -2kV. The rate performance of a Moscow glass chamber [9] is also shown for comparison. The gain remains constant up to approximately 4 MHz/mm^2, when space charge effects are believed to become dominant. This is where a region of positive ions formed in the avalanche begin to alter the electric field above the strips. It should be noted that at the highest rate the current drawn on the anodes is 470nA and the resulting voltage drop across the 10MΩ resistor in the input stage of the pre-amplifier is of the order of 4.7 volts which corresponds to a gain drop of ~13%. Therefore at rates above about 3.5MHz (~100nA) the data points have been corrected, using the gain versus cathode voltage curves from figure 5.3, to take account of this. The movement of positive ions towards the drift plane is the main contribution to the space charge effect because of their smaller mobility These effects are generally seen when a detector is illuminated at high rate where a large number of positive ions will be formed. In figure 5.9 the fractional currents drawn on the drift plane and the side cathodes are shown and one can clearly

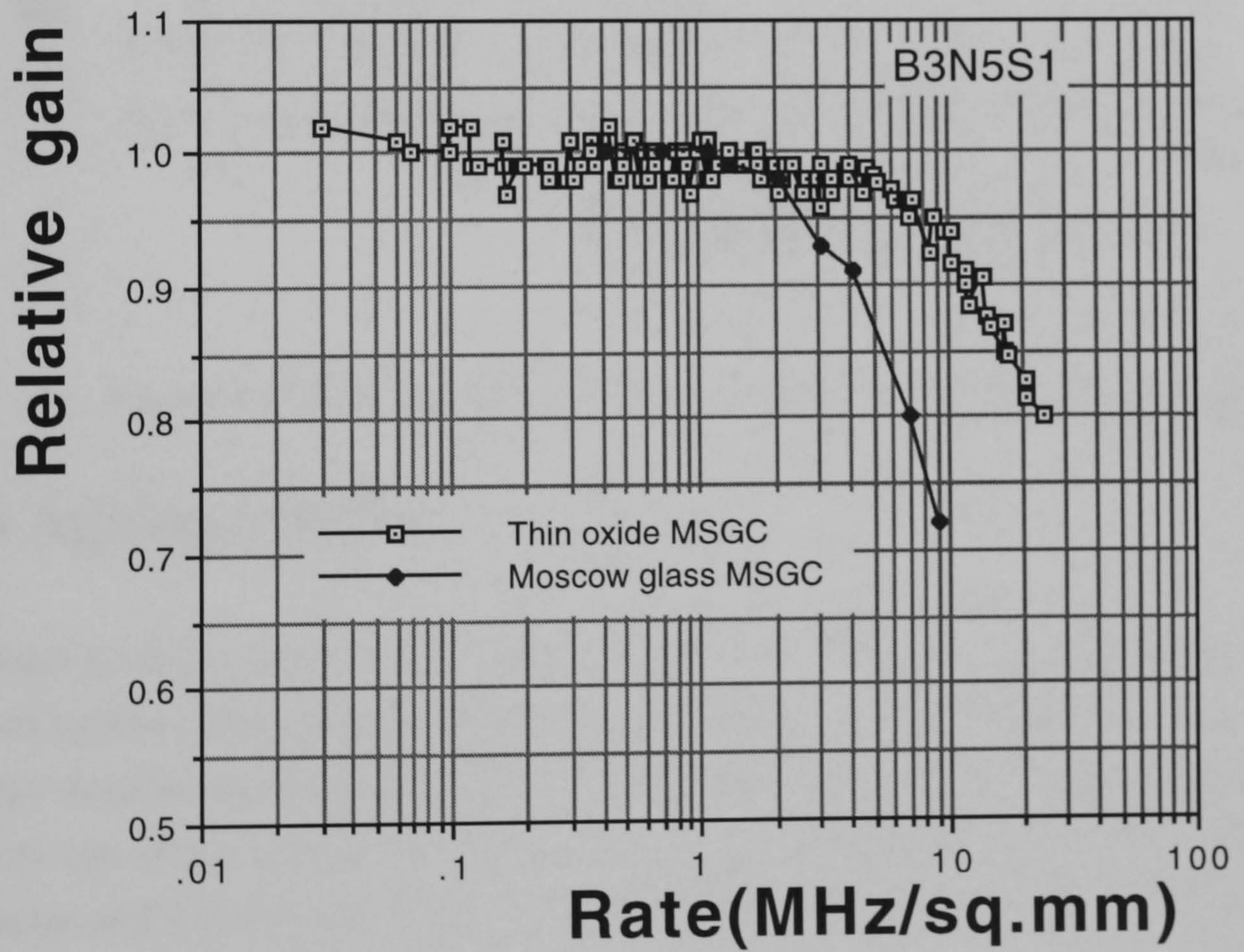

Figure 5.8: Relative gain versus converted photon rate for thin oxide MSGC

see the effects of space charge taking place. The drift plane current is measured using a Keithley 175 multimeter connected to a modified Silena HV unit [10]. The cathode current is measured with the SMU and the anode current is measured with a Keithley 475 picoammeter. At low rates the current fraction flowing to the cathodes is of the order of 26% and to the drift plane ~77%. As the rate is increased this changes to ~31% on the cathodes and ~70% on the drift. The sum of the drift and cathode fractional currents indicates that there is a current component flowing through the substrate.

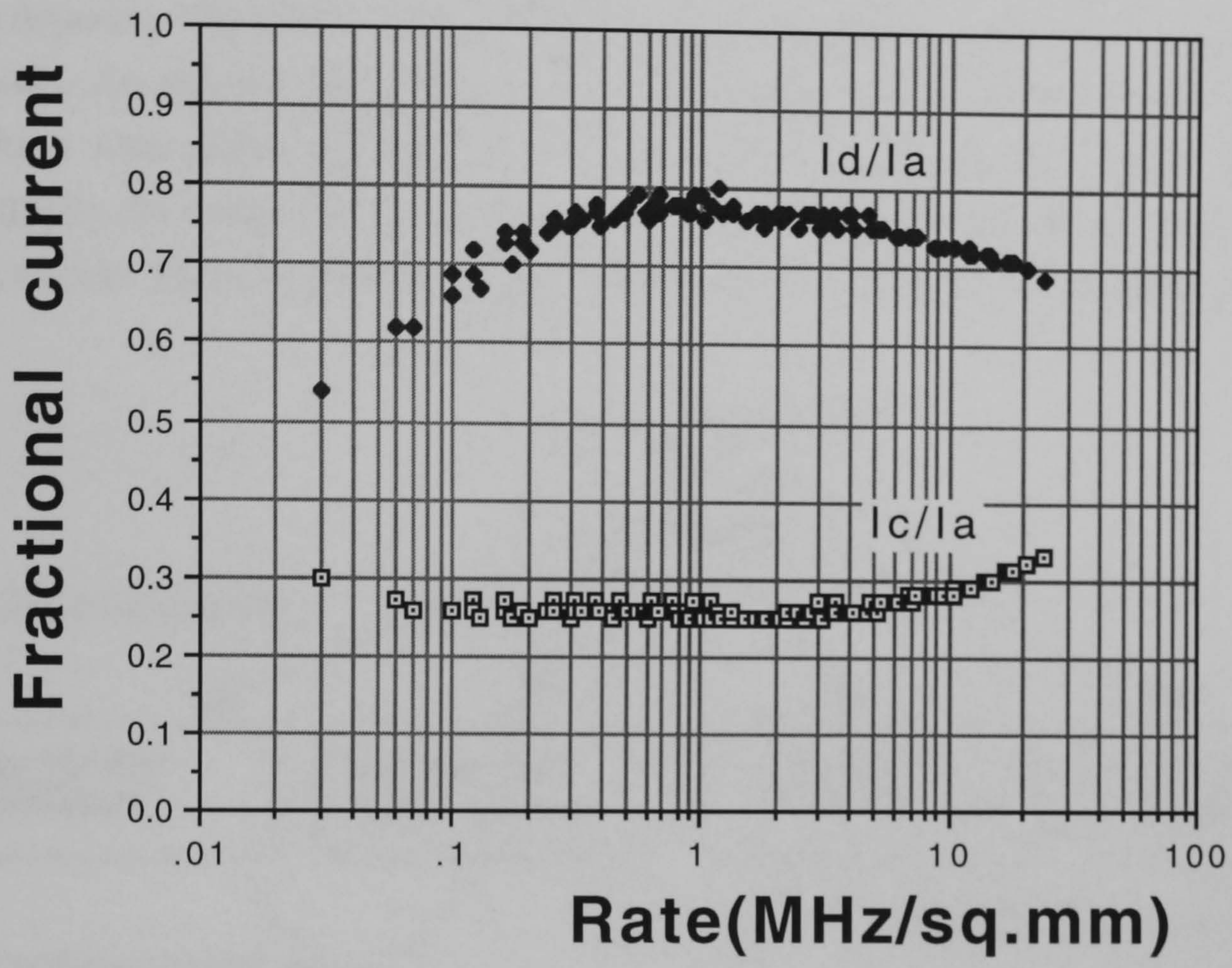

Figure 5.9: Ratio of drift and cathode currents to the anode current

5.6 Ageing studies

A major problem, and probably the least understood, with any proportional counter is that of ageing. This ageing manifests itself in many ways including loss of gain, loss of energy resolution, excessive currents, self-sustained currents and sparking. These effects can all be caused by coating or other degradation of the anode and cathode surfaces, and it is this effect which is thought to be the main contributor to ageing [4].

5.6.1 Ageing effects and processes

During the formation of an avalanche around an anode strip, positive ions, free radicals (neutral or charged) and negative ions (electrons mostly) are produced. Reactions between the chemically active neutral radicals and the ions formed in this 'plasma soup' can occur, which produce further free radicals and can ultimately result in the formation of polymers [11]. The formation of the polymer can begin in the gas, on the electrode surface or begin in the gas and migrate to the surface. In any case the molecular weight becomes so large that the polymer condenses as a solid or liquid onto the strips or the chamber walls. Figure 5.10 is a schematic representation of this polymer formation as caused by these free radicals [12]. As a consequence of such polymer build up various effects which can occur are the Malter effect [13] and thin film deposits. The Malter effect occurs when an insulating coating is deposited on the cathode. An electric dipole layer is formed across the insulating polymer due to the positive ions drifting from the avalanche. This increases the dipole field until eventually the threshold for field emission is exceeded and electrons are extracted from the cathode. These then enter the gas and drift to the anode producing more positive ions from the avalanche which then drift to the cathode. This positive feedback mechanism causes large standing currents, electrical breakdown and discharges even after the voltages have been removed from the electrodes. A further effect which is due to extremely thin deposits [14], but quite separate from the Malter effect, is that some deposits can be photosensitive allowing very low energetic photons, created in the avalanche, to liberate electrons from the cathode. Again resulting in a positive

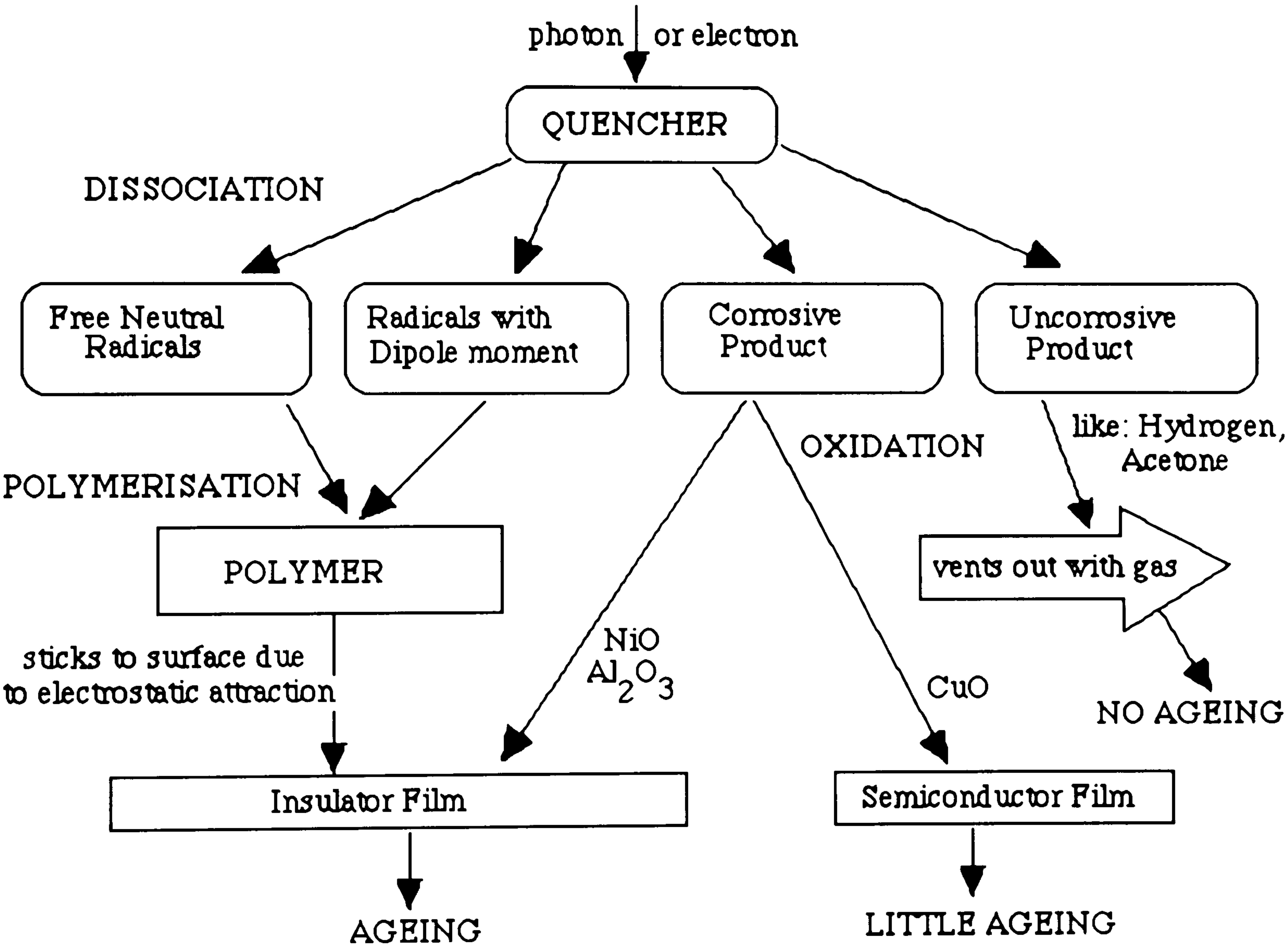

Figure 5.10: Schematic representation of polymer formation, taken from [12].

feedback mechanism and runaway current. This is thought to be due to a lowering of the electron work function.

5.6.2 Chamber construction materials

The choice of materials used in the construction of the MSGC which are in contact with the gases used, has been found to be an important factor in the ageing rate [15,16]. Outgassing from various components used in the chamber construction and in the gas system can increase the susceptibility of deposit formation as described in the previous section. Extra care has to be taken when using DME as it is known to react adversely with various plastics and even some metals [11] and a list of the various components used is given in appendix 1.

5.6.3 Results

Throughout the ageing studies carried out over the last twenty years on wire chambers a convention has been established whereby the ageing is characterised by the total accumulated charge that the detector can sustain without too much gain degradation. So it seems only natural to characterise the MSGCs performance in the same way. The rate of accumulated charge is calculated in the following way [17]:

$$Q(Ccm^{-1}s^{-1}) = \frac{G.n_e.e.R(Hz)}{S(mm^2)}.10\left(\frac{mm}{cm}\right).\frac{1}{n\left(\frac{strips}{mm}\right)} \qquad (5.1)$$

where G is the gas gain, n_e the number of primary electrons, R is the rate, e the electron charge, S is the collimator area and n is the number of anodes in one mm. A more convenient way of expressing equation 5.1 is by using the current drawn in the chamber which is calculated from the charge in one avalanche multiplied by the rate. This is given by $G.n_e.e.R$ and so equation 5.1, for a $200\mu m$ pitch detector, can be written as:

$$Q(Ccm^{-1}) = \frac{I(A)}{S(mm^2)}.2 \qquad (5.2)$$

where I is the chamber current in amps. Thus to calculate the charge acquired becomes just a matter of integrating the current drawn throughout the test. Table 5.1 gives a list of the ageing tests performed with the rate, accumulated charge, substrate used and the initial value of the gain that the chamber was operated at. All the tests listed where operated in Ar:DME 80:20 mixtures except test 6 which was done with Ar:DME 50:50. Tests 2a, b and c are performed on the same spot within the chamber whereas for tests 4 to 7 a different location on the same structure was used. Figure 5.11 shows the relative gain variation with accumulated charge for the seventh ageing test. The gain has been normalised using the SWPC. This shows a drop in gain of approximately 20% for an acquired charge of 54 mC/cm. For all tests except 5 and 6 the chamber was irradiated until either the gain dropped to 80% of its original value or until the chamber was destroyed by either human error or severe loss of gain or energy resolution. Tests 5 and 6 were performed as a comparison of gas mixtures, and figure 5.12 shows the normalised gain of these tests versus dose. As is clear from the graph the relative percentage of DME makes little difference in the ageing rate, although the large fluctuations throughout the test are not fully understood. As well as monitoring the current in the chamber the energy resolution of the detector was also measured periodically at lower rates with the pulse height analyser. Figure 5.13 shows the normalised FWHM to peak channel amplitude ratio for tests 5 and 6. Even though the gain is almost constant (figure 5.12) the FWHM increases by 50% within the first few mC/cm of charge, and this behaviour appears to be typical of MSGCs. Once the ageing tests were complete the chamber was opened up in the clean room and the detector was examined under an optical microscope. In some cases, sparking had occurred resulting in broken strips which ultimately leads to gain deterioration. However in all cases deposits were observed on the electrode surfaces in the irradiated spot. For the seventh test deposits were also seen on the drift electrode with a pattern similar to that of the electrodes. This has also been seen in studies with wire chambers [18].

Test	**Substrate**	**Rate(kHz)**	**Gas gain**	**Acc.Charge(mC/cm)**
1	B2N10S2	150	500	8.0
2a	B2N12S4	250	600	3.0
2b	B2N12S4	400	1000	20.0
2c	B2N12S4	900	1000	12.9
3	B3N3S1	400	1000	33.5
4	B3N5S1a	350	1000	22.9
5	B3N5S1b	350	1000	9.6
6	B3N5S1c	350	1000	9.6
7	B3N5S1d	~12MHz	1000	54.0

Table 5.1: Summary of ageing tests

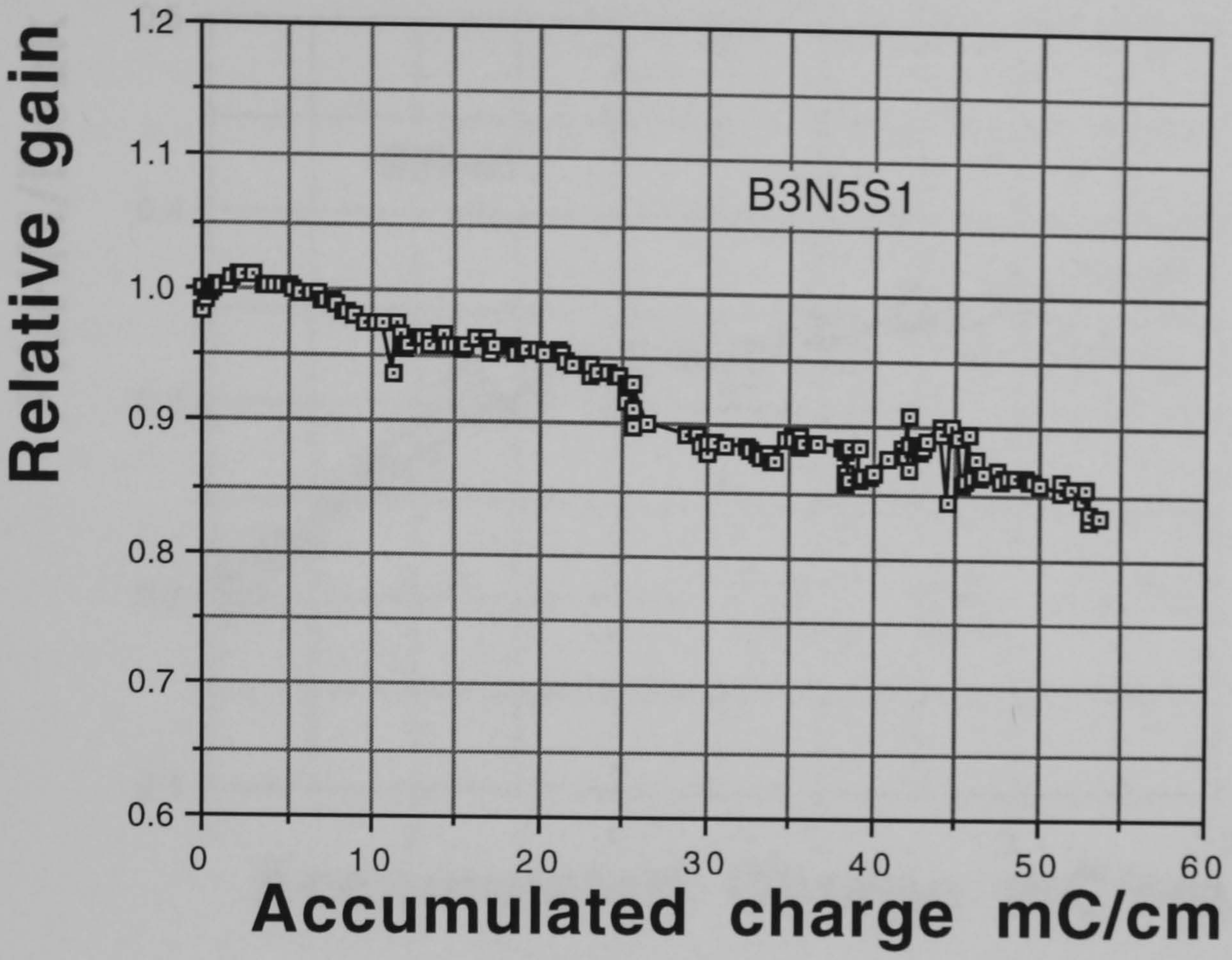

Figure 5.11: Relative gain as a function of accumulated charge for 7th ageing test

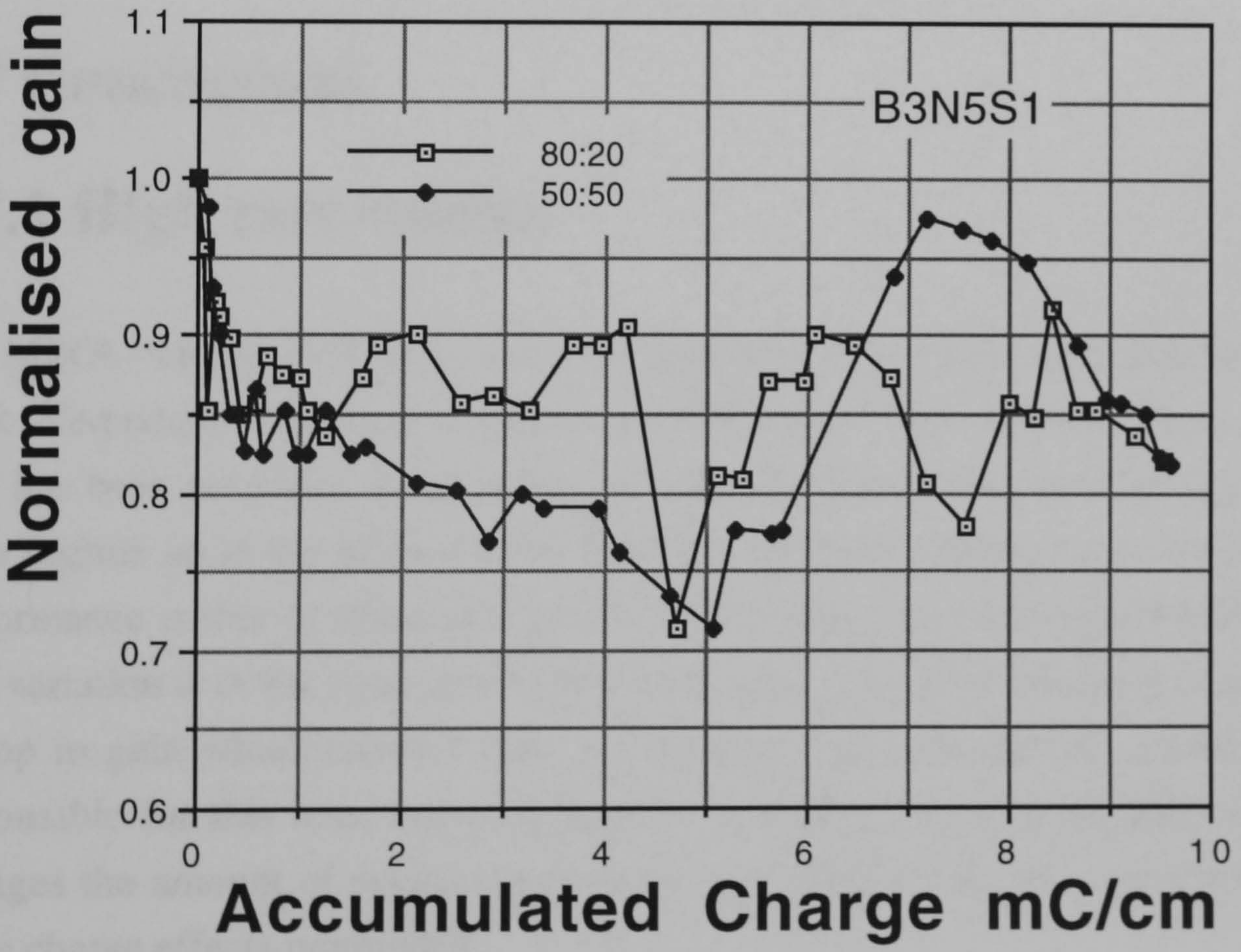

Figure 5.12: Ageing curves for different percentages of DME

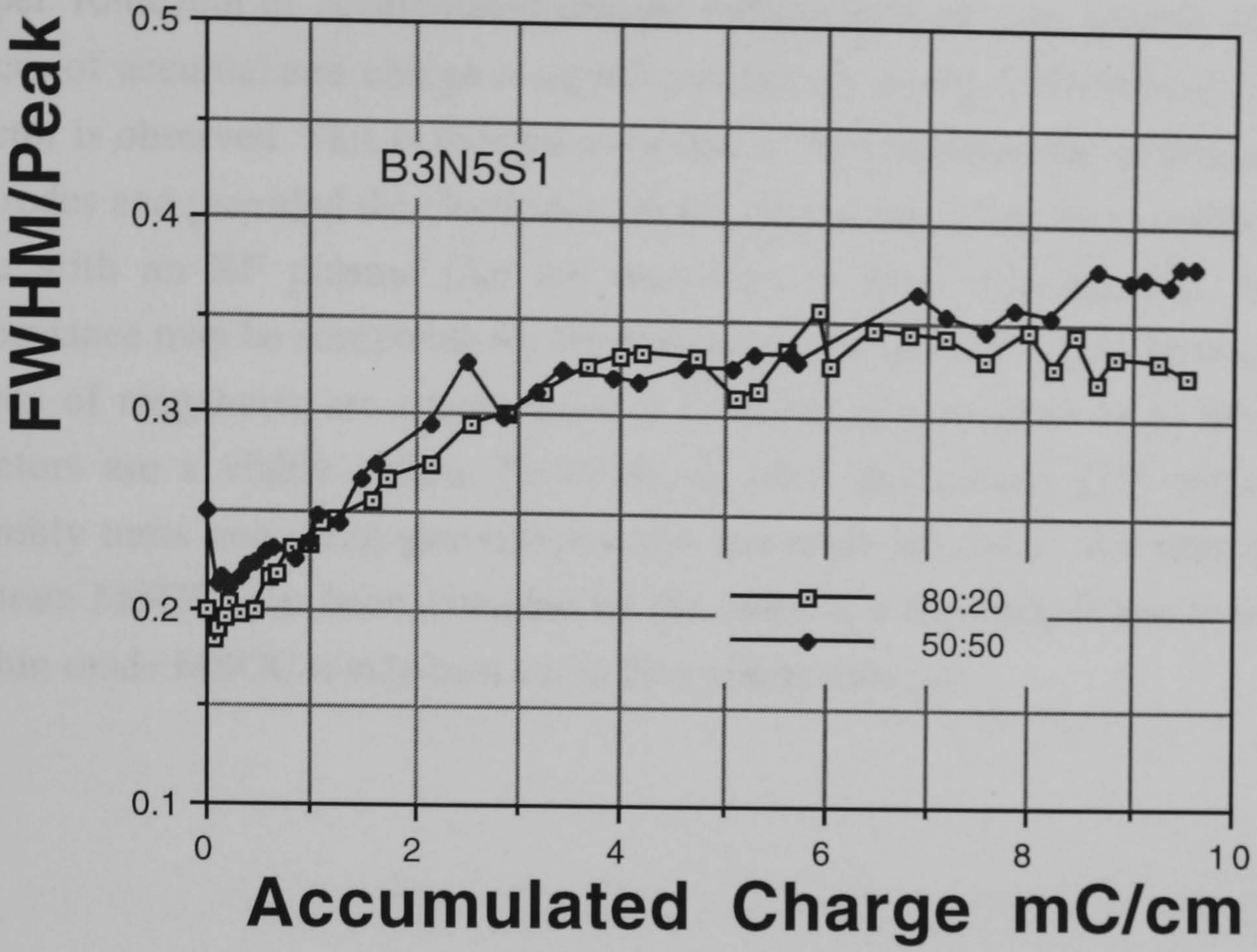

Figure 5.13: Energy resolution versus accumulated charge for ageing tests with different relative percentages of DME

5.7 Conclusions

5.7.1 High rate studies

The MSGC was studied using an x-ray generator of variable flux and has proved to work adequately to rates in excess of 20 MHz/mm^2. The distribution of ion current flow has been measured as a function of rate showing that the detector operates in the same regime up to the highest rates. Perhaps the main limiting factor in the detectors performance is that of space charge. For rates below approximately 4 MHz/mm^2 the gain variation is of the order of 4%. But for higher rates space charge is responsible for a drop in gain which reaches 20% at 24 MHz. The slow moving positive ions are responsible for this loss, implying that by carefully choosing the drift and cathode voltages the amount of positive ions in the gas volume may be controlled and hence space charge effects minimised.

5.7.2 Ageing studies

Several ageing tests have been performed with doses up to ~50mC/cm. There is a reasonable agreement between the different tests which show a fall of approximately

4% per 10mC/cm of accumulated charge, independent of rate. During the first few mC/cm of accumulated charge a significant change in the FWHM/peak ratio of the detector is observed. This is thought to be due to the accumulation of polymers on the electrodes and provided the electrodes are not destroyed, it may be possible to remove these with an RF plasma like the one used in their manufacture. Whilst this performance may be acceptable for HEP purposes, in SR work where rates of the order of tens of megahertz are encountered, it becomes questionable as to whether such detectors are a viable option. However, at other institutions [19] where ceramic assembly units and clean gas systems and materials are used, the lifetime of bulk substrate MSGCs has been extended by the order of a hundred. If this is the case for the thin oxide MSGC it may turn out to be a viable solution.

Bibliography

[1] EG & G ORTEC Instruments, Div. of EG & G Ltd., Sorbus House, Mulberry Business Park, Wokingham, Berkshire, RG11 2GY, UK.

[2] LeCROY Research Systems Ltd., Elms Court, Botley, Oxford, OX2 9LP. UK.

[3] Keithley Instruments Ltd., 1 Boulton Road, Reading, Berkshire, RG2 0NL, UK.

[4] F.Sauli, *Principles of Operation of Multiwire Proportional and Drift Chambers,* CERN 77-09 1977

[5] S.F.Biagi, T.J.V.Bowcock, D.Duxbury, J.N.Jackson, T.J.Jones, S.Kiourkos *A study of the response of thin-oxide MSGCs to minimum ionising particles and low energy x-rays* Nucl. Instr. and Meth. A367 (1995) 193-197

[6] A.Oed, P.Geltenbort, C.Budtz-Jorgensen *Substratum and layout parameters for microstrip anodes in gas detectors* Nucl. Instr. and Meth. A310 (1991) 95-97

[7] I.Duerdoth, S.Snow, R.Thompson, N.Lumb *A study of breakdown in microstrip gas chambers* Nucl. Instr. and Meth. A348 (1994) 356-360

[8] Nanochem gas purification system, Hercules Inc., Wilmington, U.S.A.

[9] R.Bouclier, G.Million, L.Ropelewski, F.Sauli, Yu.N.Pestov, L.I.Shekhtman *Performance of gas microstrip chambers on glass substrata with electronic conductivity* Nucl. Instr. and Meth. A332 (1993) 100-106

[10] SILENA S.p.A., Via Firenze 3, 20063 CERNUSCO S/N, ITALY.

[11] J.A.Kadyk *Wire chamber ageing* Nucl. Instr. and Meth. A300 (1991) 436-479

[12] A.V.Zarubin *Properties of wire chamber gases* Nucl. Instr. and Meth. A283 (1989) 409-422

[13] L.Malter, Phys. Rev., Vol. 50 (1936)

[14] J.Va'Vra *Review of wire chamber ageing* Nucl. Instr. and Meth. A252 (1986) 547-563

[15] R.Bouclier, C.Garabatos, G.Manzin, F.Sauli, L.Shekhtman, T.Temmel, G.Della Mea, G.Maggioni, V.Rigato, I.Logachenko *Development of microstrip gas chambers on substrata with electronic conductivity* CERN-PPE/93-192, October 1993

[16] R.Bouclier, C.Garabatos, G.Manzin, G.Million, F.Sauli, T.Temmel, L.Shekhtman *Ageing studies with micro-strip gas chambers* CERN-PPE/94-63, March 1994

[17] Procedures for high rate MSGC tests, CERN-PPE-DRD, March 1994

[18] S.Majewski *Results on ageing and stability with pure DME and isobutane/methylal mixture in thin high rate multi-wire chambers* LBL workshop

[19] R.Bouclier, M.Capeans, C.Garabatos, G.Manzin, G.Million, L.Ropelewski, F.Sauli, L.Shekhtman, K.Silander, T.Temmel-Ropelewski *Ageing of microstrip gas chambers: problems and solutions* CERN-PPE/96-33, January 1996

Chapter 6

Imaging properties of the MSGC and MGAP

6.1 Introduction

The imaging properties of the MSGC and MGAP detectors will be discussed in this chapter. The detectors had to be interfaced to an existing readout system, which will briefly be described, that enables single channel readout. The initial testing performed with the system will also be given The tests were carried out in the Biological X-ray Detector Laboratory at the Daresbury SRS and on two separate beamlines of the SRS.

6.2 Description of readout system

The readout system used for these tests has been designed for a wire microgap detector built at the Daresbury laboratory, and a description of the system and detector is given in [1]. The Multi Wire Linear (MWL) system is a multi channel acquisition system, which enables multiple events to be handled simultaneously thus increasing the overall counting rate performance, whilst any single channel has only to operate at modest speeds. The ultimate in this approach is the pixel detector, which consists of an electronics chain for each pixel including amplifier, discriminator, counting and memory. A schematic diagram of the MWL system is shown in figure 6.1. With this system no attempt is made to perform any interpolation between channels thus one anode represents one pixel. The amplifiers (A) have been realised as surface mount printed circuits and are enclosed within the detector housing. Each hybrid consists of 4 channels of bi-polar amplifiers and a 4 channel digital to analogue converter to enable each discriminator threshold to be adjusted independently by software control. The individual gain of each amplifier can also be adjusted using the same software. The system is designed such that the sum of two adjacent wires can be readout. This is used

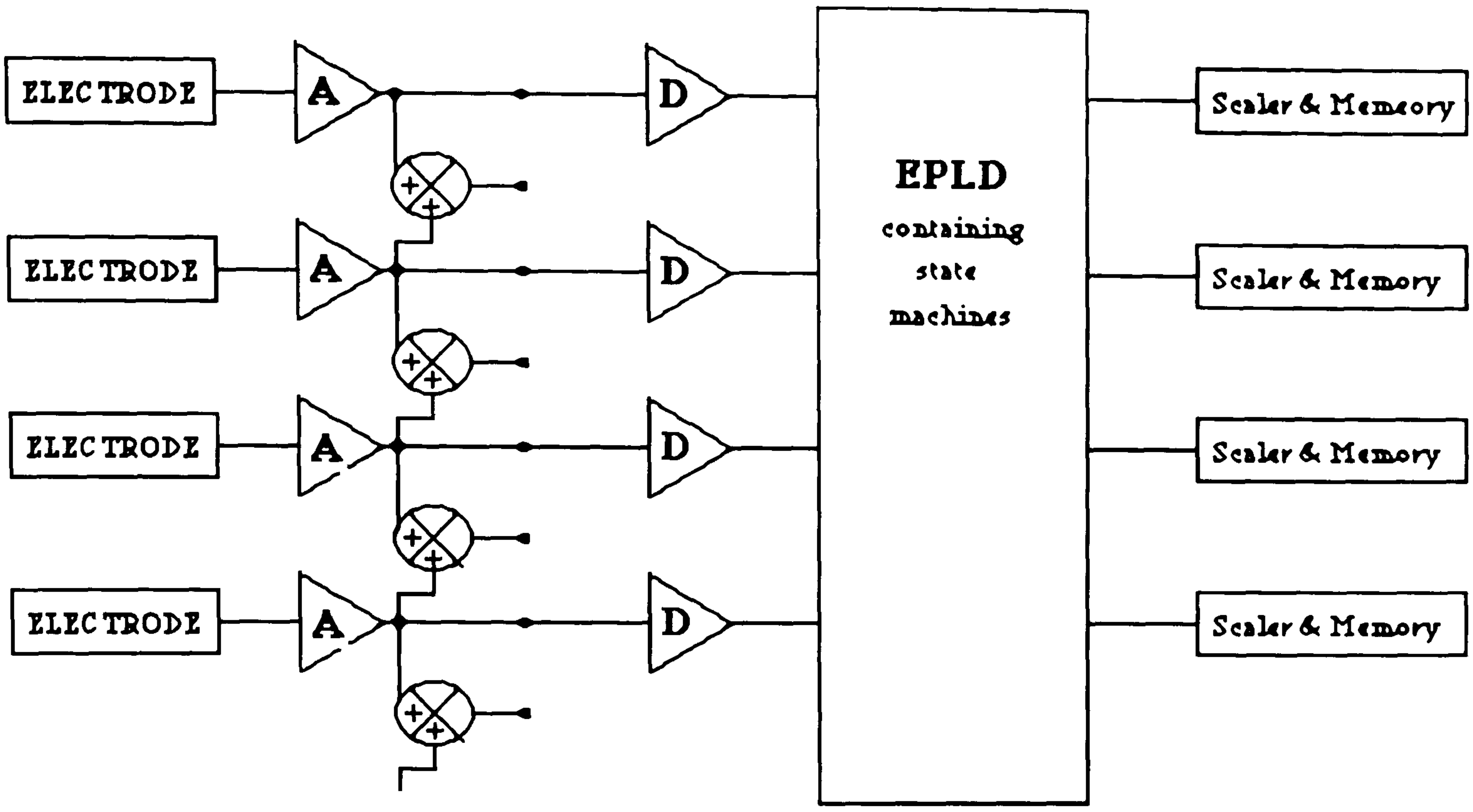

Figure 6.1: Schematic representation of MWL readout system

to overcome the effects of charge sharing, which is when the full signal from a photon interaction is shared between two adjacent wires resulting in two smaller signals being obtained. In this "sum channels" mode, as in single channel mode, double counting can occur and this is overcome by the inclusion of very fast state machines which examine the pattern of pulses above the threshold level of the discriminators. These are programmed such that to define a hit either 1,2 or 3 adjacent channels out of 5 must be firing. These state machines also operate when the system is used in single channel mode and it is this mode that is used in the presented results.

6.3 Characterisation of the MGAP detector

The microgap detector used in these tests has kindly been supplied by R.Bellazzini of the INFN Pisa, and was already instrumented for single anode readout i.e. each anode was connected to a preamp channel. Hence interfacing the MGAP with the MWL readout was simply a case of linking the two with a twisted pair cable. Unfortunately the signals coming from the preamps were far too small, resulting in the need for extra post amplifiers. The MSGC tested had to have a special PCB and housing designed to directly couple it to the preamp housing of the MWL and this will be described in the next section.

The MGAP detector is adequately described in [2,3] and will only briefly be characterised here. The gain of the MGAP detector is much higher than that of the MSGC for the same voltage due to the higher electric field defined by its structure. In figure 6.2 the gain for a single anode is plotted versus the applied cathode voltage.

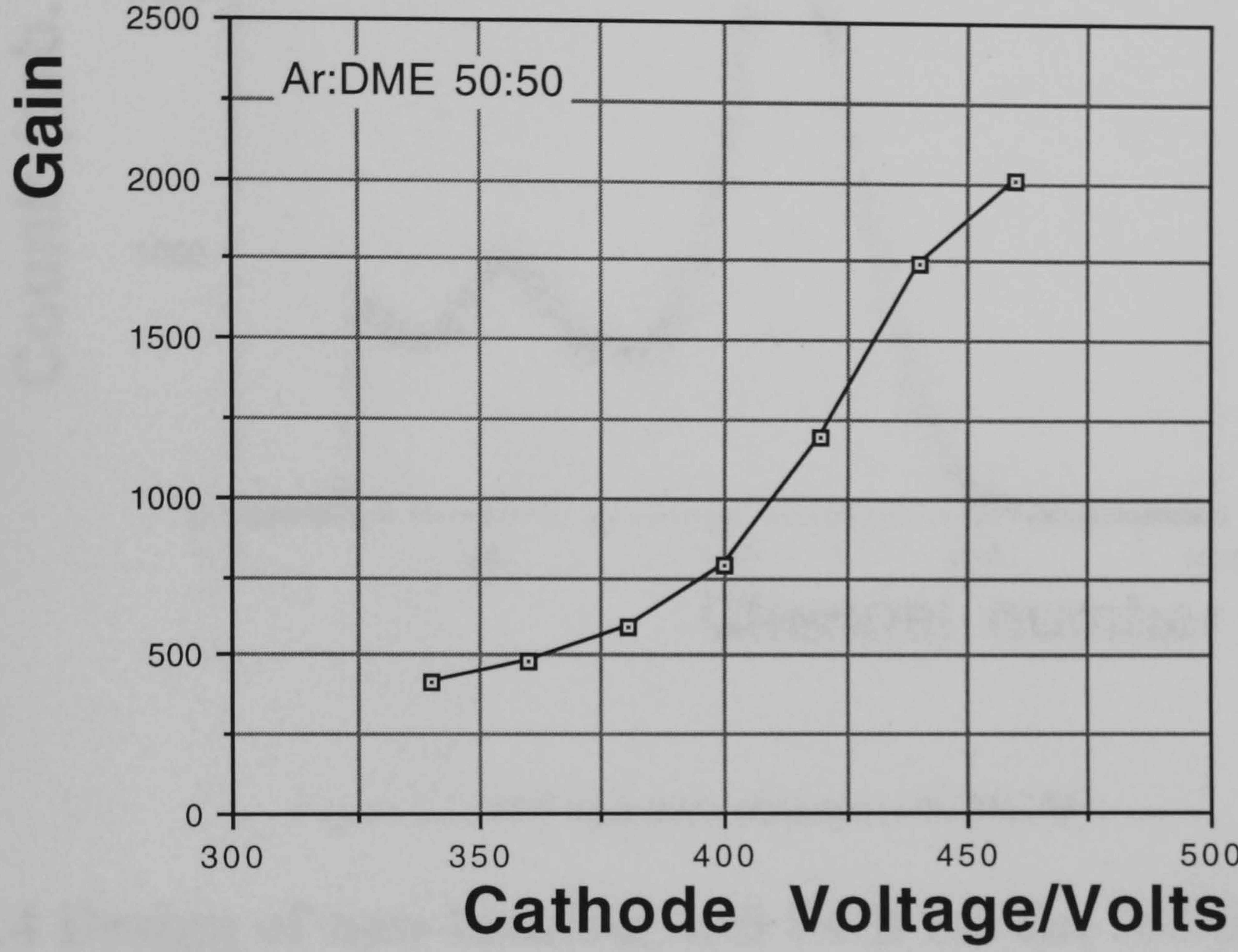

Figure 6.2: MGAP gain for a single anode

One would expect the values given in the graph to be further increased if more anodes were ganged together as more of the charge created in the avalanche will be collected. It is worth noting that the gas mixture used in the detector has a high percentage of quench gas. This is necessary due to the close proximity of the cathode to the anode which calls for a corresponding reduction of the UV photons mean free path created in the avalanche. Failure to use a large amount of quench gas results in catastrophic sparking at the electrode surface. In fact this was the reason for not increasing the gain above 2000. The energy resolution of the MGAP has been measured to be 14.8% for 5.4 keV Chromium x-rays [2], but for the system used the energy resolution is of the order of 25%, figure 6.3. This figure was obtained from the sum of 4 adjacent channels and with an uncollimated x-ray source, so one would expect a better energy resolution if the number of anodes summed into the preamplifier was increased.

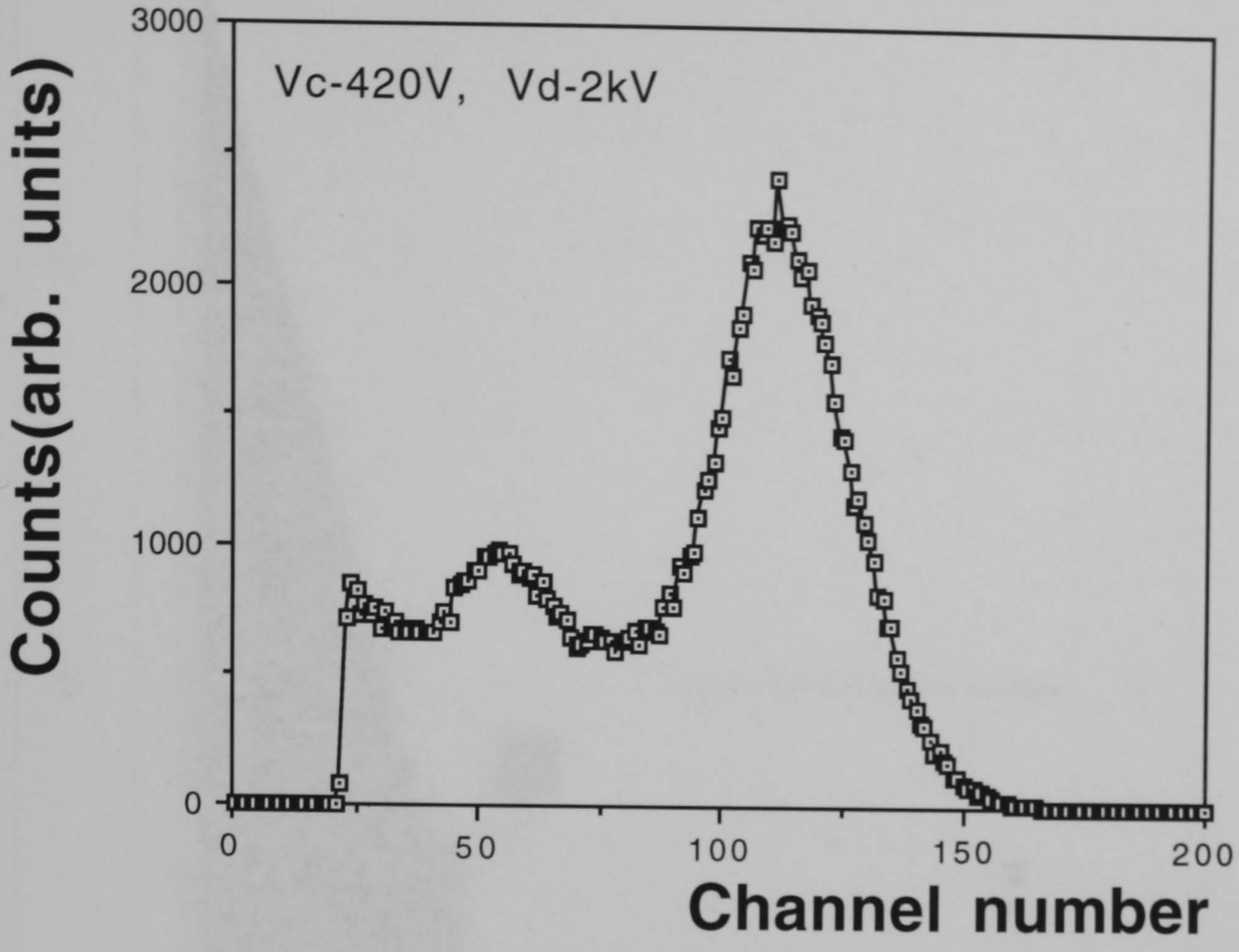

Figure 6.3: Fe^{55} spectrum obtained with MGAP

6.4 Design of new housing and PCB for the MSGC

Before an MSGC could be tested with the readout system a new PCB was designed enabling each electrode to be independently read out. To be easily interfaced with the MWL electronics a new housing also had to be made which could be bolted straight onto the preamp housing therefore making read out straightforward. The PCB design is shown in figure 6.4 and a drawing of the housing is given in figure 6.5. In figure 6.4 only the top side of the PCB is shown, the rear side contains biasing resistors and decoupling capacitors. The 200 tracks shown coming from the wafer have a width of $100\,\mu m$ with the same width gap between tracks. This extends further to a pitch of 1.6mm where they are soldered to 'Samtec' [4] micro strip terminals enabling connection to the female 'Samtec' connector of the preamps. The tracks are made of copper with a coating of nickel and a further coating of gold flash. The gold coating is necessary so that the anodes of the wafer can be ultrasonically bonded to them. The nickel is present to strengthen the gold during the bonding. The housing, made in-house at Liverpool, is made of aluminium and is fitted with a rubber o-ring to provide a gas tight seal along with provisions for HV connectors and gas inlets. The detector was then assembled and bonded at Liverpool and taken to Daresbury for testing.

Figure 6.4: New PCB design for MSGC

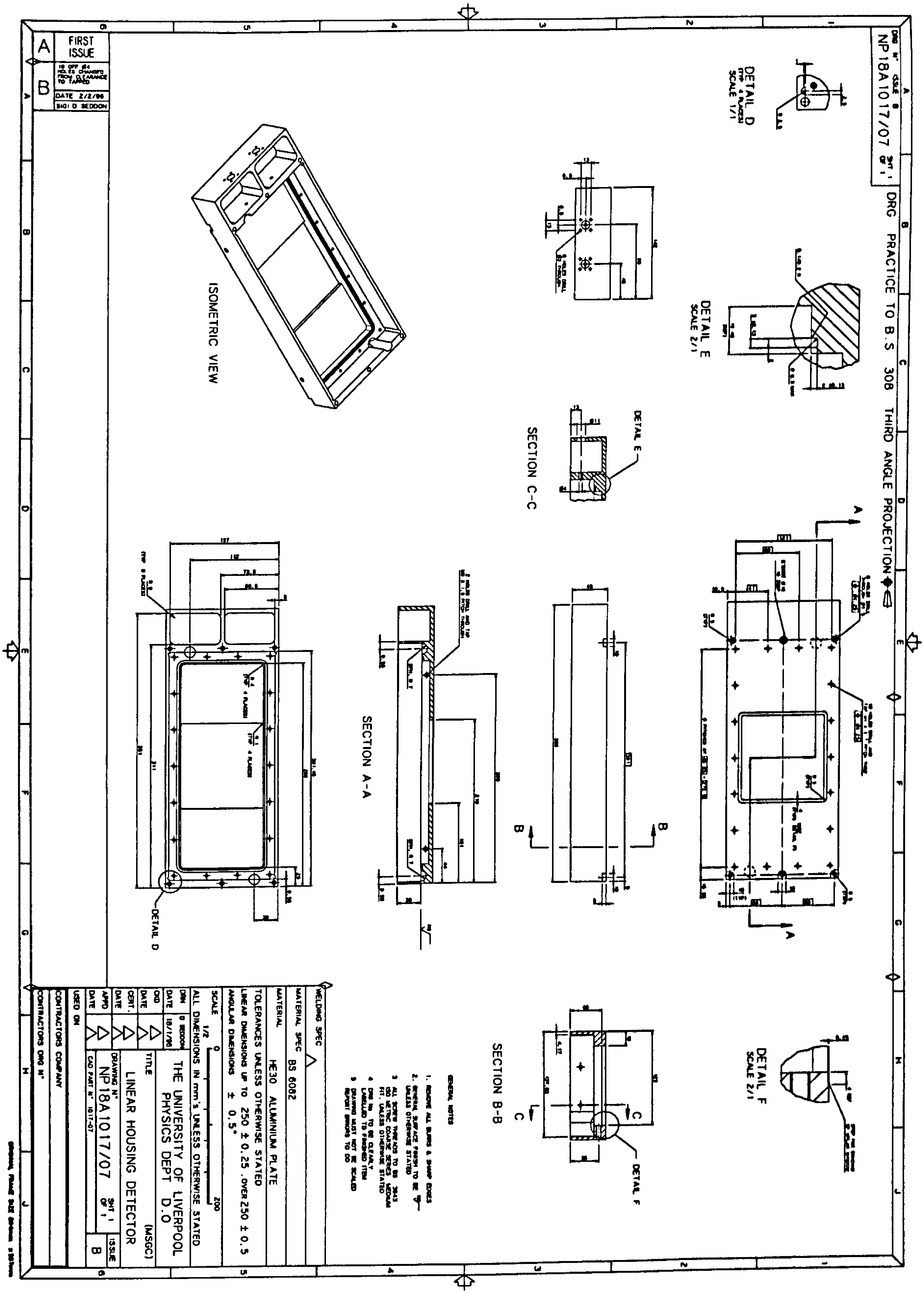

Figure 6.5: Engineering drawings for MSGC housing

6.5 Initial laboratory tests with the MWL readout system

As mentioned in section 6.2, the individual gains of the preamplifiers and the threshold levels of the discriminators are set by the use of PC based software. Figure 6.6 shows a gain scan taken with the MSGC. This was performed with the detector switched off and with no x-ray illumination and at a fixed threshold level on the discriminators. The gain of the preamps can be varied between 0 and 2047. The figure shows the levels at which the preamps become noisy. This figure is not the actual gain of the preamplifier but just the value passed to the DAC and represents some fraction of the actual gain. With the exception of a few channels the noise levels of the preamps are very similar. Channel 60 however, is clearly not performing as the others. This is precisely the reason for doing the scan, so that the gains can all be set to levels at which they give the same count rate. For the results given, the gains were set at the levels where they gave 50 noise counts per second.

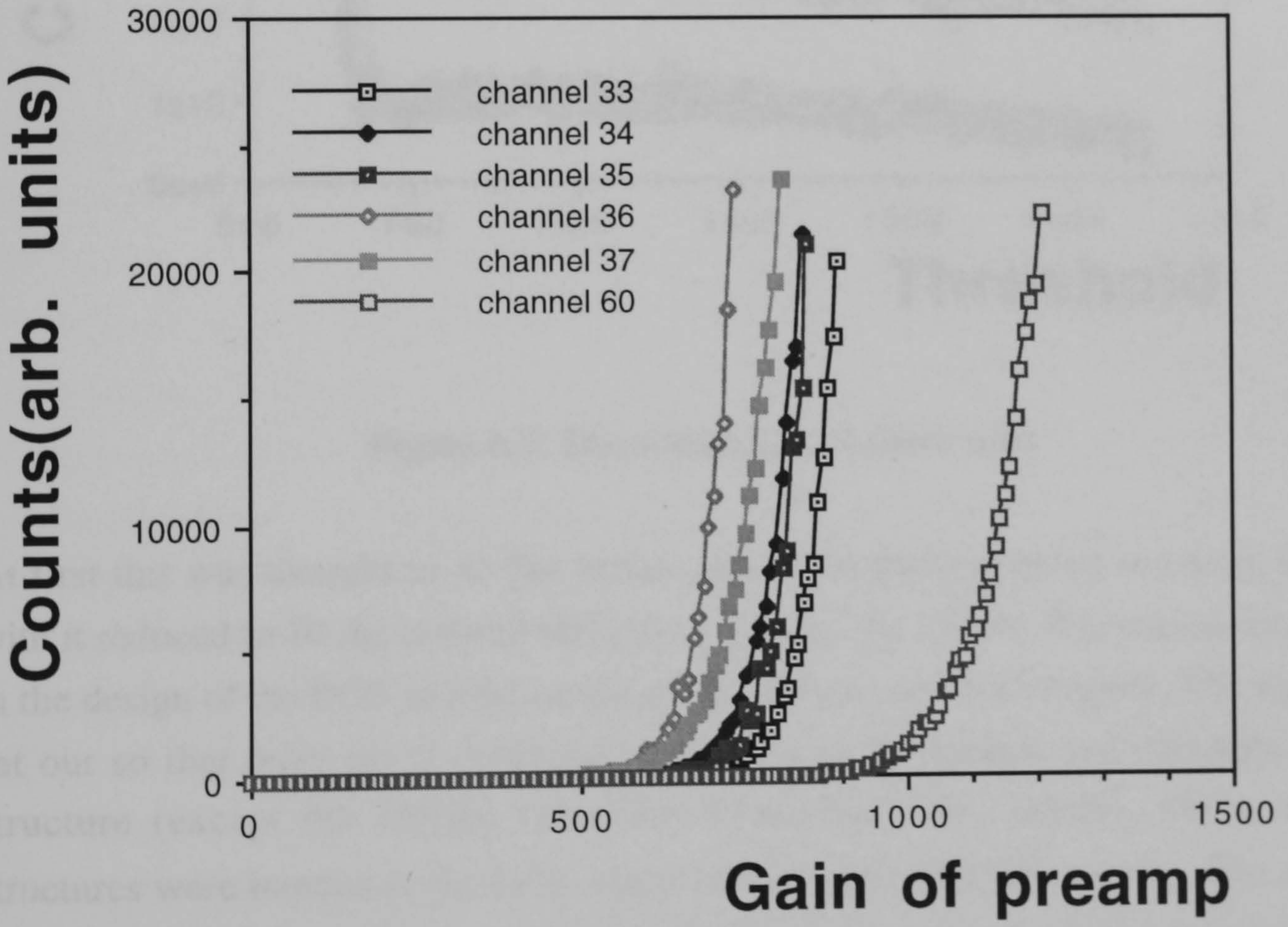

Figure 6.6: Preamplifier gain scan

The discriminator thresholds can be varied from 0 to 2000 where 0 corresponds to -0.25V and 2000 to 0.75V. Figure 6.7 shows a threshold scan taken with the MSGC and with the gain levels of the preamps determined from the scans shown in figure 6.6, under illumination and with the detector operational. The threshold was varied from 500 to 1600 corresponding to levels of 0V and 0.6V. The graph shows the noise at low values of threshold and then as the threshold is gradually increased, a flat response as would be expected from a detector with good proportionality. As can be seen from the figure channel 60 records approximately 3 times the counts as the rest of the channels.

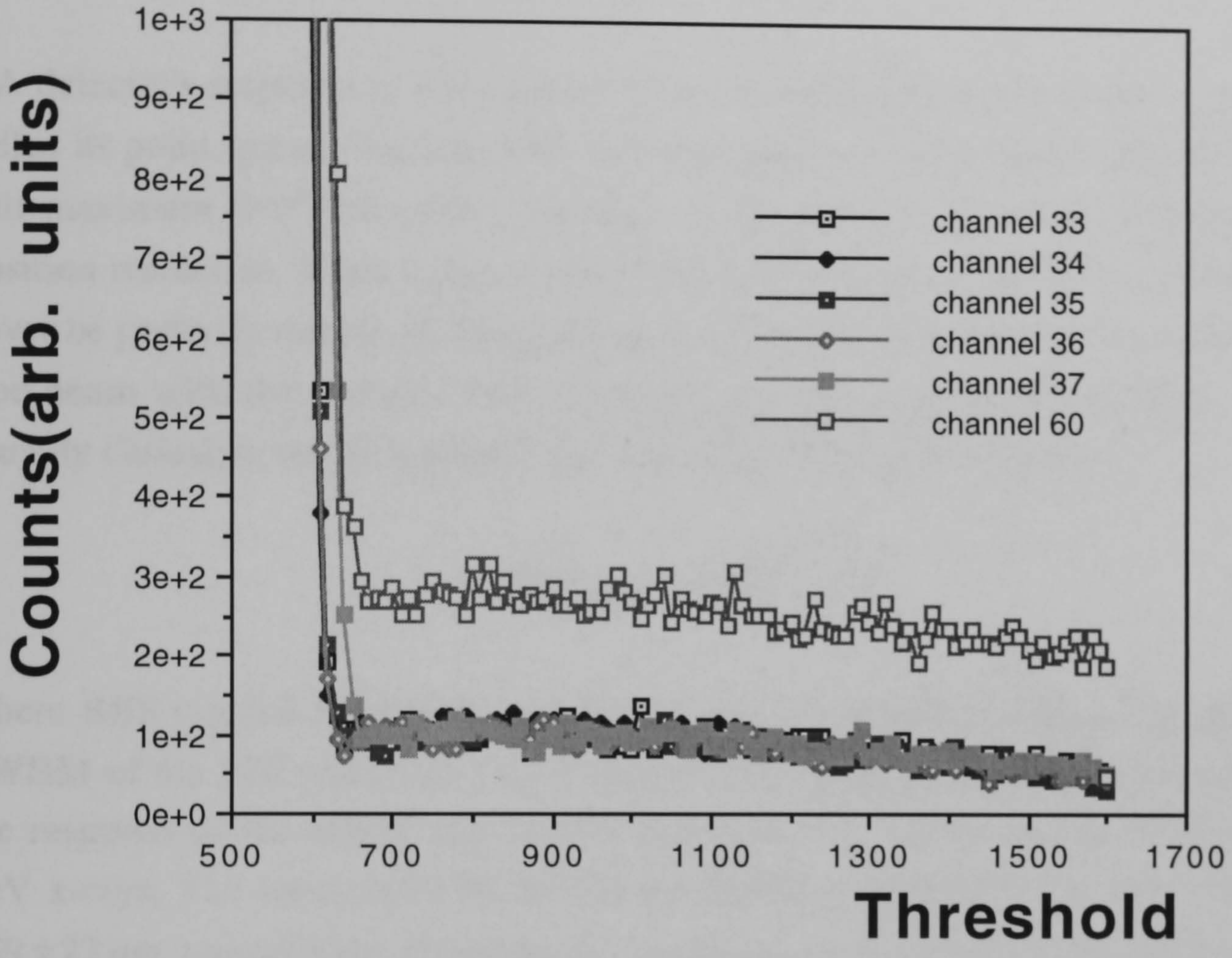

Figure 6.7: Discriminator threshold scan

At first this was thought to be due to the gain of the preamp being too high, but even with it reduced to 10 the channel still gave ~3 times the counts. The reason for this lies in the design of the PCB and the layout of the wafers used at Liverpool. The wafers are set out so that there are 5 structures on each with 60 anodes and cathodes to each structure (except the $100\mu m$ structure which has 120 anodes). Three of these structures were bonded to the PCB which had provision for 200 anodes. The structure used in the tests was structure 2 but structures 1 and 4 were also bonded. Hence to one side of structure 2 the anodes were grounded but on the other side they were at floating potential. Thus the extra counts seen on channel 60 were due to x-ray interactions outside of the drift region above structure 2 being focused onto the anodes whereas at the edge near structure 1, interactions outside the drift region are neutralised on the grounded anodes of structure 1. Thus throughout the tests the threshold level was set above the noise at approximately 700. For the results presented in the following sections the MSGC was operated at -350V on the cathodes and -2kV on the drift in an Ar:DME 75:25 gas mixture and the MGAP at -440V on the cathodes with -2kV on the drift in an Ar:DME 50:50 gas mixture. These settings correspond to gas gains of approximately 300 and 2000 respectively.

6.5.1 Position resolution

A detector's response to illumination from an infinitely narrow beam of photons is called its point spread function, PSF, and will possess a finite width. The full width at half maximum (FWHM) of this function is one way of characterising the detectors position resolution. Since a photon beam has a finite width, the PSF of a detector can never be perfectly measured. The position resolution is given by the convolution of the true beam with the detector PSF. Provided that the beam profile and the PSF are roughly Guassian, which is usually the case, this can be approximated to:

$$FWHM_{mes} \approx \sqrt{RES^2 + \Delta^2} \tag{6.1}$$

where RES (spatial resolution of detector) and Δ (width of photon beam) are the FWHM of the PSF and beam profile respectively. Figure 6.8 shows a comparison of the response of the MSGC and MGAP detectors to a $100\,\mu m$ collimated beam of 8 keV x-rays. The measured FWHM for the MSGC and MGAP are $386 \pm 40\,\mu m$ and $259 \pm 27\,\mu m$ respectively. However the conditions of illumination are not the same in the two cases. In the case of the MSGC the collimator is 30cm from the detector front window and for the MGAP the collimator is 1cm away. The collimator itself consists of a length of brass with attachments at both ends allowing for the insertion of pinhole collimators. The two collimators are 15cm apart. From such geometry it is possible to calculate the FWHM of the beam profile at the detection plane and hence using equation 6.1 calculate the position resolution of the detectors. For the MSGC the FWHM of the beam profile is calculated from the geometry to be $300 \pm 20\,\mu m$ and for the MGAP it is calculated to be $107 \pm 10\,\mu m$. This leads to position resolutions of $243 \pm 25\,\mu m$ and $236 \pm 24\,\mu m$ respectively for the MSGC and the MGAP. For the readout system used, a position resolution of $200\,\mu m$ is the best that one can hope to achieve as the system performs no interpolation between strips. Theoretically then, we would expect to measure FWHM of $360 \pm 40\,\mu m$ for the MSGC and $227 \pm 30\,\mu m$ for the MGAP, which are in fair agreement with the actual measurements.

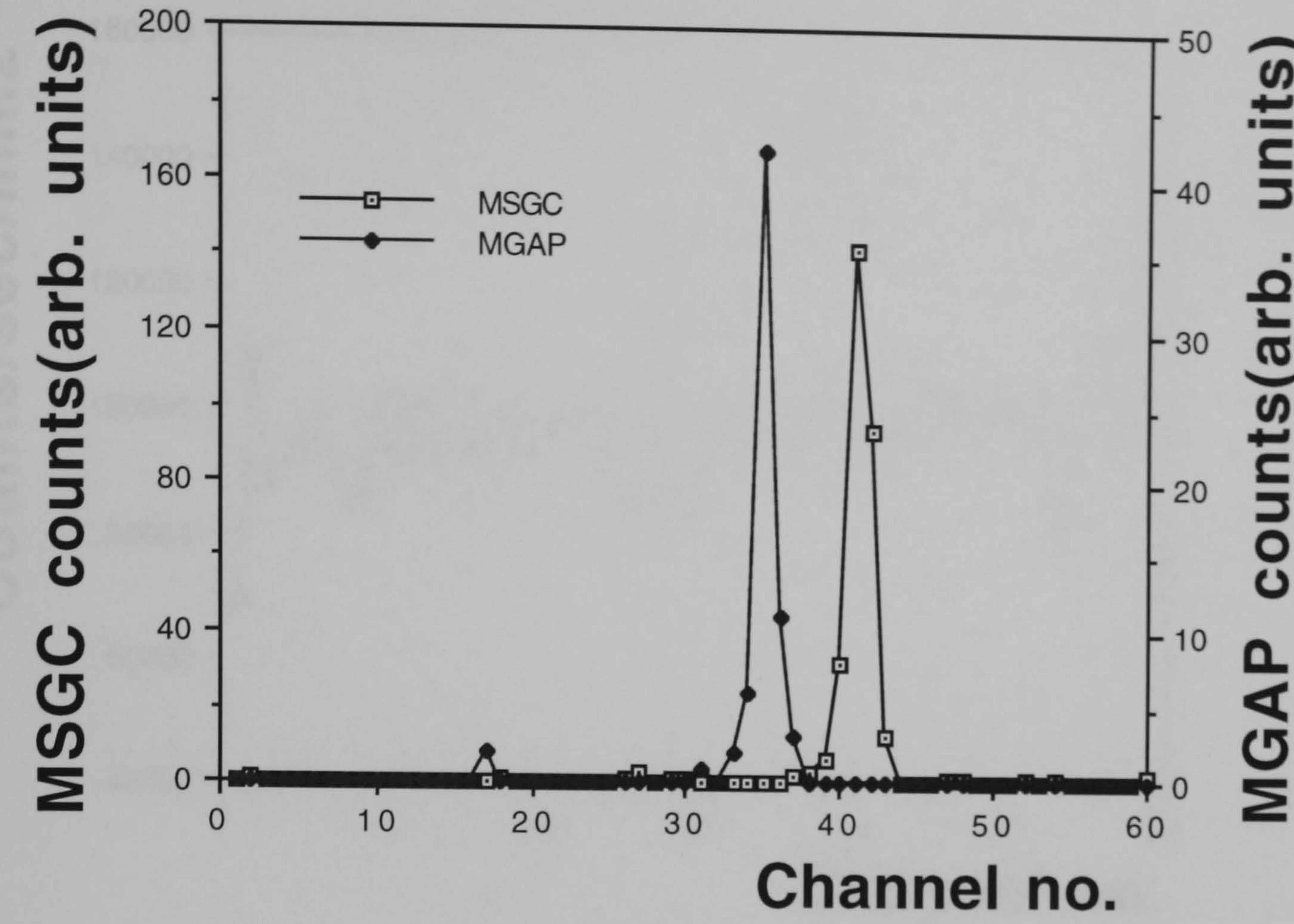

Figure 6.8: Comparison of PSFs of MSGC and MGAP detectors

6.5.2 Detector response studies

For the detectors tested to be considered as viable candidates as imaging devices, a uniform response to illumination is desirable across the whole detector area. Figures 6.9 and 6.10 show the response of the MSGC and MGAP respectively to an uncollimated 8keV x-ray source. The global flux in both cases is of the order of 6MHz. From figure 6.9 it can be seen that the MSGCs response is roughly uniform to 1×10^5 counts per second per square mm. With the obvious exceptions of the detector edges and a few channels centred about channel 28. Figure 6.10 shows a rather more erratic response which is due to non-optimised electronics and the effects of a few dead channels. If we now look at the response at a lower overall input rate of 2×10^4 counts per second per square mm, and divide the image obtained at high flux by that obtained at low flux we should remove any local differences between channels and get a flat response, figure 6.11. Again it can be seen that for the majority of the detector the response is uniform. The inconsistency around channel 26 is not fully understood.

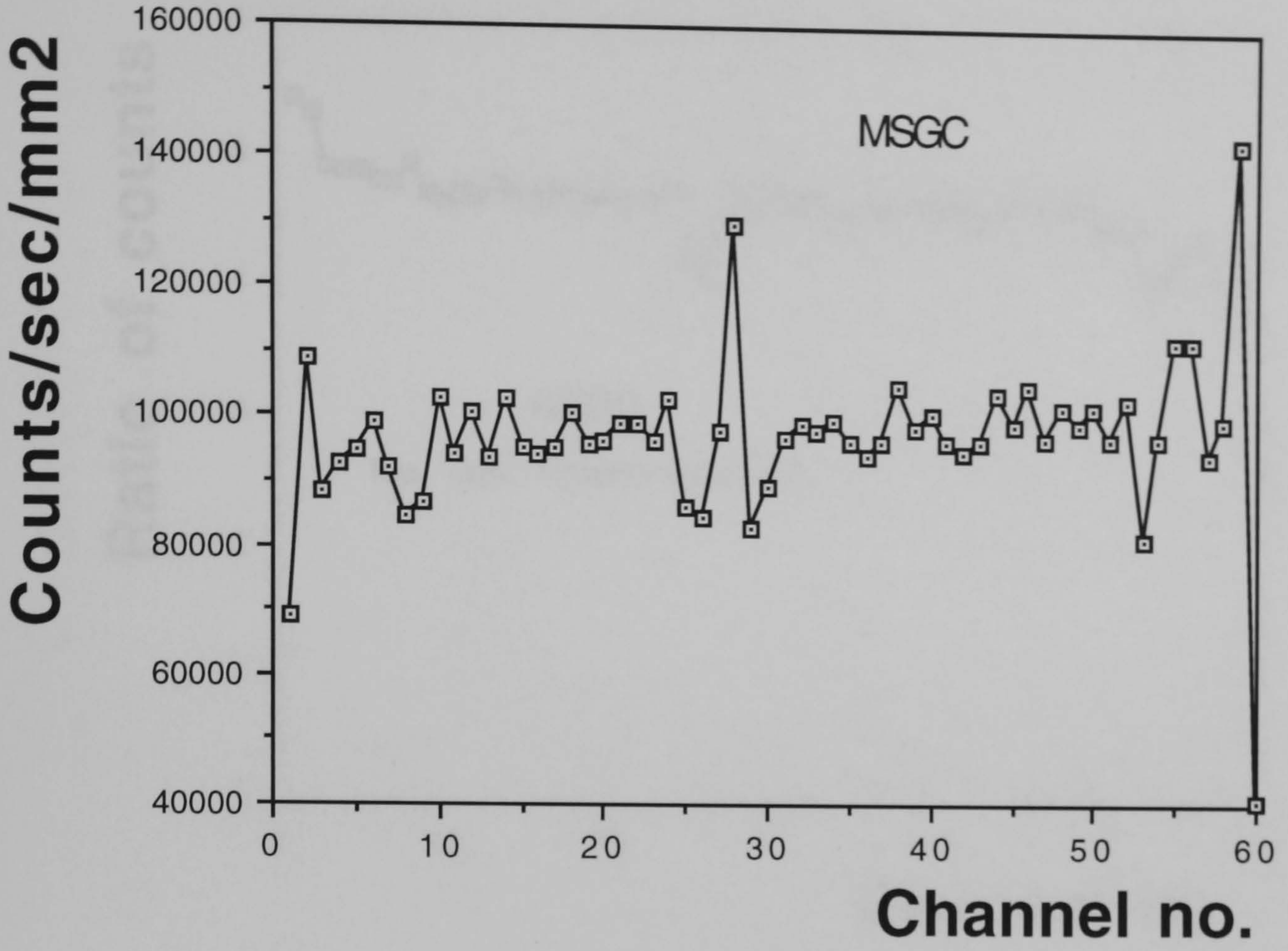

Figure 6.9: Uniformity of response of MSGC to a global x-ray rate of 6MHz

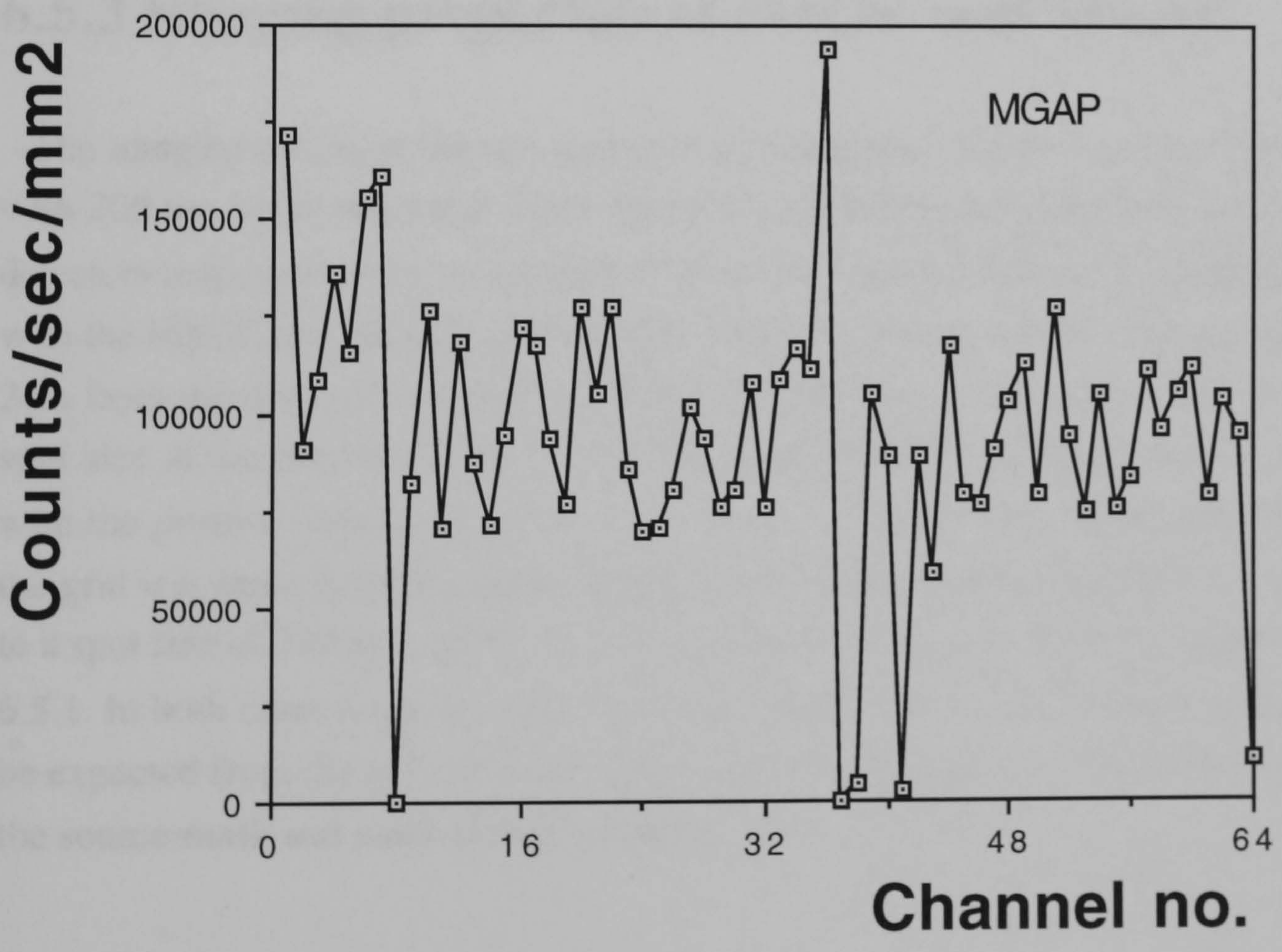

Figure 6.10: Uniformity of response of MGAP to high rate illumination

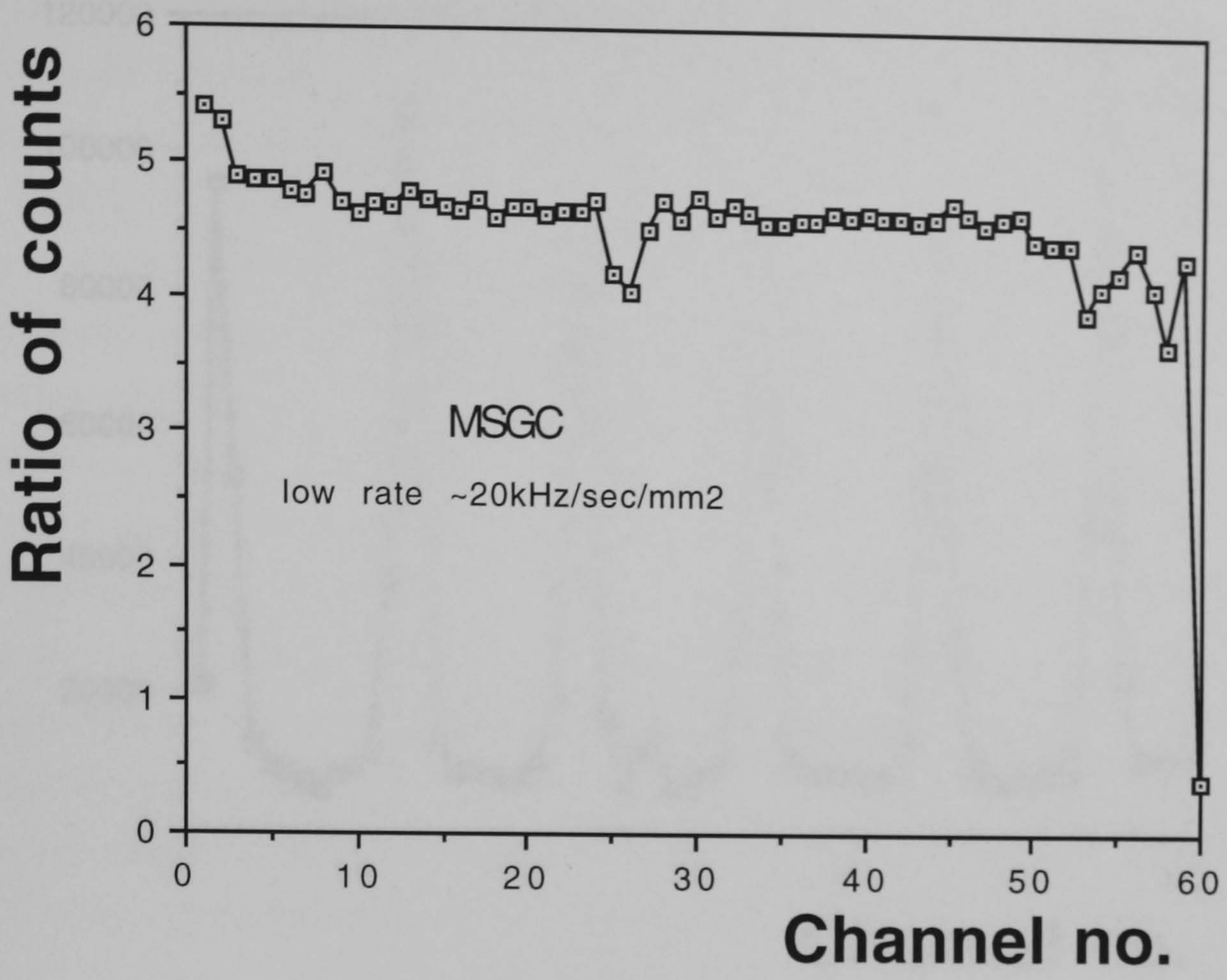

Figure 6.11: Ratio of high rate response to low rate response for the MSGC

6.5.3 Imaging properties of MSGC and MGAP

The imaging ability of the two detectors is investigated in this section. A nickel mask with 200 μm holes spaced at 2mm intervals is illuminated with 8keV x-rays and the detectors response to this is recorded. Figures 6.12 and 6.13 show the obtained patterns with the MSGC and MGAP respectively. In the case of the MSGC, the grid was placed 2cm from the drift cathode and the grid was 43cm from the x-ray source, leading to a spot size at the detector plane of $210\,\mu m$, and the widths of the peaks are consistent with the position resolution given in section 6.5.1. In the case of the MGAP detector the grid was 6mm from the drift cathode and the grid was 6cm from the source leading to a spot size of $220\,\mu m$. Again the peak widths are consistent with the result of section 6.5.1. In both cases it can be noticed that the peaks are not 10 channels apart as would be expected from the grid spacing. This is due to the geometrical relationship between the source-mask and mask-detector separation.

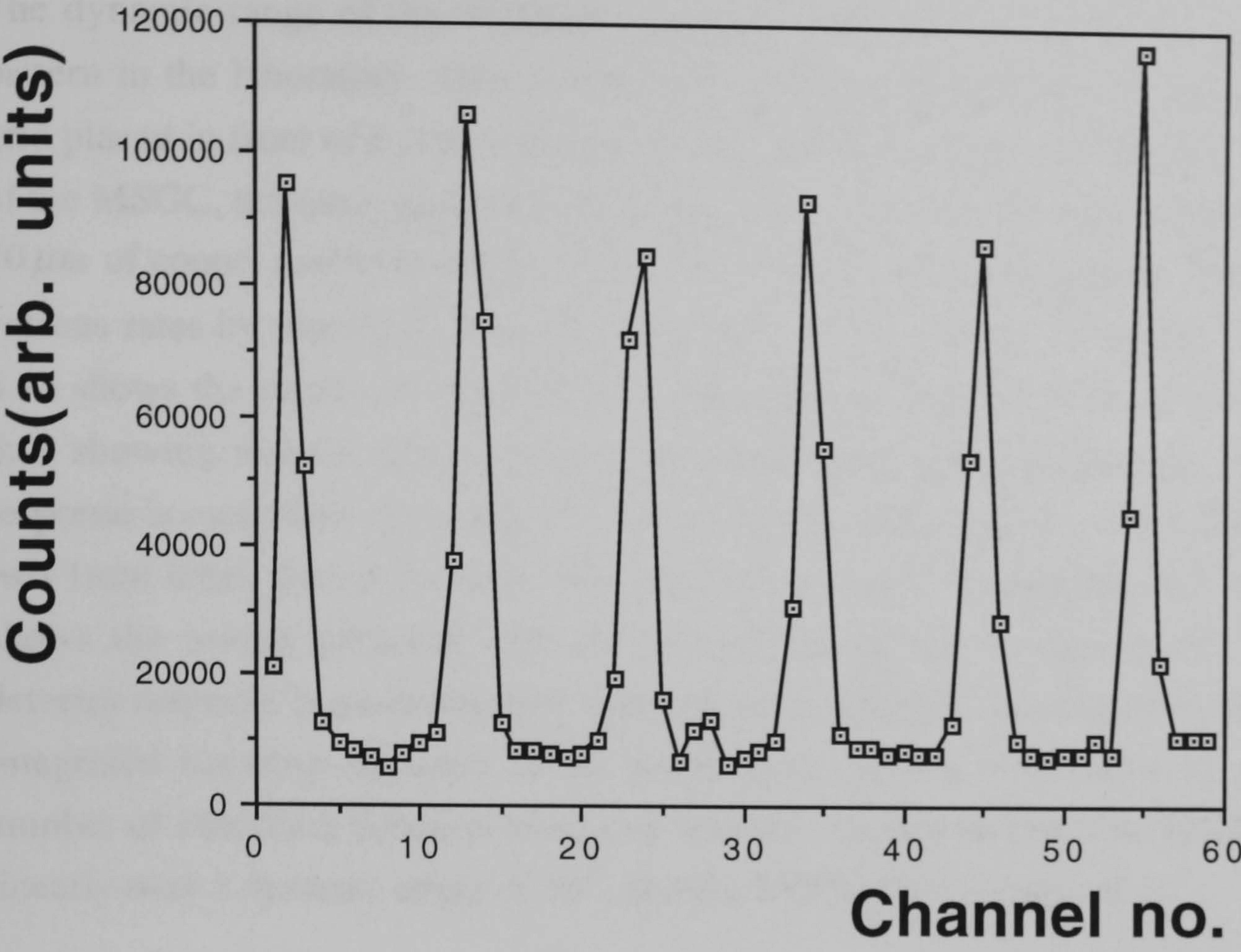

Figure 6.12: Image of nickel grid taken with MSGC

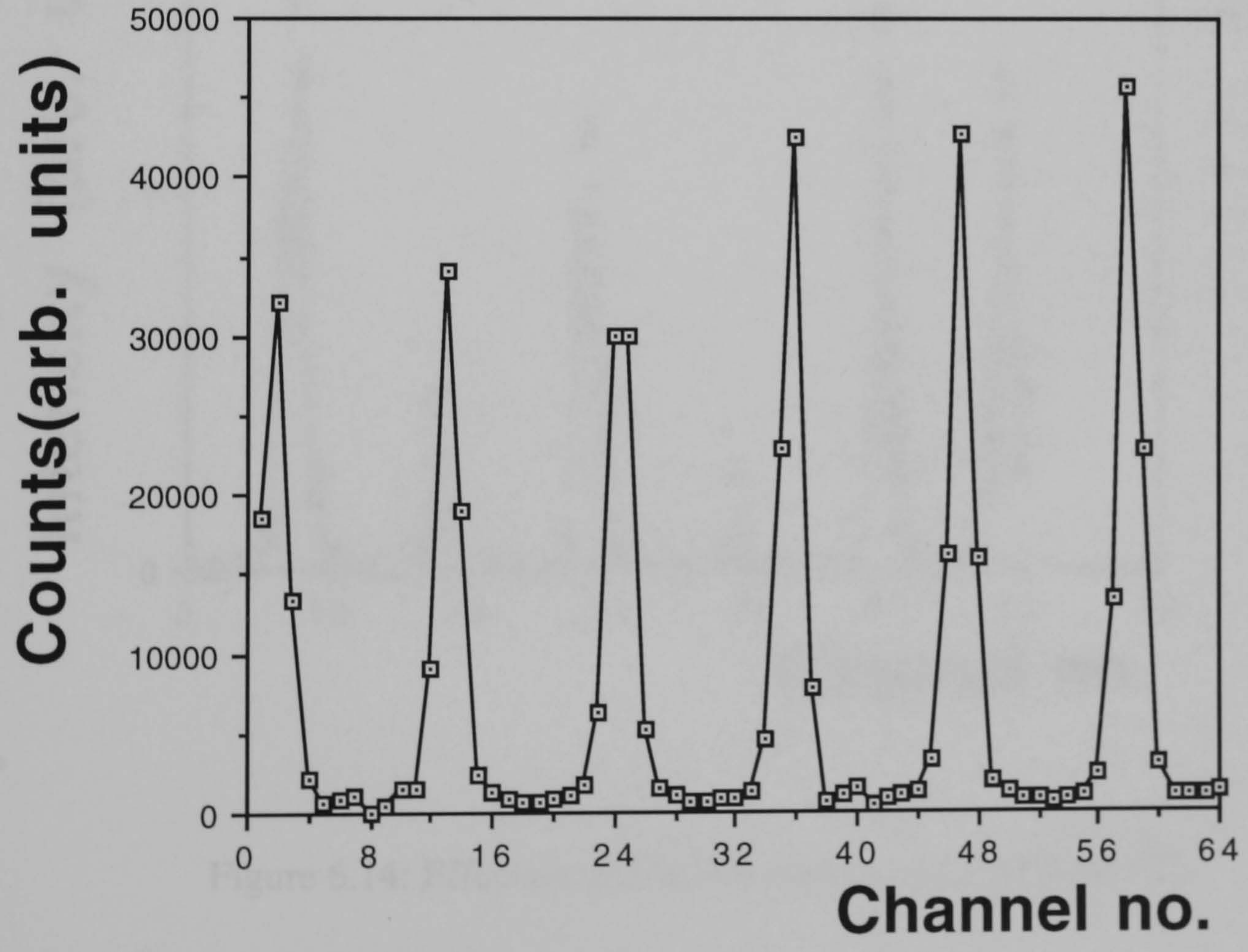

Figure 6.13: Image of nickel grid taken with MGAP

The dynamic range of the detectors can be investigated by simulating a diffraction pattern in the laboratory. This is achieved by again illuminating the detector with a grid placed in front of it, but with absorbers placed over some of the holes. In the case of the MSGC, the same grid was used as in figure 6.12, but with one hole covered with $70\,\mu m$ of copper and with another hole covered with $140\,\mu m$ of copper. This is done at various rates by placing further absorbers between the beam and the detector. Figure 6.14 shows the results of this effective diffraction pattern, normalised to channel 29, thus showing that for each absorber placed between grid and detector, the detector response is essentially the same. For the MGAP the grid used was a sheet of lead with two 1mm holes spaced at 2mm, thus allowing a higher throughput rate. Figure 6.15 shows the results obtained with the MGAP normalised to channel 47. Again the detector response is essentially the same for each different rate. Figure 6.16 shows the integrated intensity for each of the peaks from figures 6.14 and 6.15 against the number of absorbers between beam and detector. As can be seen, the MGAP behaves linearly over a dynamic range of 10^4, and the MSGC over a range of 10^3.

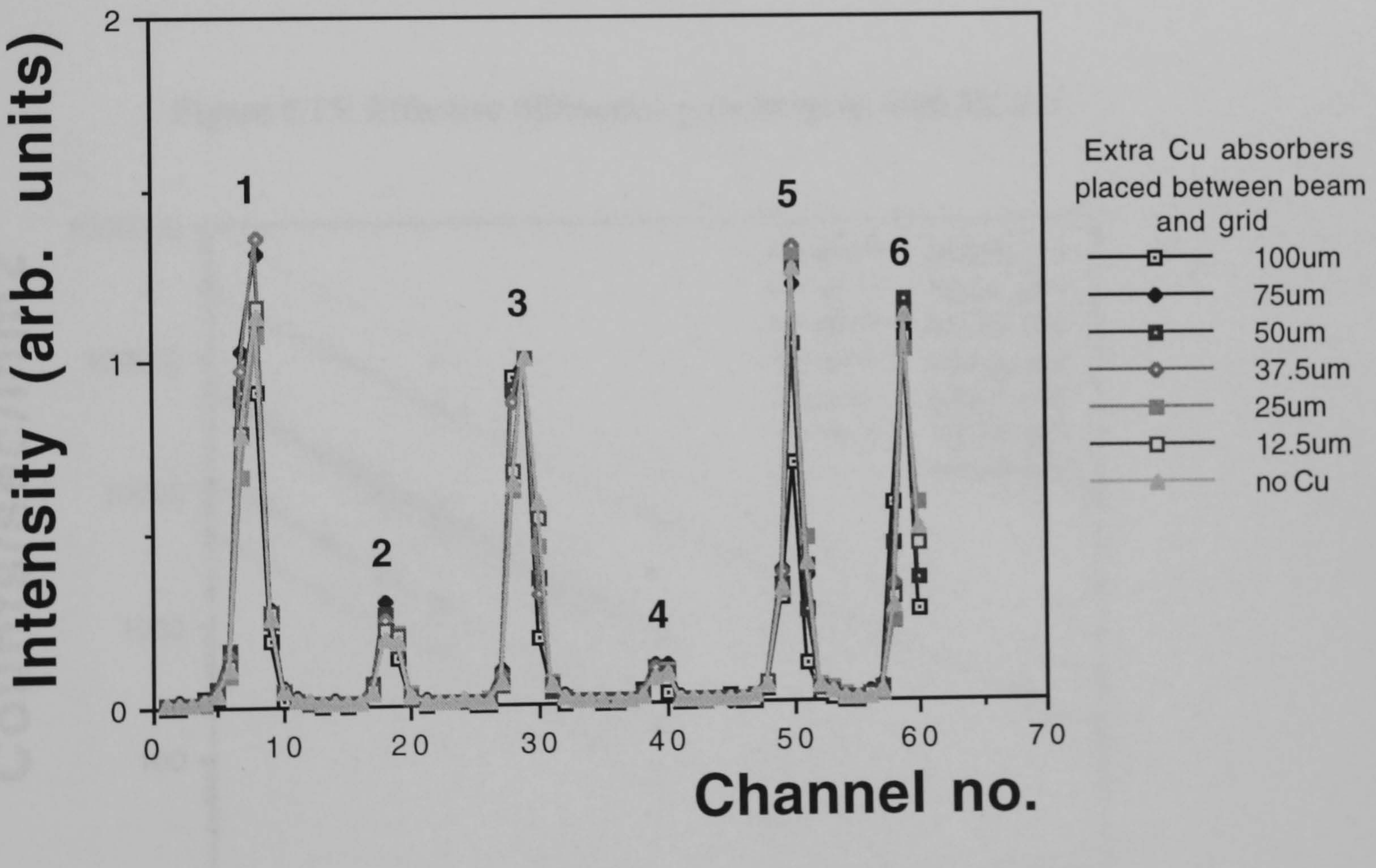

Figure 6.14: Effective diffraction pattern taken with MSGC

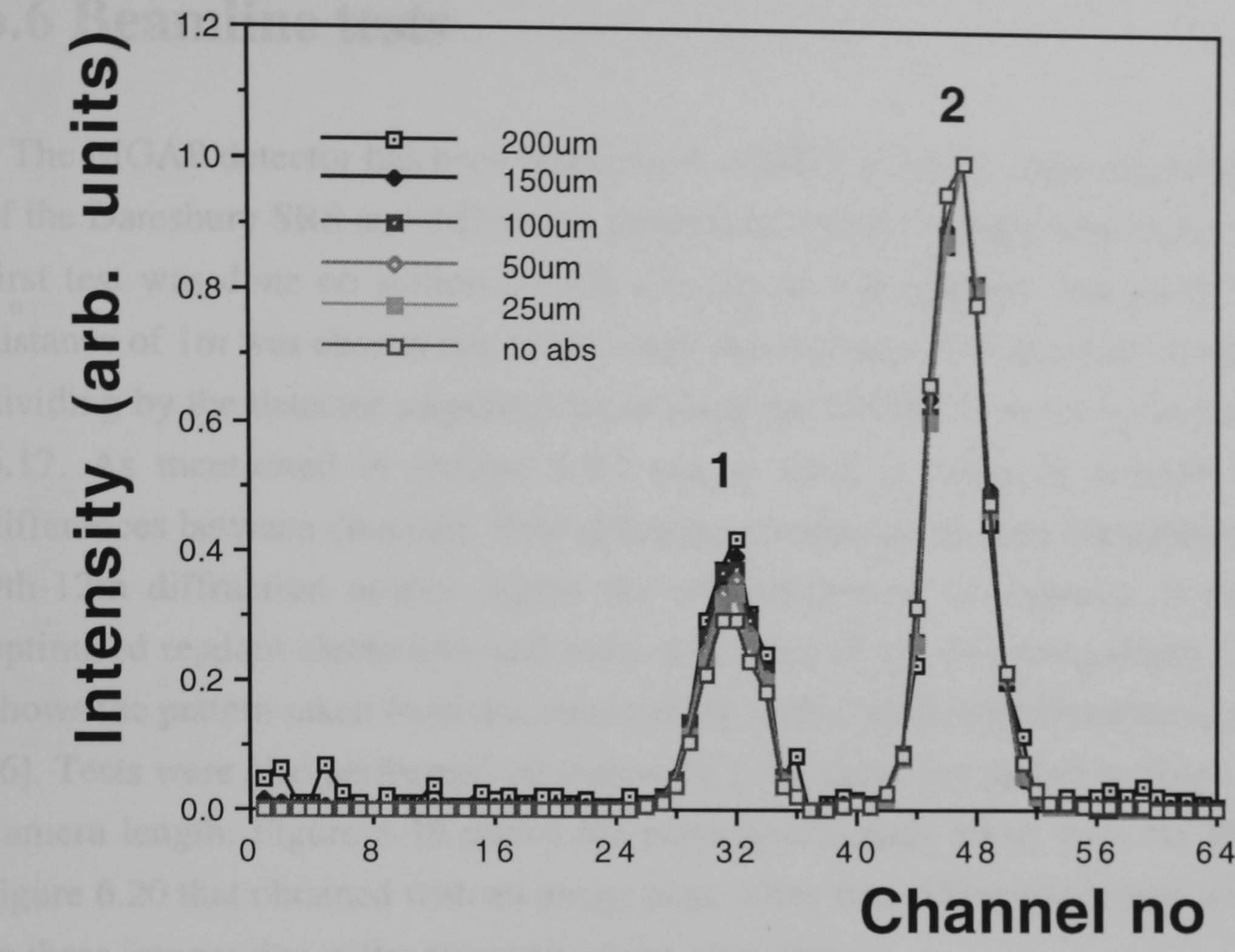

Figure 6.15: Effective diffraction pattern taken with MGAP

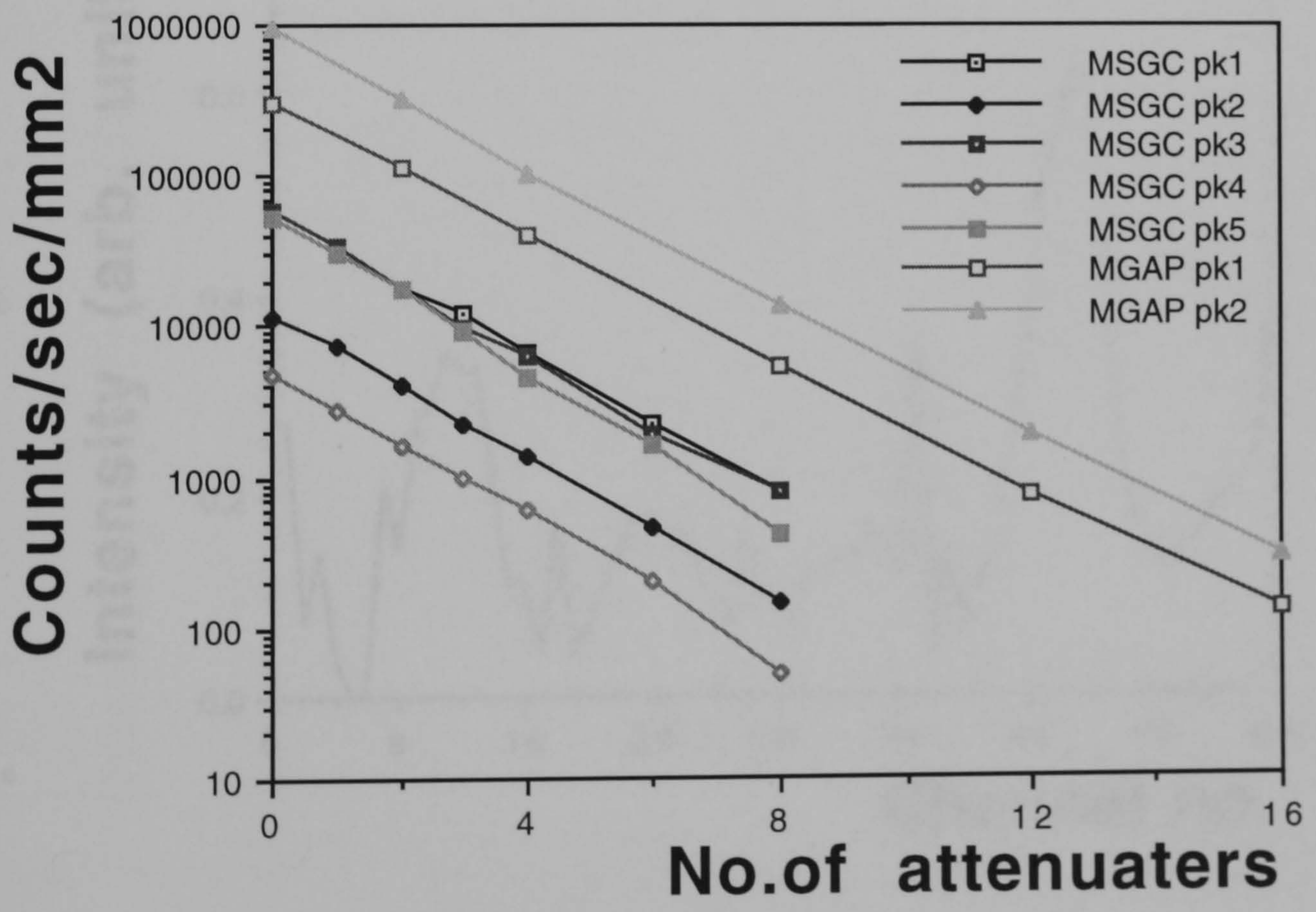

Figure 6.16: Illustration of the linearity of the MSGC and MGAP detectors. Each series of points relates to the peaks in the effective diffraction patterns

6.6 Beamline tests

The MGAP detector has been tested on two different small angle scattering stations of the Daresbury SRS and diffraction patterns of rat tail collagen have been taken. The first test was done on station 2.1 [5] and dry rat tail collagen was used. A camera distance of 1m was chosen due to the small detector area. The normalised image (after dividing by the detector response) taken using the MGAP detector is shown in figure 6.17. As mentioned in section 6.5.2 this is done in order to remove any local differences between channels. Four diffraction peaks can be seen corresponding to the 9th-12th diffraction orders. Again the non uniformity of response is due to non optimised readout electronics and some to noise pick-up. For comparison figure 6.18 shows the pattern taken from the same sample with a Molecular Dynamics image plate [6]. Tests were also performed on station 16.1 [7] using wet rat tail collagen and a 3m camera length. Figure 6.19 shows the normalised image taken with the MGAP and figure 6.20 that obtained with an image plate. Only two diffraction orders are apparent in these images due to the geometry of the apparatus.

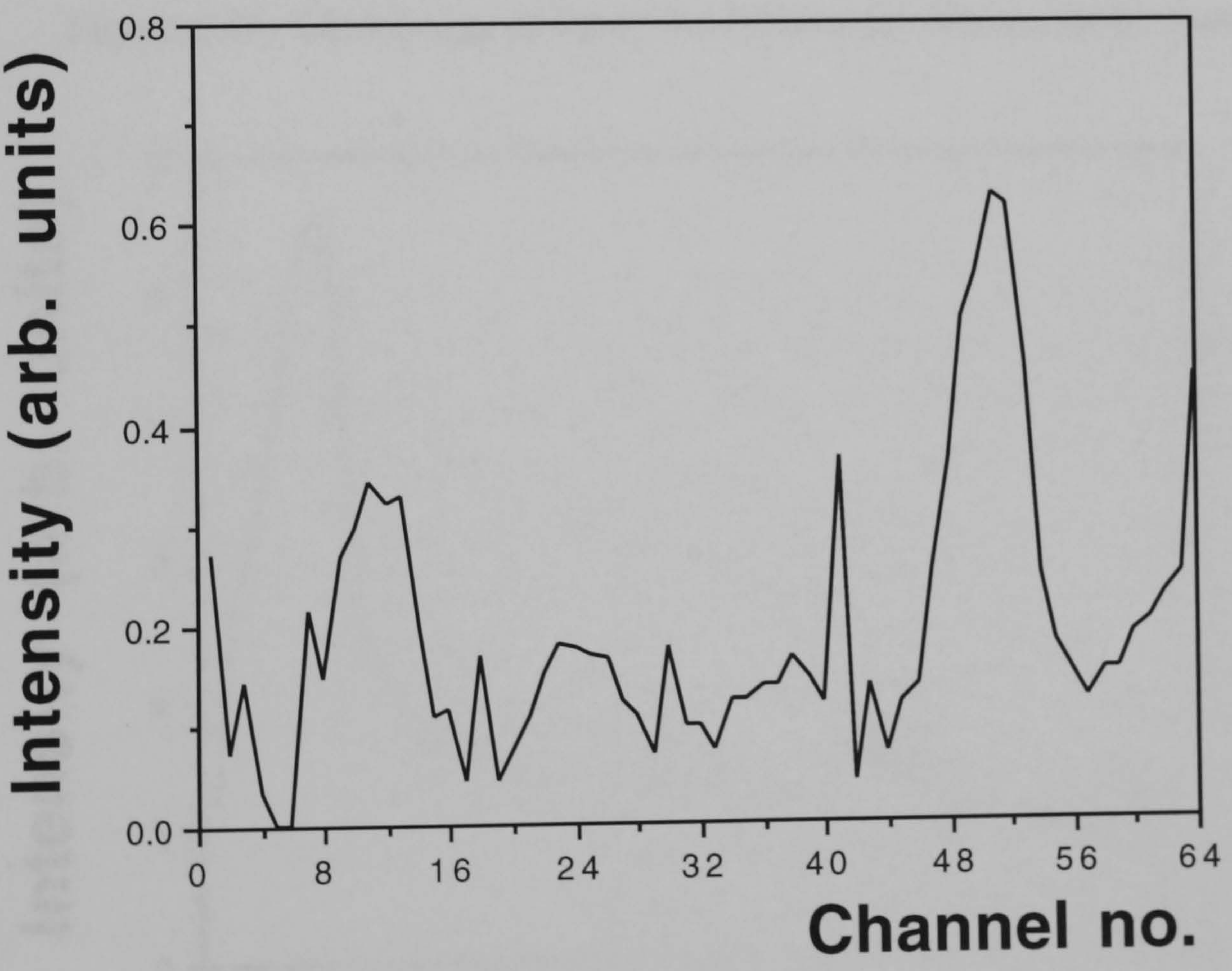

Figure 6.17: Image of 9th-12th diffraction orders of rat tail collagen taken with MGAP

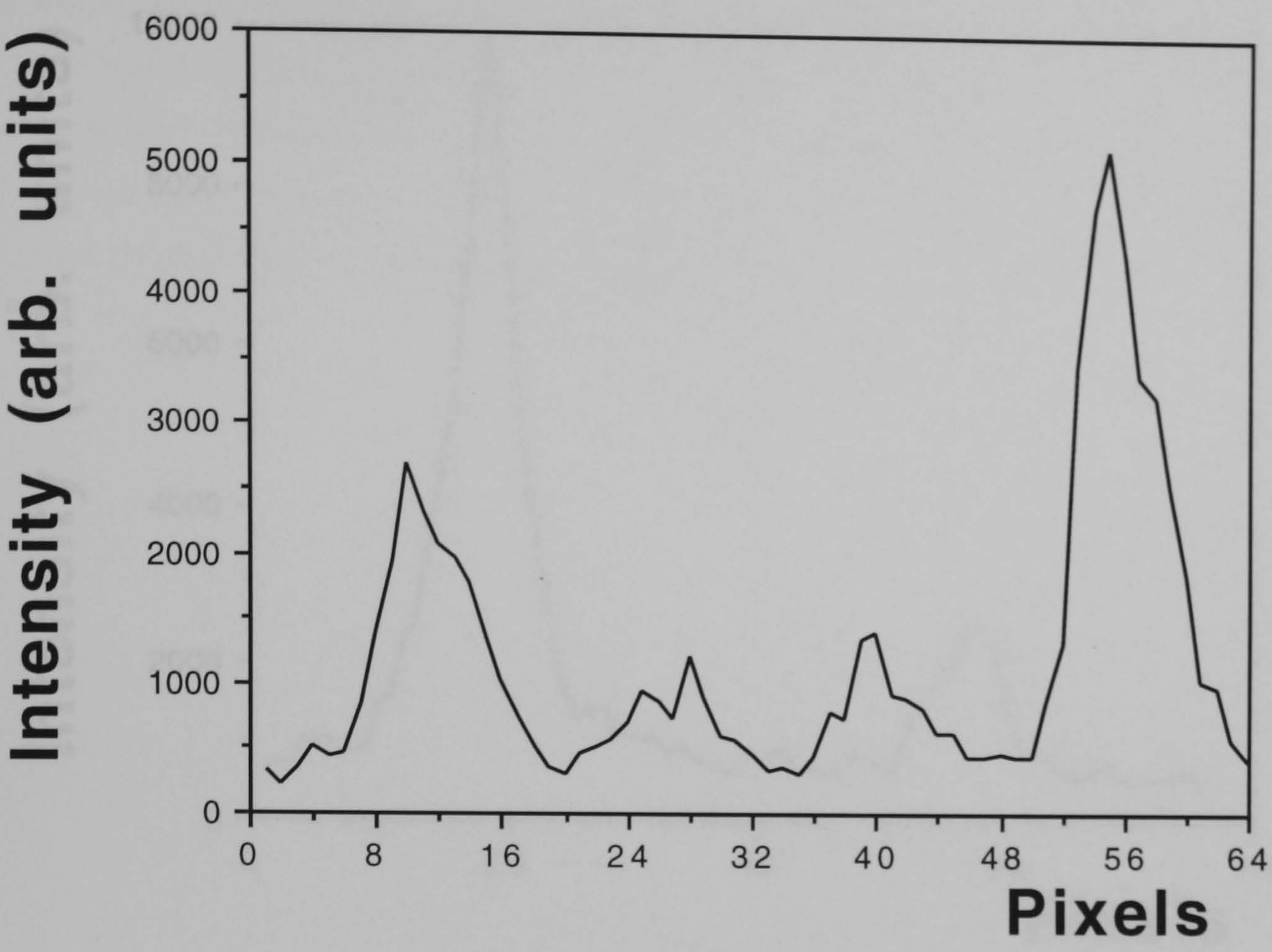

Figure 6.18: Same image as figure 6.17 but taken with an image plate

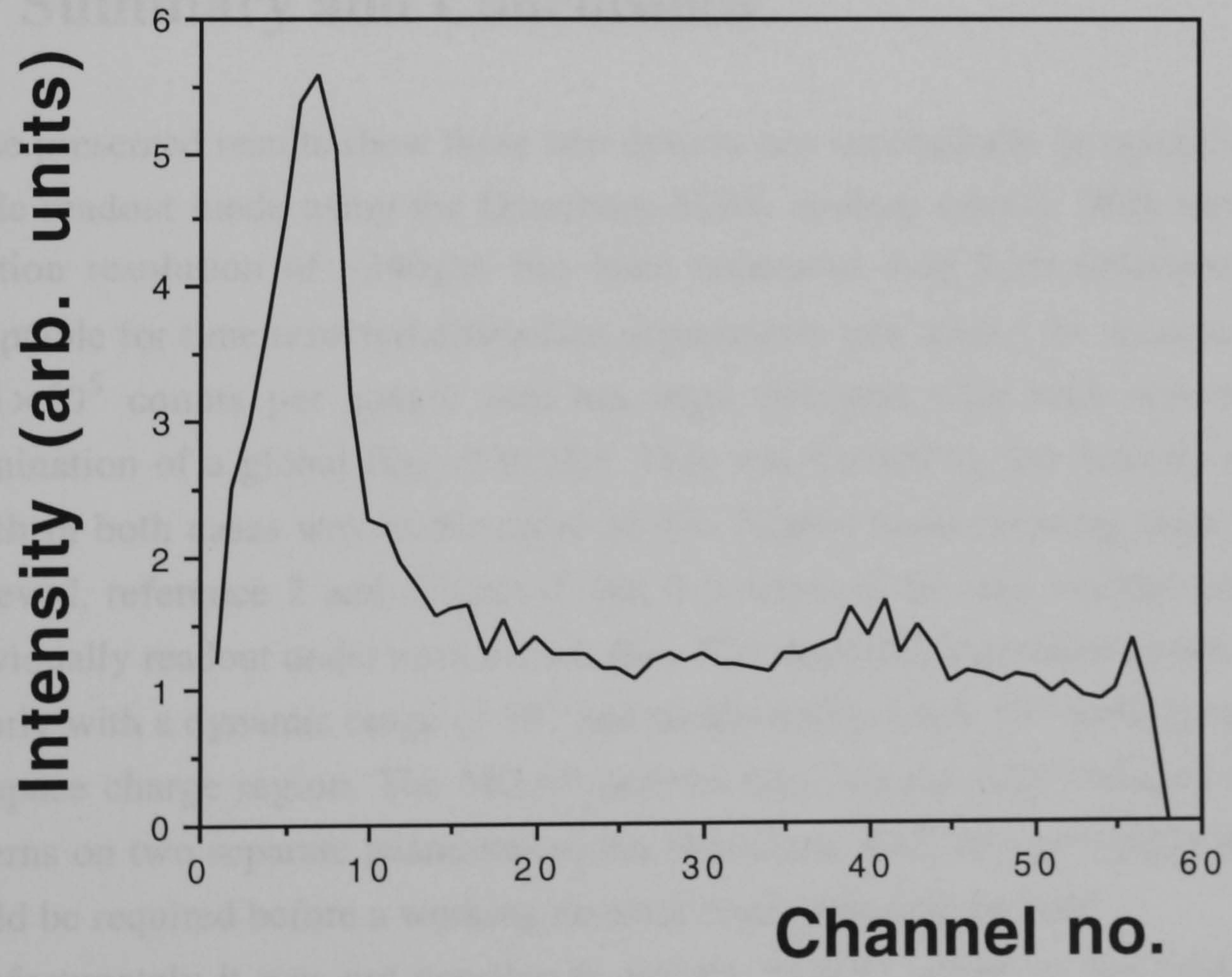

Figure 6.19: Image of 9th and 10th diffraction orders of rat tail collagen taken with MGAP

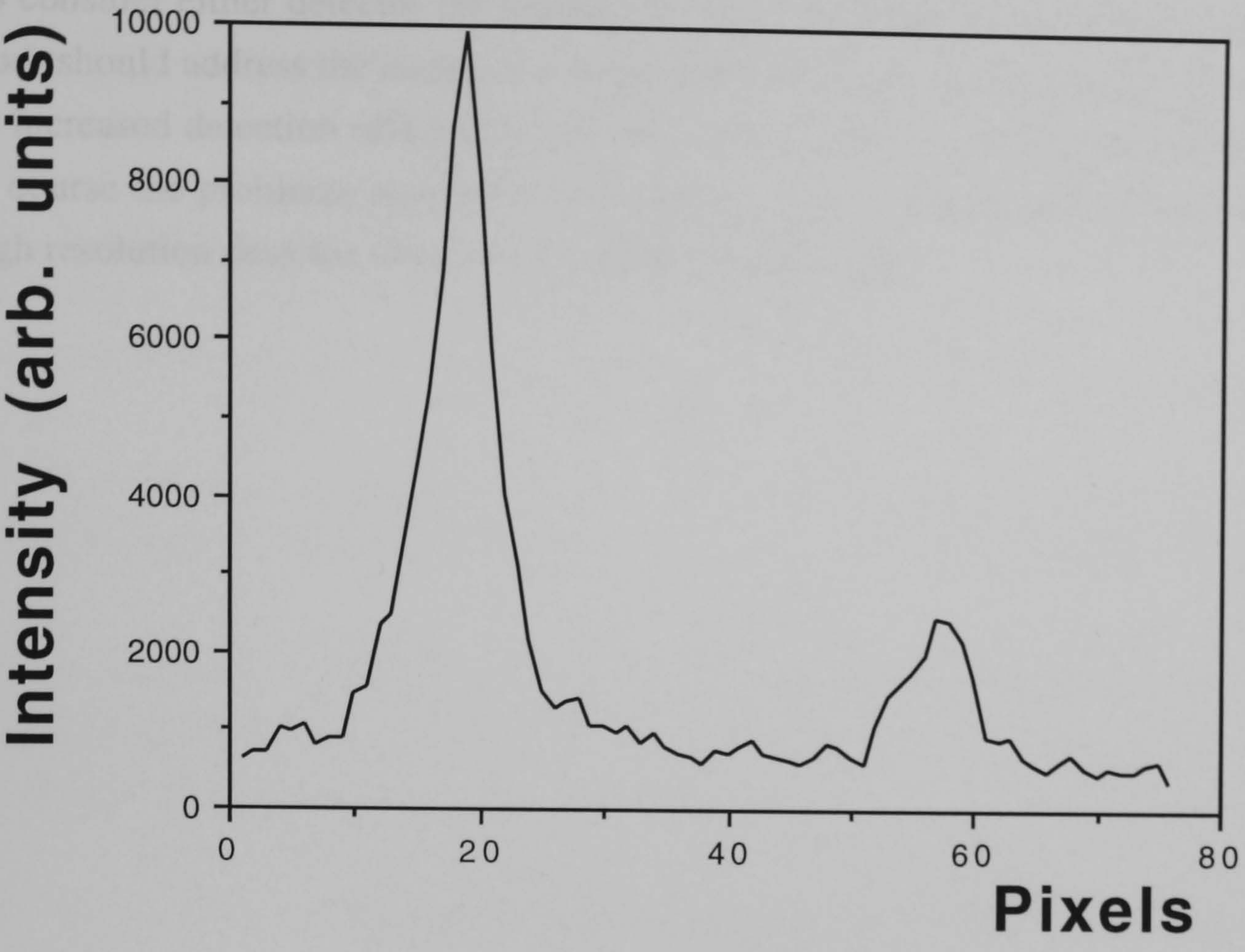

Figure 6.20: Same image as figure 6.19 but taken with an image plate

6.7 Summary and Conclusions

The presented results show these two devices can successfully be operated in single anode readout mode using the Daresbury MWL readout system. With this system a position resolution of ~240μm has been measured with both detectors which is acceptable for time resolved diffraction experiments (see table 1.1). A local count rate of 1×10^5 counts per square mm has been obtained with both detectors under illumination of a global flux of 6MHz. This was limited by the detector efficiency, which in both cases was of the order of 4%. Higher local counting rates have been achieved, reference 2 and chapter 5, but it remains to be seen whether they can be individually readout under such intense flux. The detectors have been shown to operate linearly with a dynamic range of 10^4 and should easily reach 10^5 without moving into the space charge region. The MGAP detector has "successfully" imaged diffraction patterns on two separate beamlines of the Daresbury SRS, though clearly more effort would be required before a working detector could routinely be used.

Unfortunately it was not possible to test the MSGC, which in the context of this chapter, had been specifically designed to be used with the MWL system, but as can be seen by comparing figures 6.9 and 6.10 superior diffraction images would be expected to be obtained.

To consider either detector for routine use on a small angle scattering station further work should address the issues of a larger detection area (of the order of $20 \times 20cm^2$), an increased detection efficiency (by using xenon and/or increasing the drift gap) and of course the problems associated with ageing. Once these are addressed a high rate, high resolution detector should be available for SR work.

Bibliography

[1] R.A.Lewis, N.S.Fore, W.Helsby, C.Hall, A.Jones, B.Parker, I.Sumner, J.S.Worgan, C.Budtz-Jorgensen *High counting rate gaseous x-ray detectors for synchrotron radiation applications* Rev. Sci. Instr 63(1) 1992 642-647

[2] F.Angelini, R.Bellazzini, A.Brez, M.M.Massai, R.Raffo, G.Spandre, M.A.Spezziga *The micro-gap chamber* Nucl. Instr. and Meth. A335 (1993) 69-77

[3] F.Angelini, R.Bellazzini, A.Brez, M.M.Massai, R.Raffo, G.Spandre, M.A.Spezziga, M.Bozzo *Further test and development of the micro-gap chamber* Nucl. Instr. and Meth. A349 (1994) 412-417

[4] Samtec UK, 117 Deerdykes View, Westfield, Cumbernauld, Scotland, G68 9HN.

[5] E.Towns-Andrews, A.Berry, J.Bordas, G.R.Mant, P.K.Murray, K.Roberts, I.Sumner, J.S.Worgan, R.A.Lewis *Time resolved x-ray diffraction station:X-ray optics, detectors and data acquisition* Rev. Sci. Instr. 60(7) (1989) 2346-2349

[6] Molecular dynamics

[7] N.Bliss, J.Bordas, B.D.Fell, N.W.Harris, W.I.Helsby, G.R.Mant, W.Smith, E.Towns-Andrews *W16.1: A new fixed wavelength diffraction station at the SRS Daresbury* Rev, Sci. Instr. 66(2) (1995) 1311-1313

Chapter 7

The Microdot detector

7.1 Introduction

The behaviour of the microdot gas avalanche chamber (MDOT) has been investigated. This was done in terms of the detectors energy resolution, gain characteristics, stability under illumination and different operating regimes in terms of applied drift field. In the first instance the characteristics of the first batch produced are given, which leads on to the simulation and description of a second batch of microdots. Some initial results from the second batch are also given. The set-up used for the measurements was essentially the same as that used for the characterisation of the MSGC. (See figure 5.1). The wafers were mounted on the same design of PCBs used for the MSGC as outlined in chapter 4. All the results presented here were collected with a drift gap of three millimetres.

7.2 Energy resolution

Figure 7.1 shows an Fe^{55} spectrum obtained with MDOT 4 D20V6 in an Ar:DME 80:20 gas mixture at a gain of 2000. Four distinct features can be observed:

1. noise
2. aluminium and silicon fluorescence x-rays
3. Fe^{55} escape peak
4. Fe^{55} main peak

Previously the noise levels in thin oxide MSGCs were too high to observe the aluminium and silicon peaks which in the MDOT are merged together and visible as one peak. The energy resolution is 25% FWHM / peak channel. In figure 7.2 an 8 keV Cu spectrum is shown which has been taken with a similar structure and gas mixture.

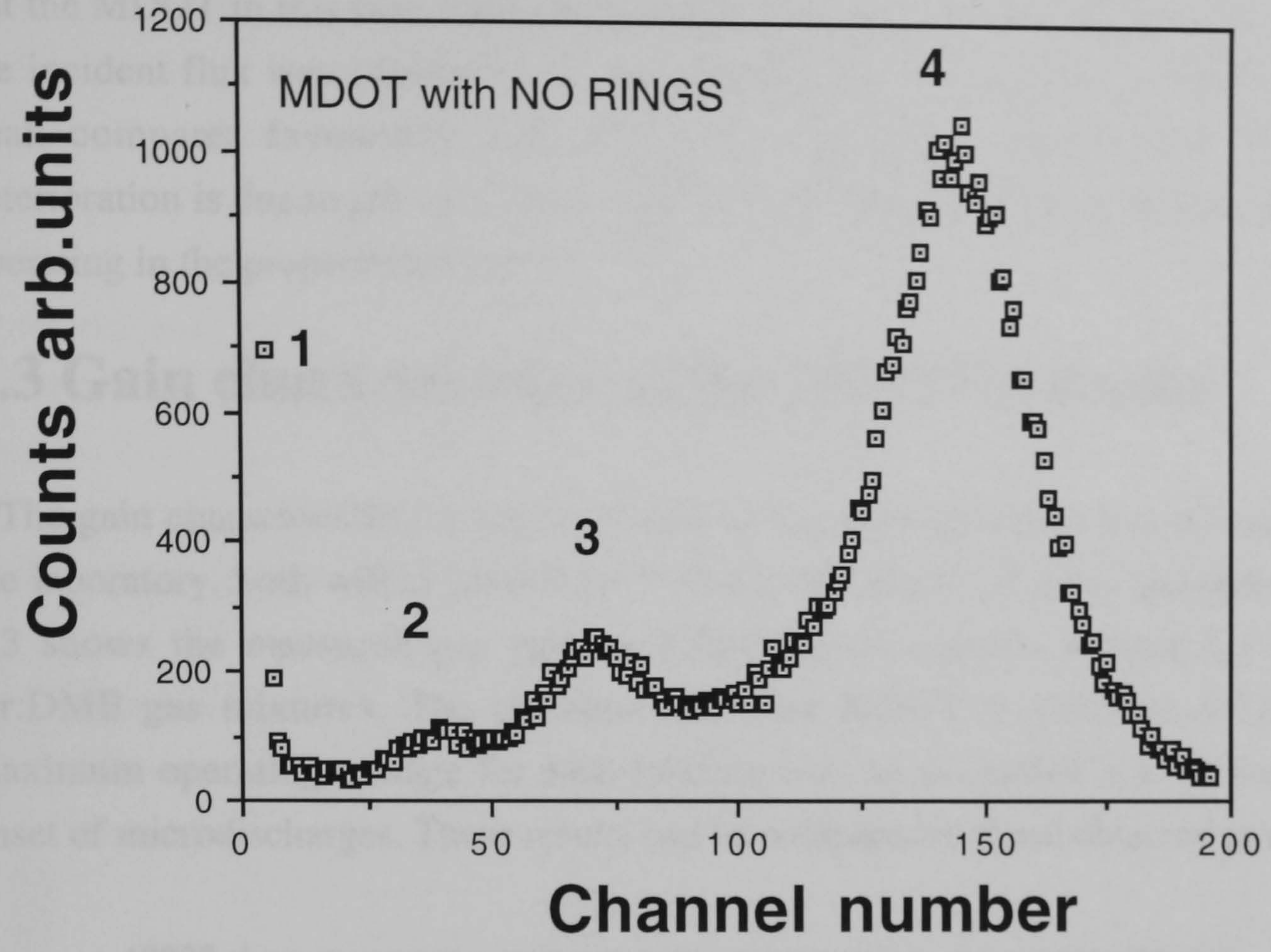

Figure 7.1: Fe^{55} spectrum taken with MDOT without rings

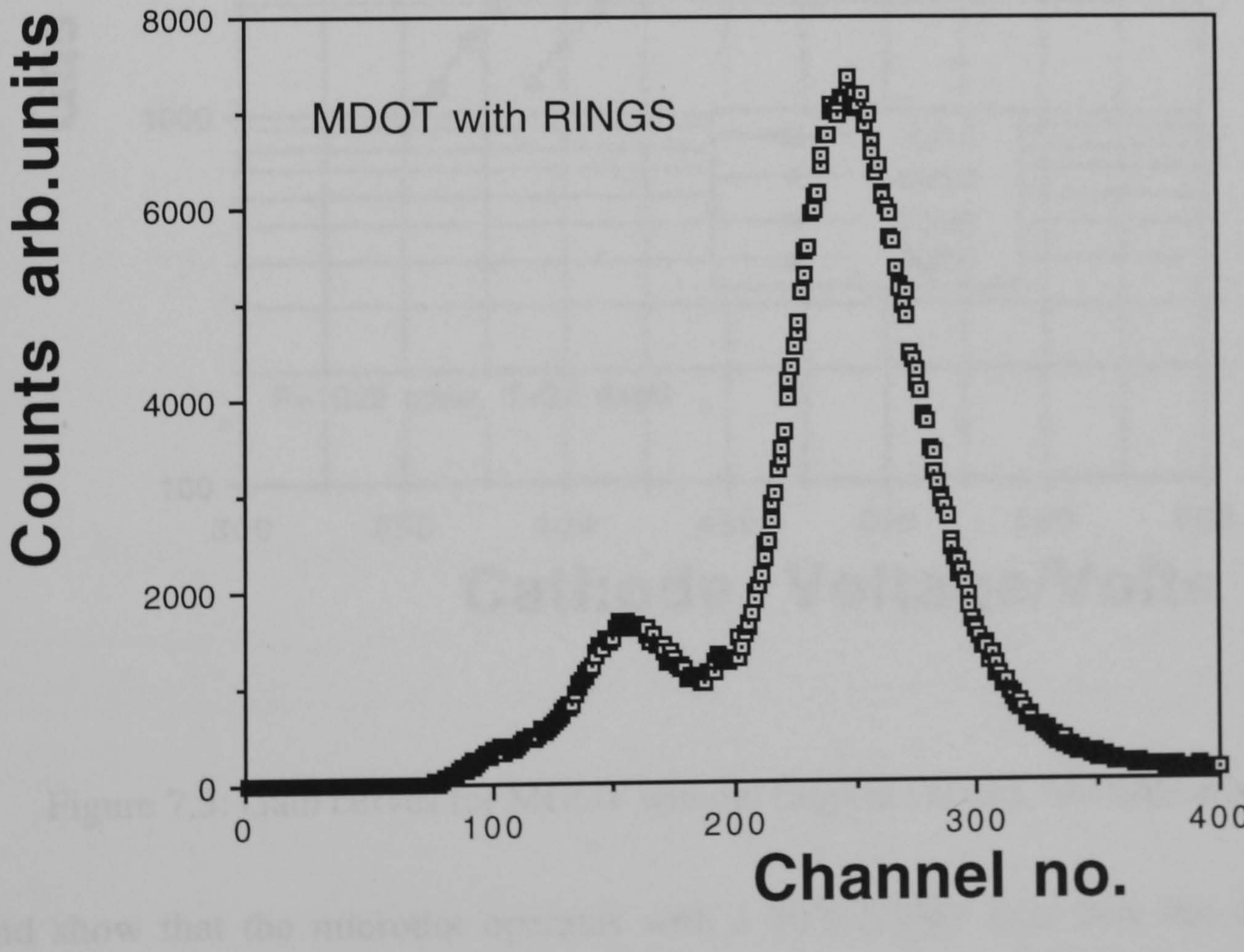

Figure 7.2: 8 keV Cu spectrum taken with MDOT with rings

but the MDOT in this case had floating rings. The gain in this situation was 5000 and the incident flux was 14kHz/mm^2. The resulting energy resolution of 19% FWHM / peak compares favourably with the 18% achieved at lower rates. The small deterioration is due to pile up in the amplifier. Both spectra indicate that the detector is operating in the proportional mode.

7.3 Gain characteristics of the MDOT detector

The gain characteristics of the first batch of microdot detectors was investigated in the laboratory, both with a 5.9keV Fe^{55} source and 8keV Cu x-ray generator. Figure 7.3 shows the measured gas gain as a function of cathode voltage for different Ar:DME gas mixtures. The chamber used was MDOT 4, structure D20V6. The maximum operating voltage for each mixture was, as in section 5.3, defined by the onset of microdischarges. These results can be compared to those obtained in chapter 4 and show that the microdot operates with a 30% higher gain than the thin oxide MSGC, at the same cathode voltage. The gas gain is thought to be limited by the creation of a small high field region between the buried anode readout bus and the surface cathode at the point of intersection, see section 4.6.2. The incorporation of the

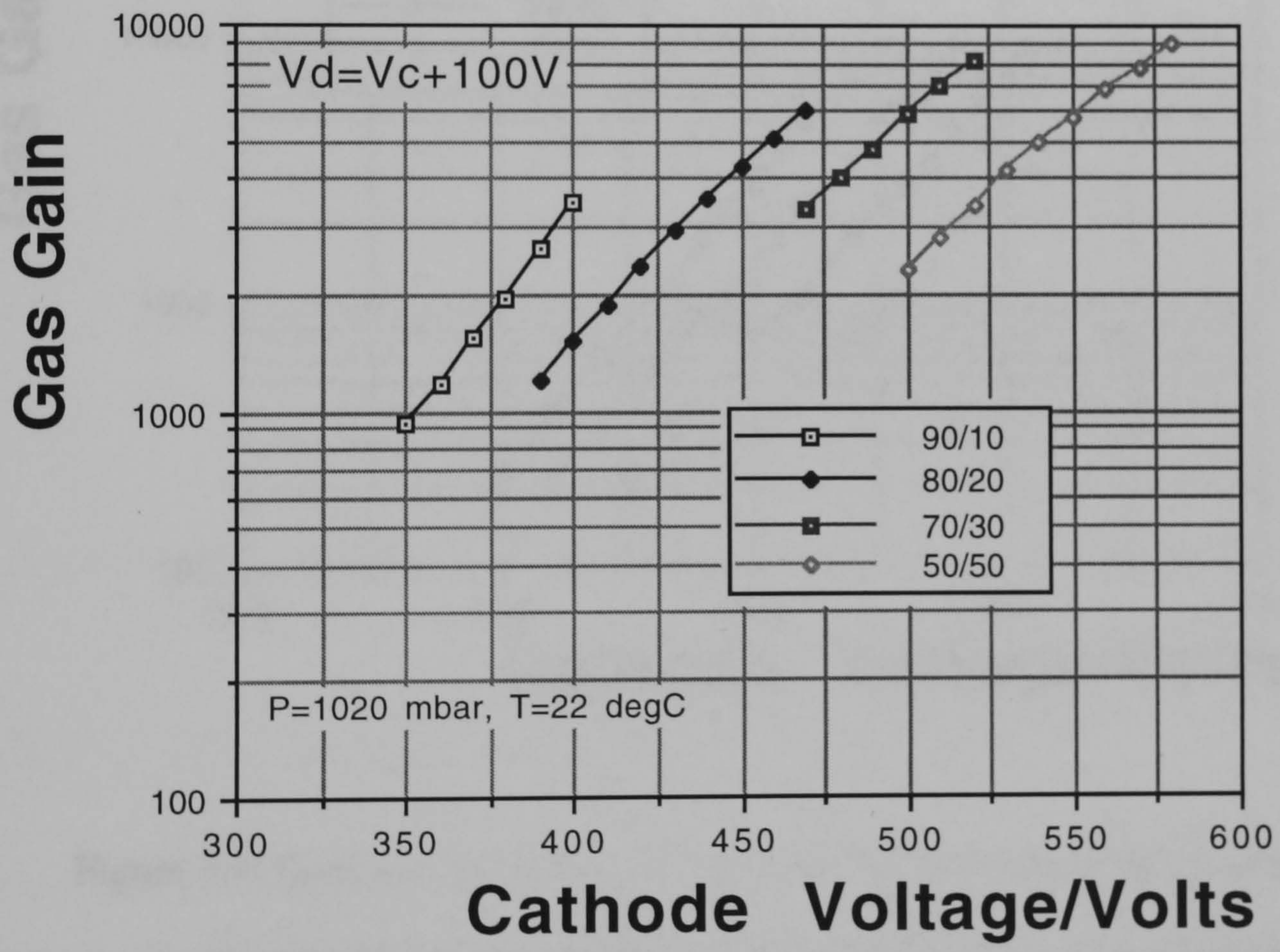

Figure 7.3: Gain curves for MDOT without rings in various Ar:DME mixtures

floating ring should reduce this effect and figure 7.4 shows the gain curves obtained with a microdot with rings. As can be seen from the figure, higher gas gains are achieved for all the gas mixtures and table 7.1 highlights this further. Also included in the table is a comparison between the different pitch MDOT structures in a gas mixture of 70:30 Ar:DME. Figure 7.5 shows a comparison of the gain of the various microdot structures in an 80:20 Ar:DME gas mixture. The figures show that the gains of all the 200 μm pitch structures are very similar at the same cathode voltage. Table 7.1 shows that the 100 μm pitch structure operates 40 volts lower for the same gain. The 100 μm structure attains roughly the same upper gain limit as the 200 μm pitch structure and achieves at least 4 times the gain obtainable with a 100 μm pitch MSGC. These results

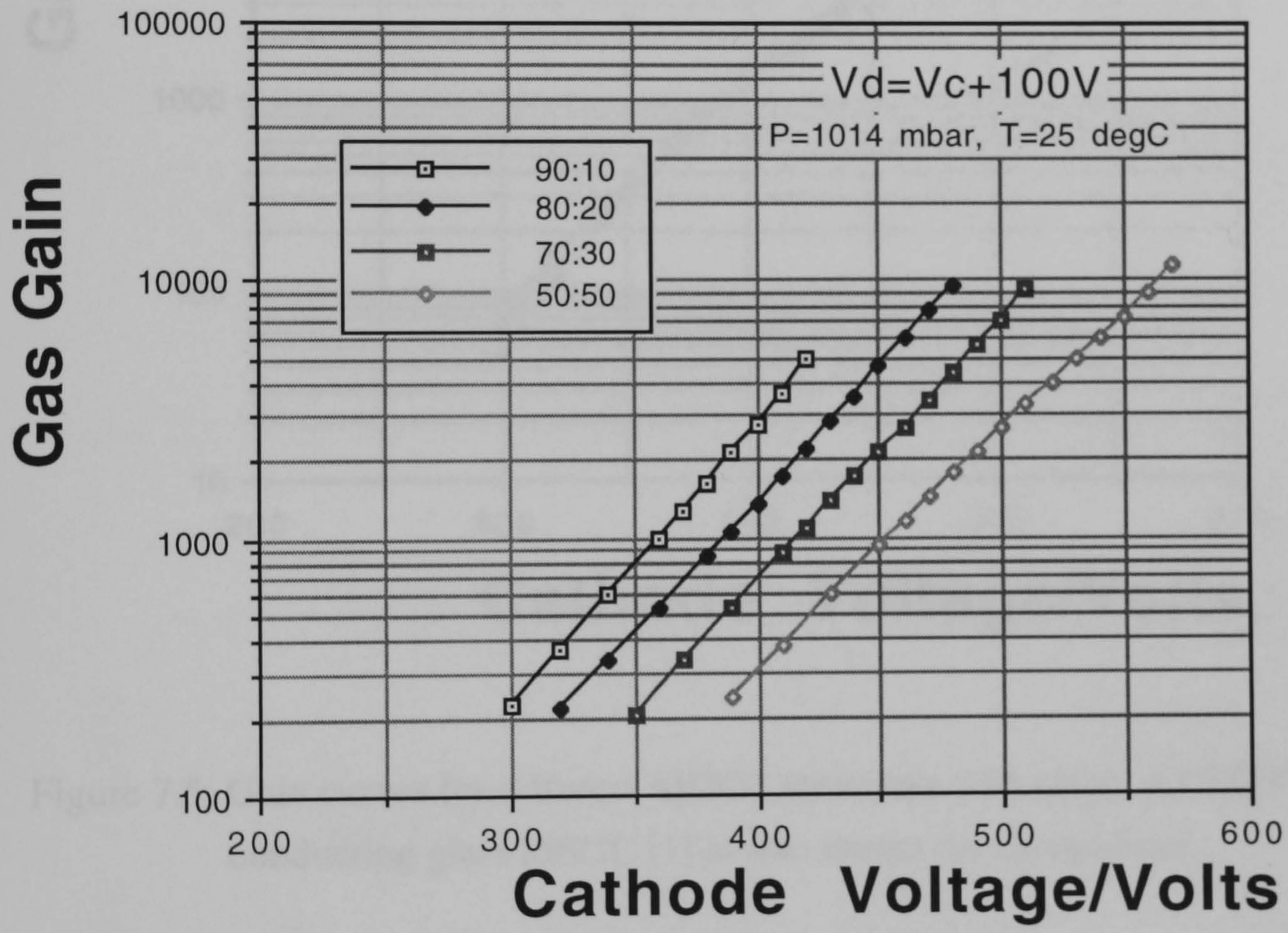

Figure 7.4: Gain curves for MDOT with rings in stated Ar:DME mixtures

Gas Mixture	MDOT No rings	MDOT with rings	200 μm pitch	100 μm pitch
90:10	3430	5008		
80:20	6000	9417		
70:30	8060	9261	11020(Vc540V)	10764(Vc510V)
50:50	9050	11261		

Table 7.1: Maximum gains in Ar:DME gas mixtures for MDOTs with and without rings. Also included is a comparison between the 100 and 200 μm pitch structures.

can be compared to those obtained with a standard MSGC on semi-conducting glass [1]. The results show a similar gas gain dependence with gas mixture, but the microdot operates at approximately 120 volts less for the same gain. Also the maximum sustainable gain for the MSGCs in [1] is ~7000 compared with ~10000 for the microdot.

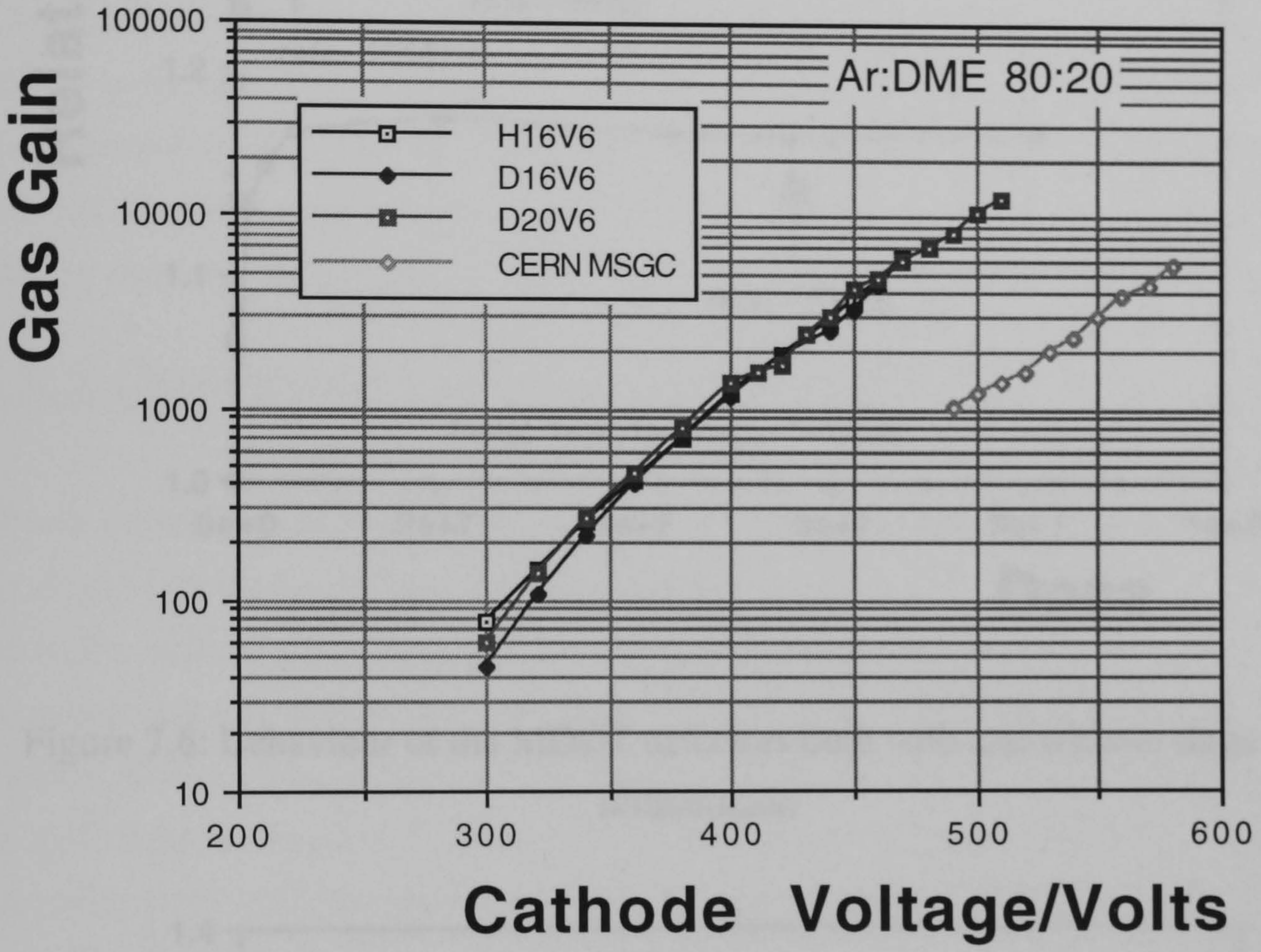

Figure 7.5: Gain curves for different MDOT structures with rings. A CERN semi-conducting glass MSGC [1] is also shown for comparison.

7.3.1 Gain Stability under Illumination

The gain behaviour of the microdot detector under sustained illumination is examined in this section. The detector is exposed to 8 keV x-ray source and the resulting behaviour for detectors both with and without floating rings is shown in figure 7.6. For the detector with no rings the initial rate of irradiation was ~14kHz/mm^2 whereas for the detector with rings the rate was ~500kHz/mm^2. The quantity 'dose' in the figure is simply the rate multiplied by the time. The figure shows that for the detector without rings there is an increase in gain of ~30% under illumination and further studies showed that this was independent of rate. This behaviour can be understood by considering the interaction of the anode fields with the substrate fields. As has been mentioned in section 4.6.2, the anode and substrate fields

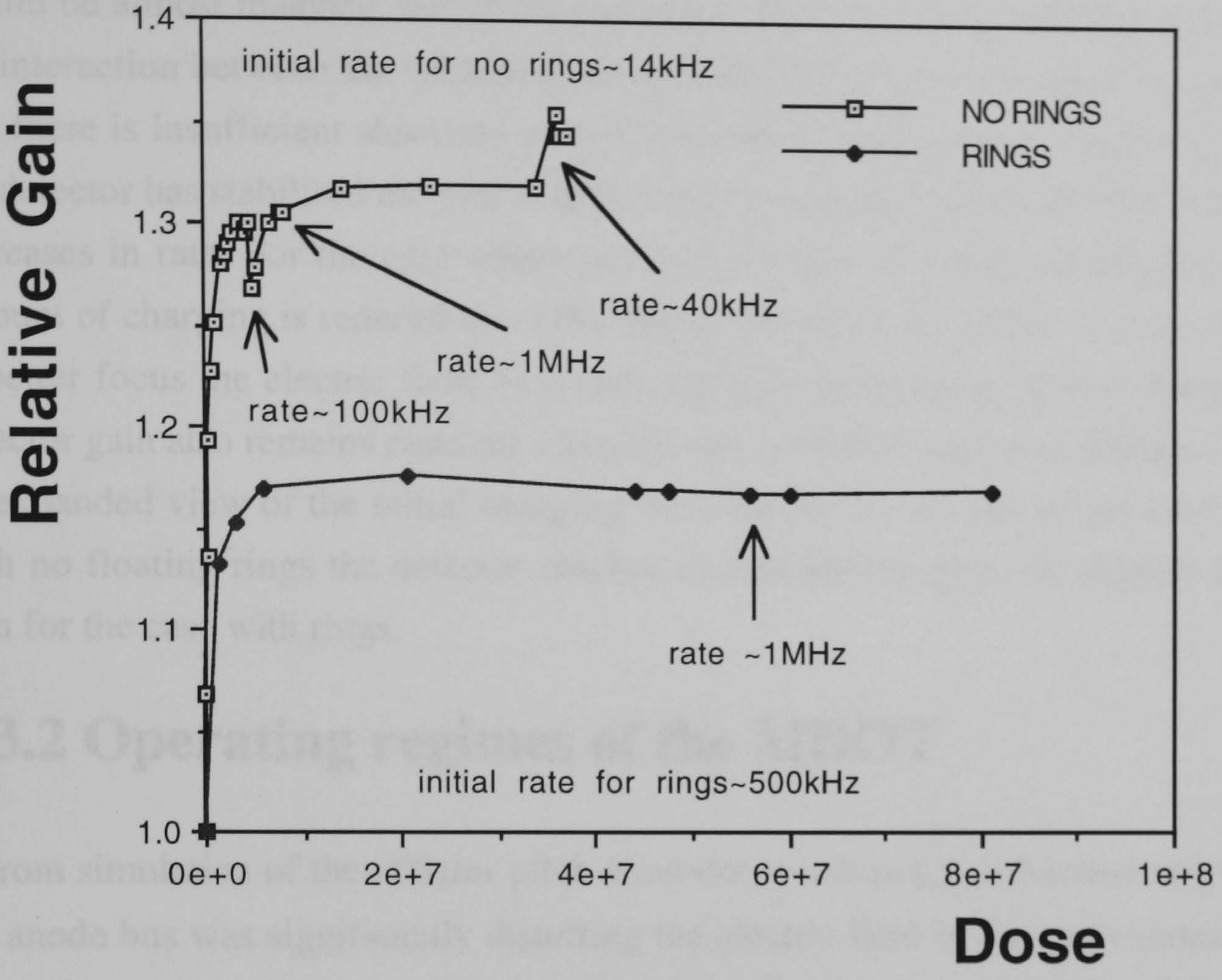

Figure 7.6: Behaviour of the MDOT detectors both with and without rings under illumination

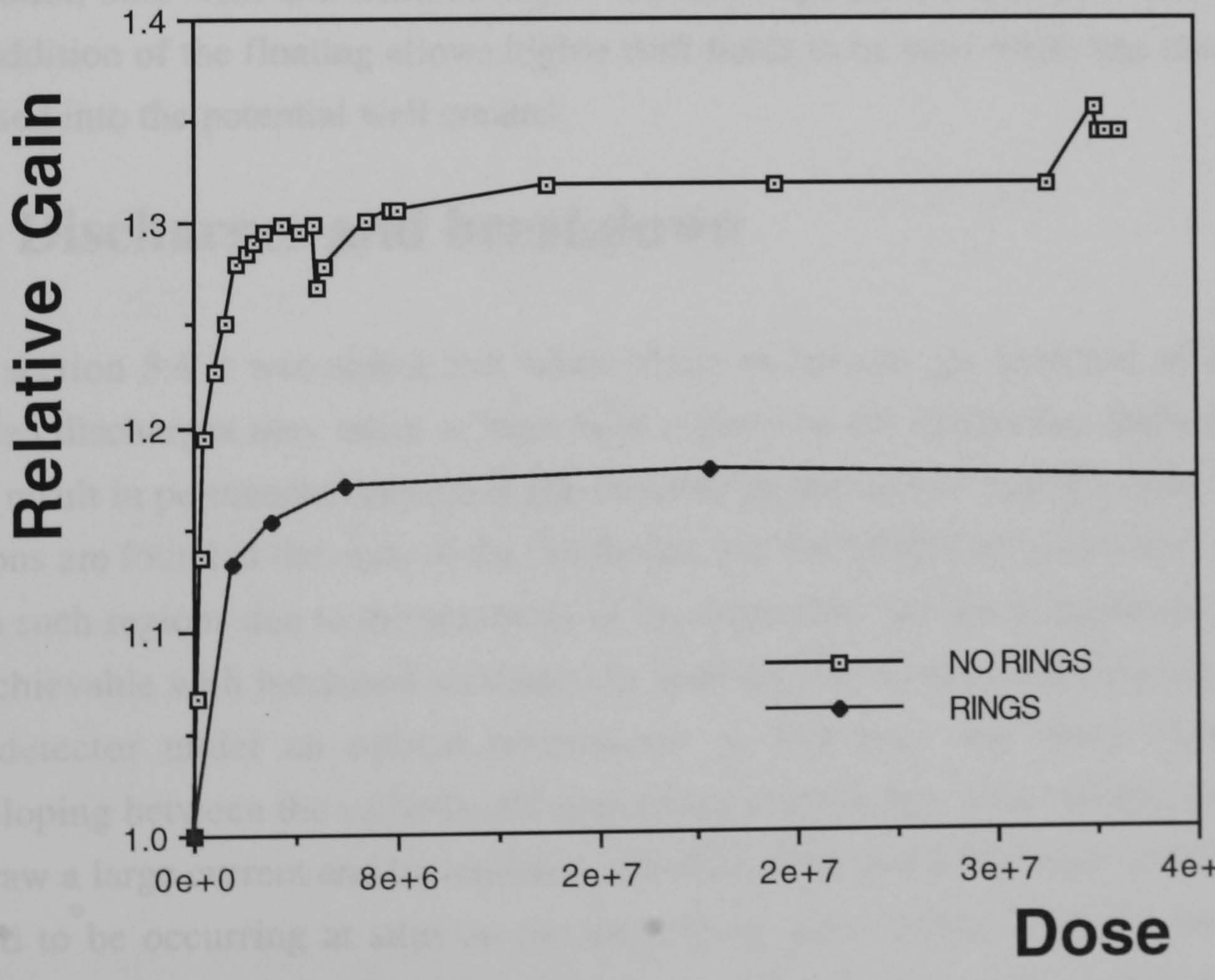

Figure 7.7: Enlarged view of figure 7.6 showing initial rise in gain

should be almost matched, due to the geometry. However, this matching is broken by the interaction between the substrate and the underlying anode readout bus and shows that there is insufficient shielding current flowing at their point of intersection. Once the detector has stabilised the gain of the chamber remains almost constant with further increases in rate. For the case where the detector has an additional floating ring the amount of charging is reduced to ~17%. Hence the inclusion of the floating ring helps to better focus the electric field lines onto the dots so resulting in less charging. The detector gain also remains constant when the rate is further increased. Figure 7.7 shows an expanded view of the initial charging from figure 7.6. As can be seen for the case with no floating rings the detector reaches its equilibrium gain for slightly less dose than for the case with rings.

7.3.2 Operating regimes of the MDOT

From simulation of the $200\mu m$ pitch microdot structure [2], it became apparent that the anode bus was significantly distorting the electric field in the gas volume directly above the surface of the bus. This has the effect of creating a potential well into which electrons can fall and be focused onto the bus lines rather than the anode dots. The fraction of electrons falling into the well is small for low drift fields but increases as the drift field is increased. This can be seen in figure 7.8, where the relative gain of the microdot, both with and without rings, is plotted against the applied drift field. Thus the addition of the floating allows higher drift fields to be used while less electrons are focused into the potential well created.

7.4 Discharges and breakdown

In section 5.4 it was stated that when trying to operate gas detectors at high gain, sudden discharges may occur at high field regions on the electrodes. Such discharges may result in permanent damage of the detector. In the case of MSGCs these high field regions are found at the ends of the electrodes, but the MDOT structure does not suffer from such regions due to the geometry of its electrodes. Therefore higher gains should be achievable with increased resistance to sparking. However, following inspection of the detector under an optical microscope, it was seen that short circuits were developing between the cathode and underlying readout bus, thus causing the detector to draw a large current and be rendered unusable. This 'punch-through' breakdown was found to be occurring at sites on the underlying metal where 'hillocks' had formed. These are regions on the aluminium metal layer where a movement of grain boundaries has occurred causing a raise in profile at the point. This is a common occurrence in the semi-conductor industry [3] and is due to the high temperatures used during the deposition of the oxide layer. This is shown schematically in figure 7.9.

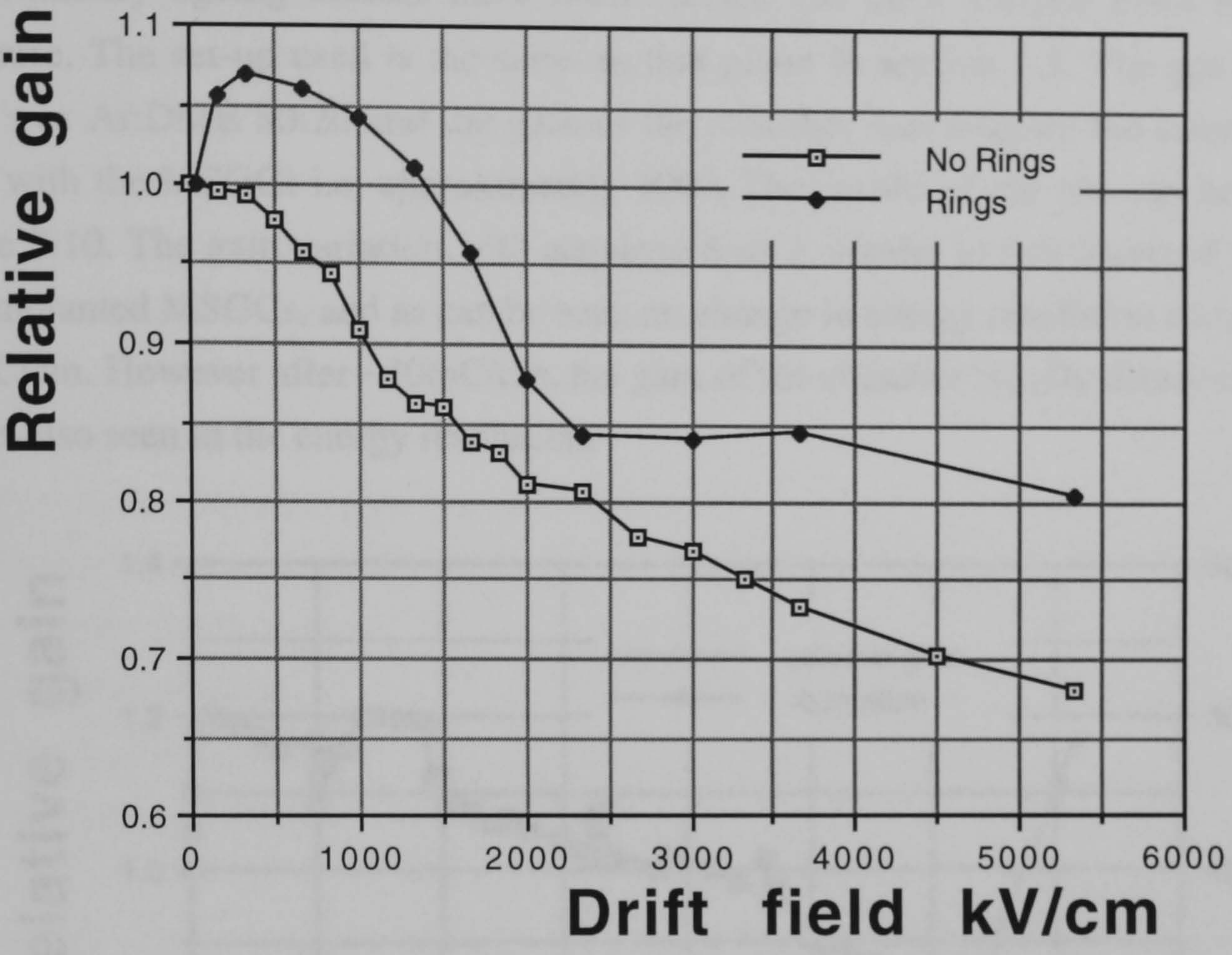

Figure 7.8: Variation of MDOT gain with applied drift field

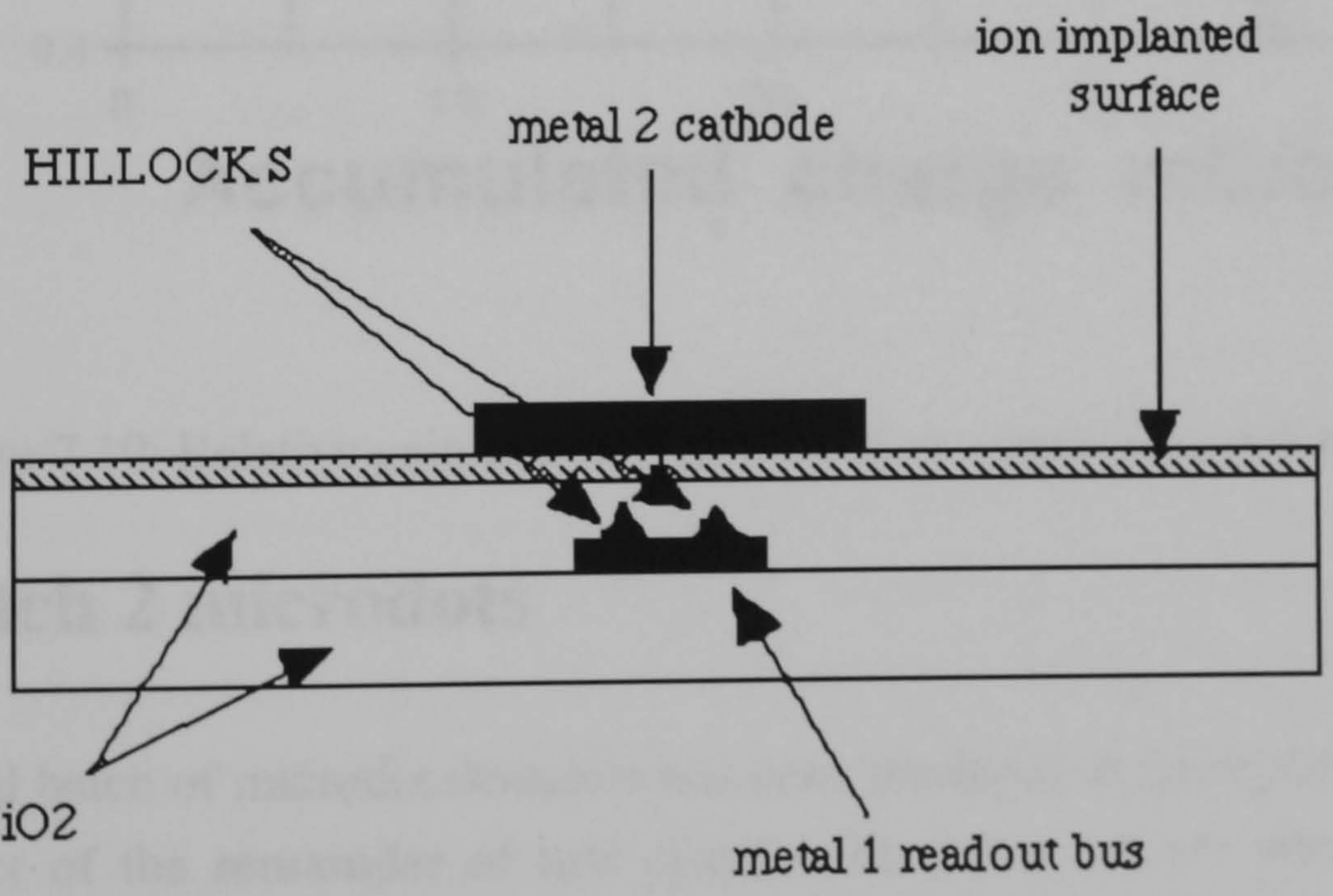

Figure 7.9: Schematic representation of 'hillocks' on the metal 1 surface

7.5 High rate ageing studies

Preliminary ageing studies have been carried out on a 100μm pitch microdot structure. The set-up used is the same as that given in section 5.5. The gas mixture used was Ar:DME 80:20 and the gain of the chamber was roughly the same as that used with the MSGCs i.e. approximately 1000. The results of the test can be seen in figure 7.10. The gain variation with acquired dose is similar to that obtained with the ion implanted MSGCs, and as can be seen no change in energy resolution occurs up to 25mC/cm. However after ~30mC/cm, the gain of the chamber rapidly deteriorates and this is also seen in the energy resolution.

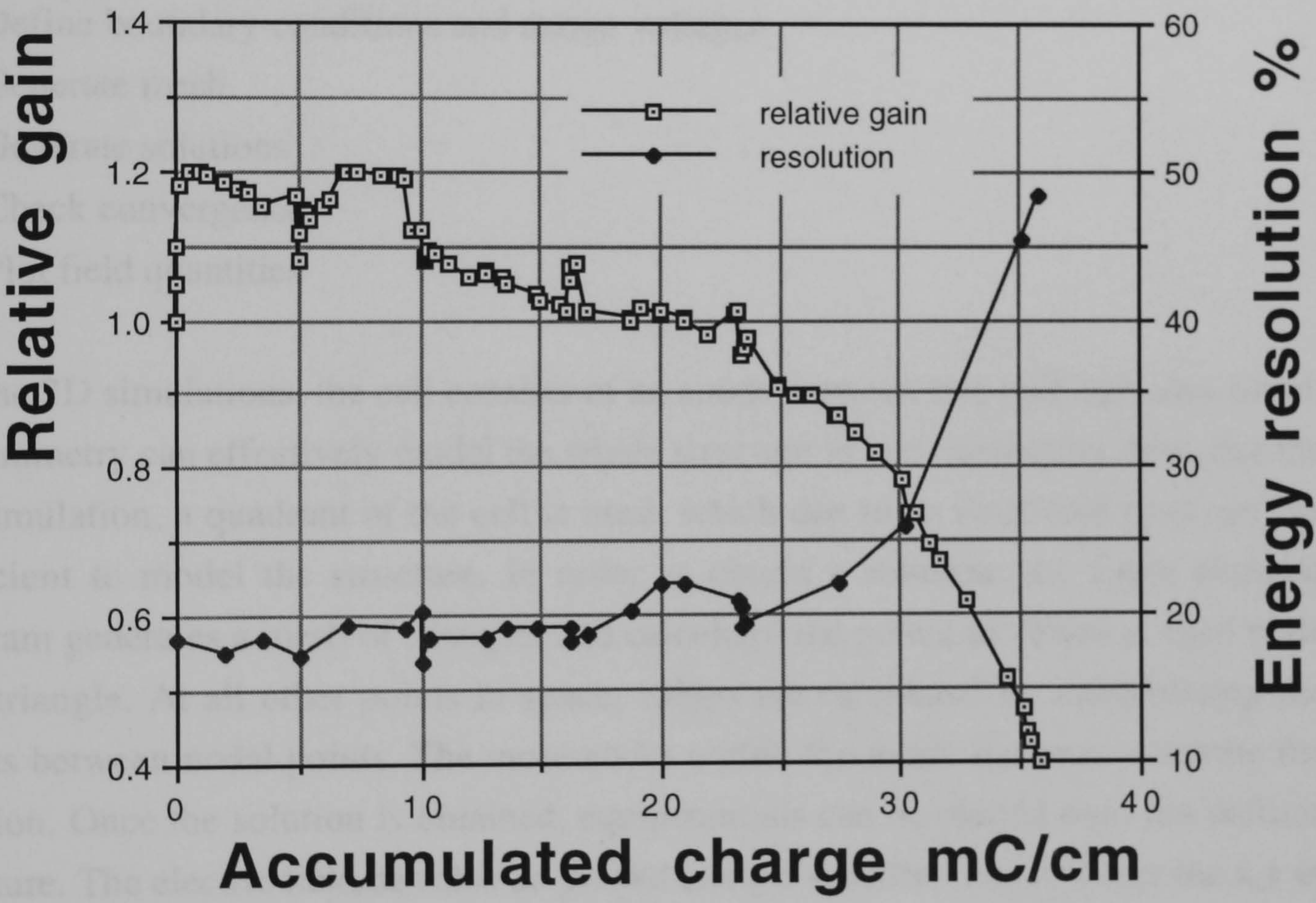

Figure 7.10: Relative gain and energy resolution versus accumulated charge

7.6 Batch 2 microdots

A second batch of microdot detectors has been produced at Liverpool which will be the subject of the remainder of this chapter. However, before the new design is introduced, a brief description of some of the simulation which has been undertaken will be given. The description of the new design along with some preliminary results will then be given.

7.6.1 The Maxwell field simulator

The Maxwell field simulator [4] is a package that uses finite element analysis to simulate electric and magnetic fields in user specified devices. Both 2D and 3D versions exist and have been used to simulate the electric field in the microdot structures. The procedures for solving an electrostatic problem are as follows:

1. Define units and dimensions to be used
2. Choose solver (electrostatic, dc-conduction etc.)
3. Define cell to be modelled
4. Assign properties to materials in the model
5. Define boundary conditions and assign voltages
6. Generate mesh
7. Generate solutions
8. Check convergence
9. Plot field quantities

For the 2D simulations, the cell consists of an anode between two half cathodes which by symmetry can effectively model the whole structure in less computing time. For the 3D simulation, a quadrant of the cell is used, which due to its rotational symmetry is sufficient to model the structure. In order to obtain a solution, the finite element program generates a mesh of triangles and calculates the potential values at each node of a triangle. At all other points in space, values are calculated by interpolating the values between nodal points. The more nodes within the mesh, the more accurate the solution. Once the solution is obtained, equipotentials can be plotted onto the defined structure. The electric field can also be plotted along a specified line in either the x,y or z plane.

Simulated geometry

The structure modelled is a 200 micron pitch MDOT with varying oxide thicknesses and with different permutations of readout bus and floating rings. Figure 7.11 shows two views of one of the models in the defined x-y and y-z planes. Experience from the simulation of implanted MSGCs [5] has shown that the ratio of surface to volume conductivity is the important parameter rather than their exact conductivities, and that this ratio is optimum at 500. In the simulations the implant layer has a thickness of $0.5\mu m$, which is twice the expected range of the implanted boron ions. This is to increase the aspect ratio between implanted layer and oxide as the solution of the simulation tends not to converge otherwise. Now because twice the thickness of implant is used, the conductivity of the layer will be halved and in order to keep the ratio of surface to volume resistivity at 500, the implanted layer is set at a conductivity 250 times that of the oxide. The thickness of the metal is $1.4\mu m$ for all models and the oxide thickness is varied from 1 to $2\mu m$. The anode is set to zero potential and the cathode is set at -500 volts. For simulations involving the ring structure then the ring is left to "float". The underlying readout bus is varied in shape and thickness from 3 to 8 microns. The drift plane is placed at a distance of 125 microns from the surface layer, to reduce the number of triangles used in the solution, and is set to -530 volts which is equivalent to a drift field of $2.4kVcm^{-1}$.

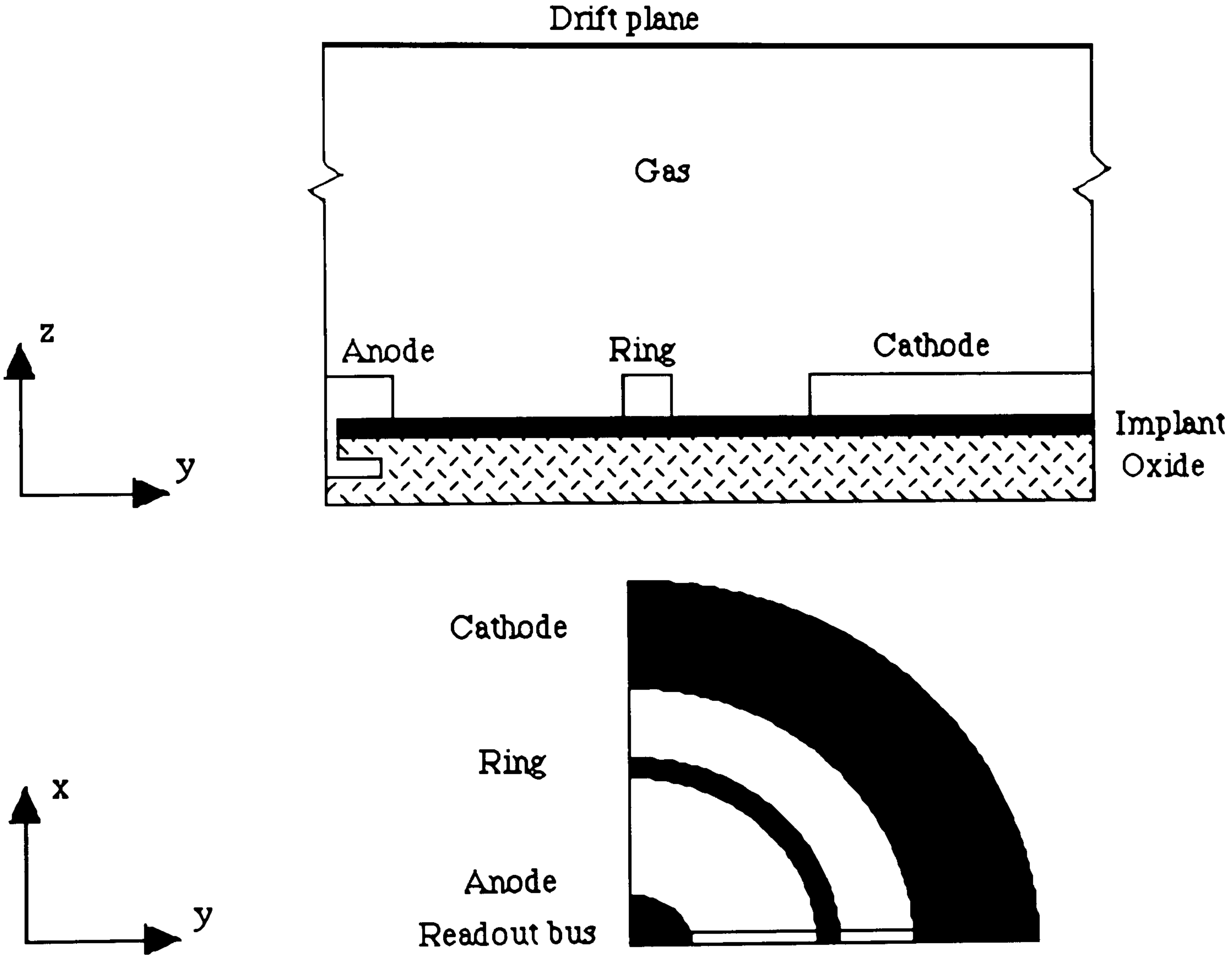

Figure 7.11: MDOT model used in simulation

7.6.2 Results from simulation

Table 7.2 shows the differences between the models simulated. The first batch of MDOTs produced were models 1 and 2. Once the simulation is complete the electric field for the defined structure may be plotted along with various other quantities along specified lines or planes. Figure 7.12 shows a plot of the potential along three lines in the plane $z=1.4\mu m$, which is the thickness of the electrodes, along the x axis (1), the y axis (2) and at 45^{o} to both these axis (3) from the anode edge to the cathode edge for the first model. In the figure the two lines which are approximately equal are lines 1 and 3. Line 2, which is the line above the readout bus, shows the problem mentioned in section 7.3.2 which is the creation of a potential well. Thus electrons created in the avalanche can fall into this well and be focused onto the surface of the wafer above the bus line. This results in an increase of gain within the detector as electron accumulation on the surface reinforces the electric field set by the geometry. This effect can be seen in figure 7.6. To combat this effect, a metal ring is placed on the surface between anode and cathode and is left at floating potential. The effect of the ring is to force the electric field lines onto the anode dot and thus reduce the effect of the underlying readout bus. Further simulation showed that by reducing the thickness of the readout bus and increasing the thickness of the oxide both help to suppress the production of a potential well. Figure 7.13 is the same as for 7.12 but for model 12, which clearly shows this effect. This model has two floating rings which again aids in reducing the effects from the bus line. Studies have also been carried out where the crossover region of surface cathode and buried bus has been reduced by a factor of 20 and in some cases where there is no crossover at all. This will be covered more in the next section.

Model number	Thick bus	Thin bus	Thick oxide	Thin oxide	No rings	One ring	Two rings
1	√			√	√		
2	√			√		√	
3	√			√			√
4		√		√	√		
5		√		√		√	
6		√		√			√
7	√		√		√		
8	√		√			√	
9	√		√				√
10		√	√		√		
11		√	√			√	
12		√	√				√

Table 7.2: The table shows the various differences between the simulated models

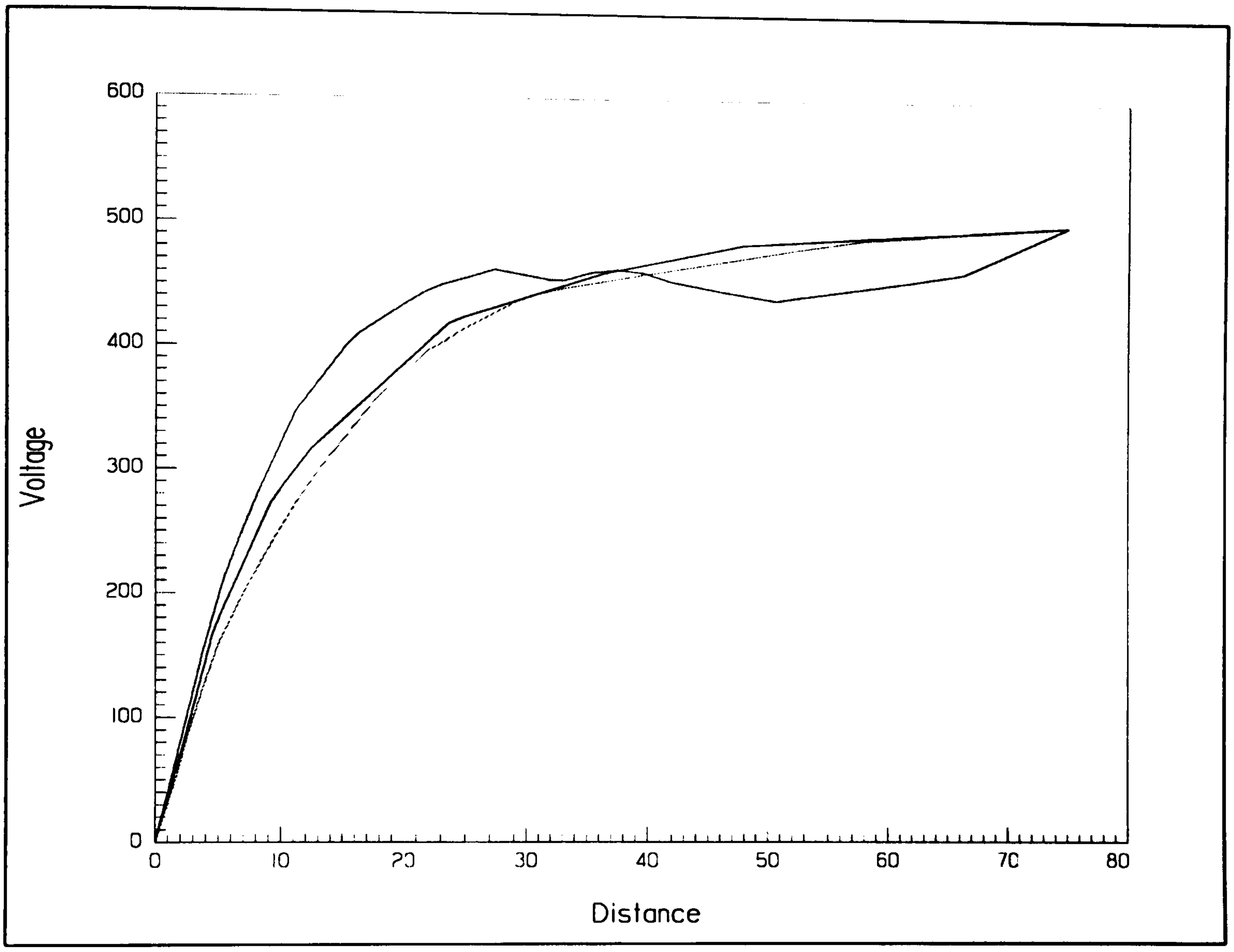

Figure 7.12: Potential along three lines in z=1.4 plane for model 1. (The distance scale is in microns, the voltage scale is in volts)

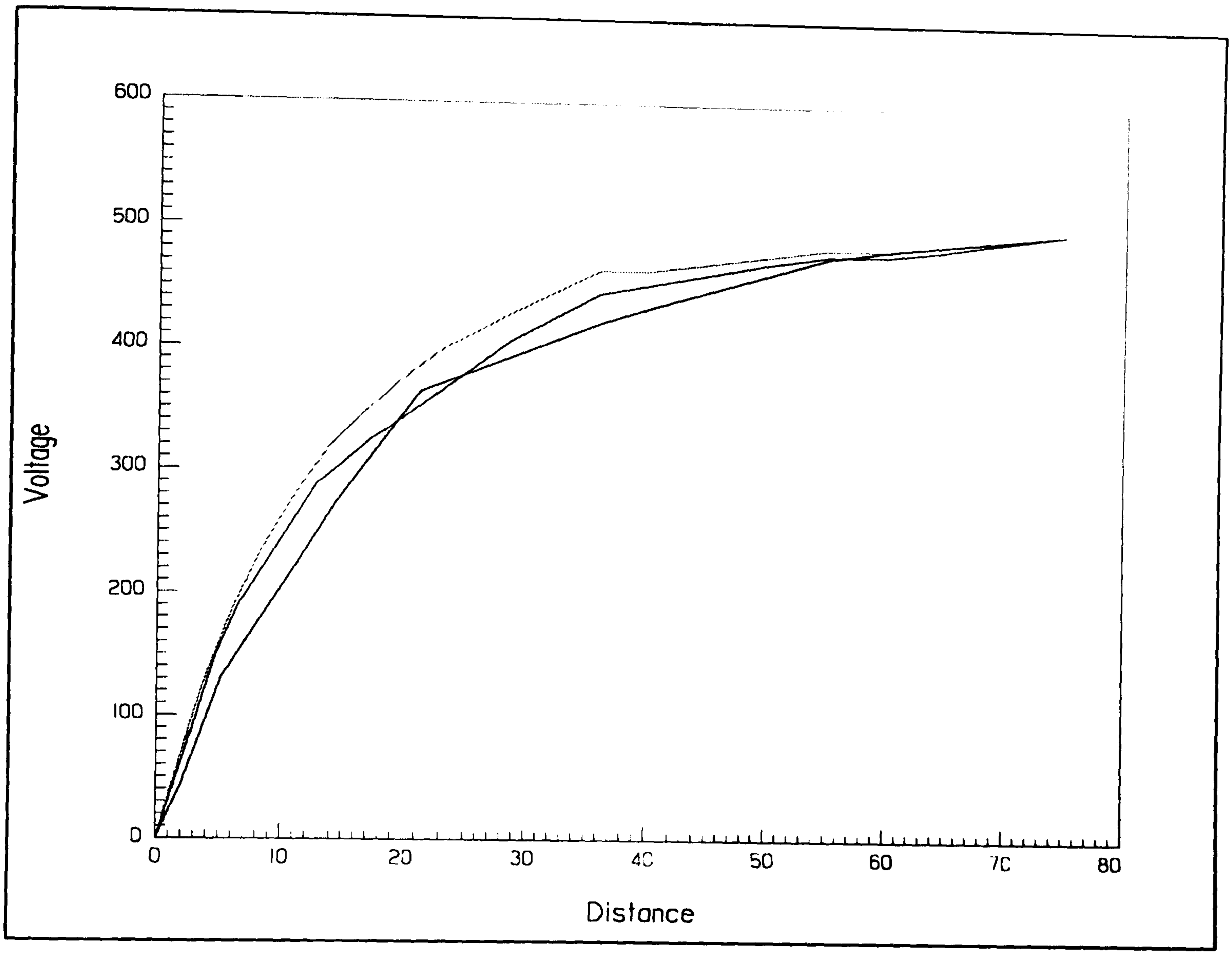

Figure 7.13: Potential along three lines in z=1.4 plane for model 12. (The distance scale is in microns, the voltage scale is in volts)

7.7 The new microdot design

A second batch of microdot detectors has been produced and tested. The main differences between the two batches are in the geometry of the electrodes and in the manufacturing of the wafers. For the first batch, the intermetal oxide was $1.8\mu m$ thick. This has been increased to $2.8\mu m$ in order to reduce damage from punch through breakdown due to hillock formation. The mask design was also improved to reduce the metalised area on the cathodes which covers the busline. This serves to reduce capacitance and also improves the reliability from punch through breakdown. In addition to these changes, some structures have been designed with the possibility of 2D readout whilst some may be readout using charge division. These changes in design are shown in figure 7.14 where 7.14a is the design of the first batch with rings; 7.14b is the design of a reduced crossover structure and 7.14c shows a 2D readout structure. The wafers have been produced with 13 different structures the geometries of which are given in table 7.3 along with the number of rings, the pitch and the method of readout, where CD stands for charge division.

Structure	Anode diameter(μm)	Pitch (μm)	Readout method	No. of rings	Crossover?	Abbreviation
1	16	200	2D	3	Yes	D16V6R3.2D
2	20	200	2D	2	Yes	D20V6R2.2D
3	20	200	2D	1	Yes	D20V6R1.2D
4	16	200	CD	2	Yes	D16V6R2
5	20	200	CD	2	No	D20V6R2.NC
6	20	200	CD	1	Yes	D20V6R1
7	24	200	CD	1	Yes	D24V6R1
8	12	100	CD	1	Yes	D12V6R1
9	12	100	CD	1	No	D12V6R1.NC
10	12	100	2D	0	Yes	D12V6R0.2D
11	12	100	2D	1	Yes	D12V6R1.2D
12	10	100	2D	1	Yes	D10V4R1.2D
13	10	100	2D	0	Yes	D10V4R0.2D

Table 8.2: Description of the various structures produced in the second batch.

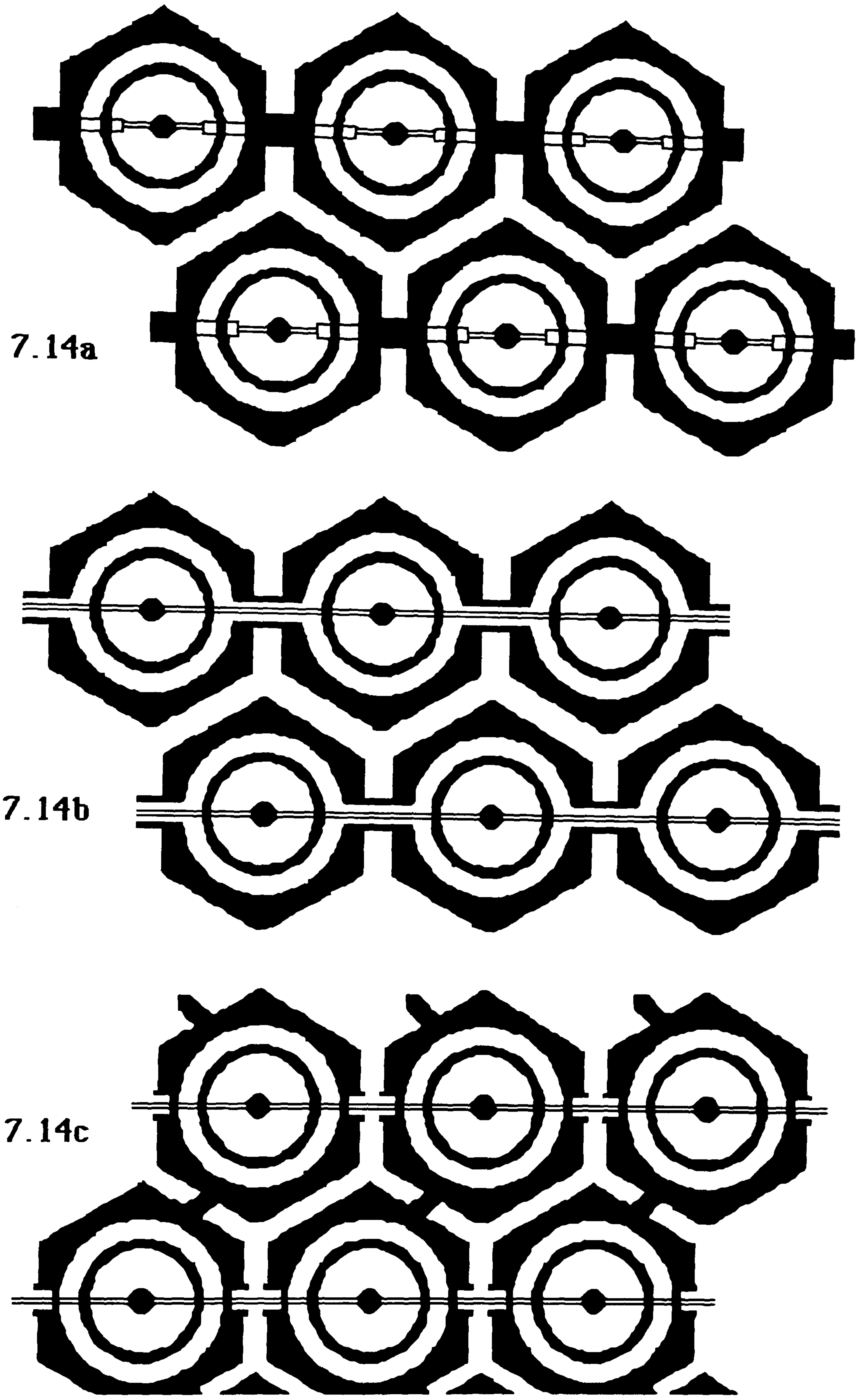

Figure 7.14: Schematic of the described microdot structures

7.8 Results with the new MDOTs

The following results have been obtained with the same set-up as that used previously. Again the wafers were mounted on the same PCBs as used in chapter 5 and a drift gap of 3mm was also used. Initially results from the 100 μm pitch detectors will be presented followed by some results from the 200 μm pitch structures. The explanation for this will be given in the next sections.

7.8.1 Gain measurements

The gain characteristics of the second batch of microdot detectors are investigated in the same way as described in section 7.3, i.e. with an x-ray emitting Fe^{55} source and with an 8 keV x-ray generator. Figure 7.15 shows the gain curves obtained with structure 9 which is a 100 μm pitch structure. The graph shows the variation in gain with cathode voltage for various mixtures of Ar:DME. Again the upper endpoints are determined by a current trip on the source measure unit, marking the onset of microdischarges or the creation of a punch through. An upper gain limit of ~45000 is achieved which is higher than anything previously obtained with a 100 μm pitch structure. The 70:30 Ar:DME curve can be compared to that in table 7.1 which shows

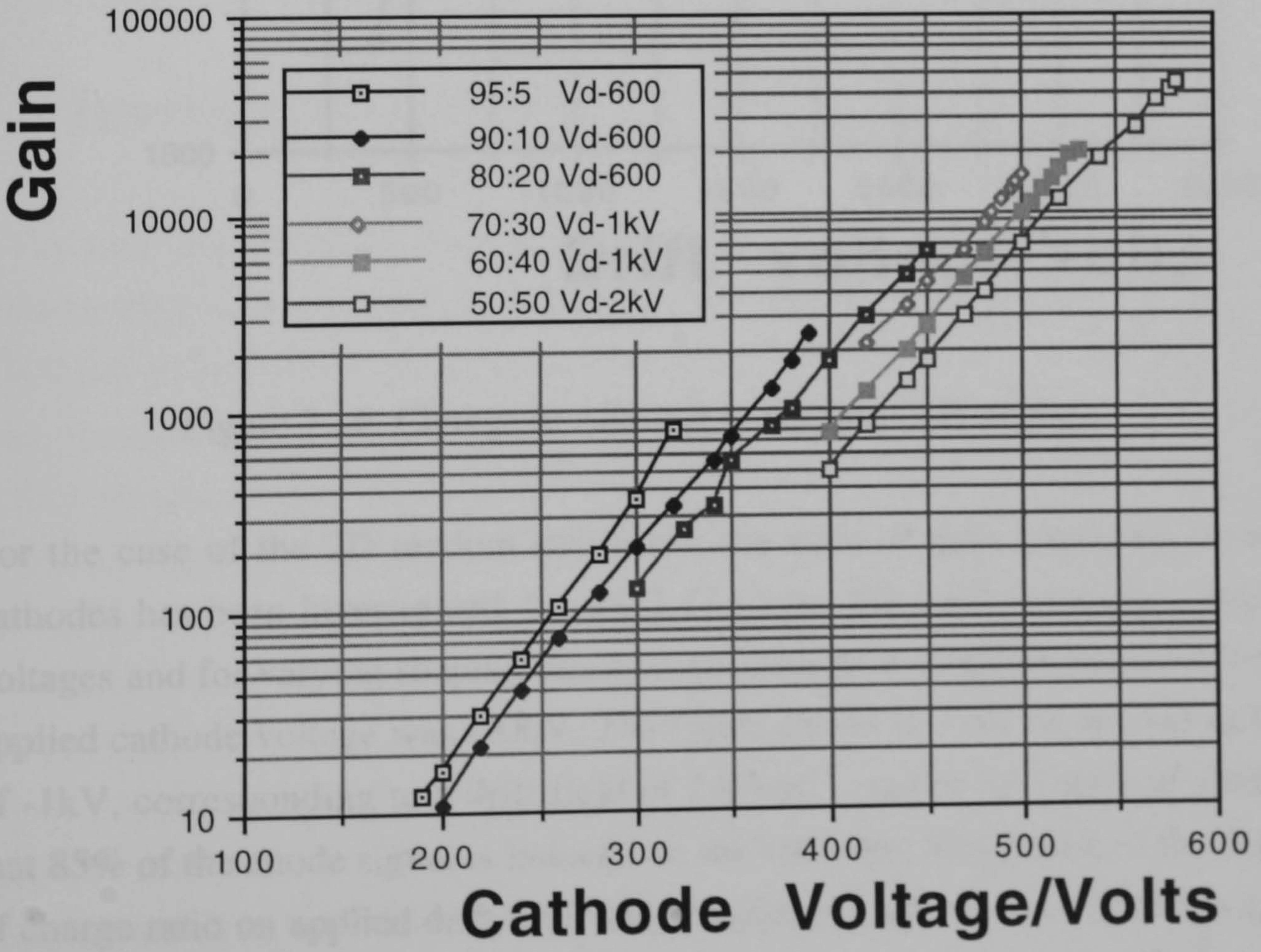

Figure 7.15: Gain curves obtained with batch 2 100 μm pitch microdot

that the gain obtained with the new batch of wafers is 50% higher than that with the old batch for the same cathode voltage. Such high gains should enable single photo electrons initiated by UV illumination of a photosensitive drift cathode to be detected. This will be investigated in section 7.9.

The problem of electron defocusing is seen in the first batch of detectors as illustrated in section 7.3.2. With the second batch of detectors, where the focusing is much better, such problems are not seen and gain from the drift region can be observed, see figure 7.16. The figure shows that as the drift plane voltage is increased from 400 to 2500 volts that the gain increases by 30% for a fixed cathode voltage.

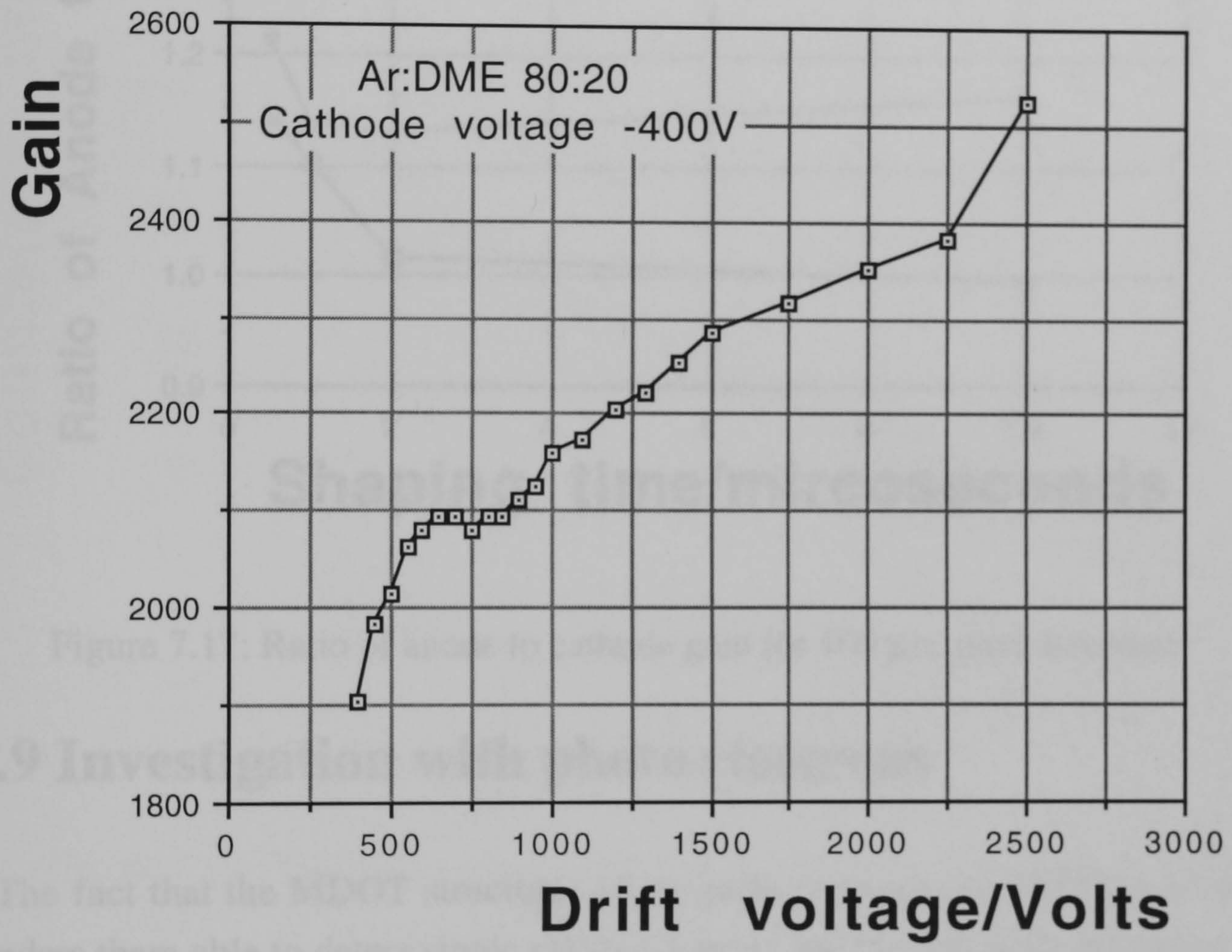

Figure 7.16: Change in gain due to varying drift voltage

For the case of the 2D readout structures, the ratio of gain measured on anodes to cathodes has been investigated. Figure 7.17 shows this ratio for various applied drift voltages and for varying shaping times on an Ortec post amplifier for structure 13. The applied cathode voltage was -400V. The figure shows that for an applied drift voltage of -1kV, corresponding to a drift field of $2\,kVcm^{-1}$, and at all values of shaping time that 85% of the anode signal is induced on the cathodes. Simulation of the dependence of charge ratio on applied drift field and integration time has been found to agree well with experimental results [6]. The change in ratio at integration times below 1.5 μS is caused by the slow rise time of the preamplifier due to capacitive loading caused by bussing a large number of the cathode strings into the preamplifier. When this effect is removed, the ratio is predicted to stay constant from 2μS to below 500nS.

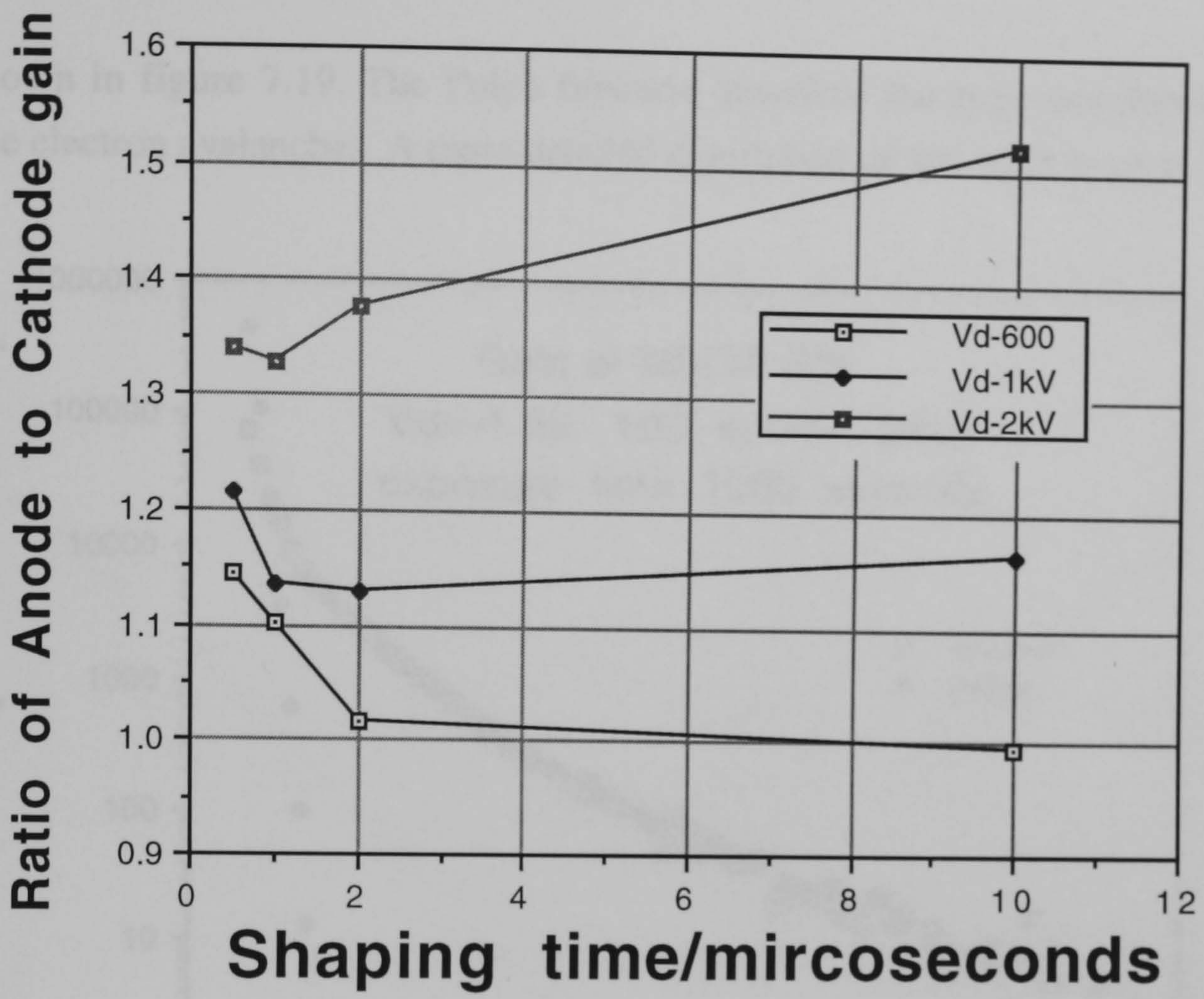

Figure 7.17: Ratio of anode to cathode gain for 100 μm pitch structure

7.9 Investigation with photo electrons

The fact that the MDOT structures allow gains in excess of 20000 to be sustained renders them able to detect single photo electrons and this has been investigated using a 100 μm pitch MDOT, in this case structure 13. For the following results the MDOT was operated between -510 and -560V with a drift voltage of -1300V. A UV lamp source was incident at an angle to the detector plane in order to extract photo electrons from the edge of the aluminium frame supporting the drift cathode. This non ideal geometry was forced due to the lack of a photosensitive drift cathode. Despite this problem, it was possible to measure about 30 pulses/second from electrons which diffused into the first row of microdots in the fringe field of the detector. Figure 7.18 shows a spectrum obtained at a gain of 30000. The spectrum was taken with a counting time of 1000 seconds. Then the electronic noise was background subtracted for the same period of time and the resulting spectrum plotted. The subtracted background is also shown for comparison. A Polya fit [7] to the spectrum which is defined as:

$$P(q) \cong \left[(1+\theta)\left({}^{q}\!\diagup_{q}\right)\right]^{\theta} e^{-(1+\theta)\left({}^{q}\!\diagup_{q}\right)}$$

is shown in figure 7.19. The Polya function describes the expected distribution for single electron avalanches. A more detailed description of this work is given in [8].

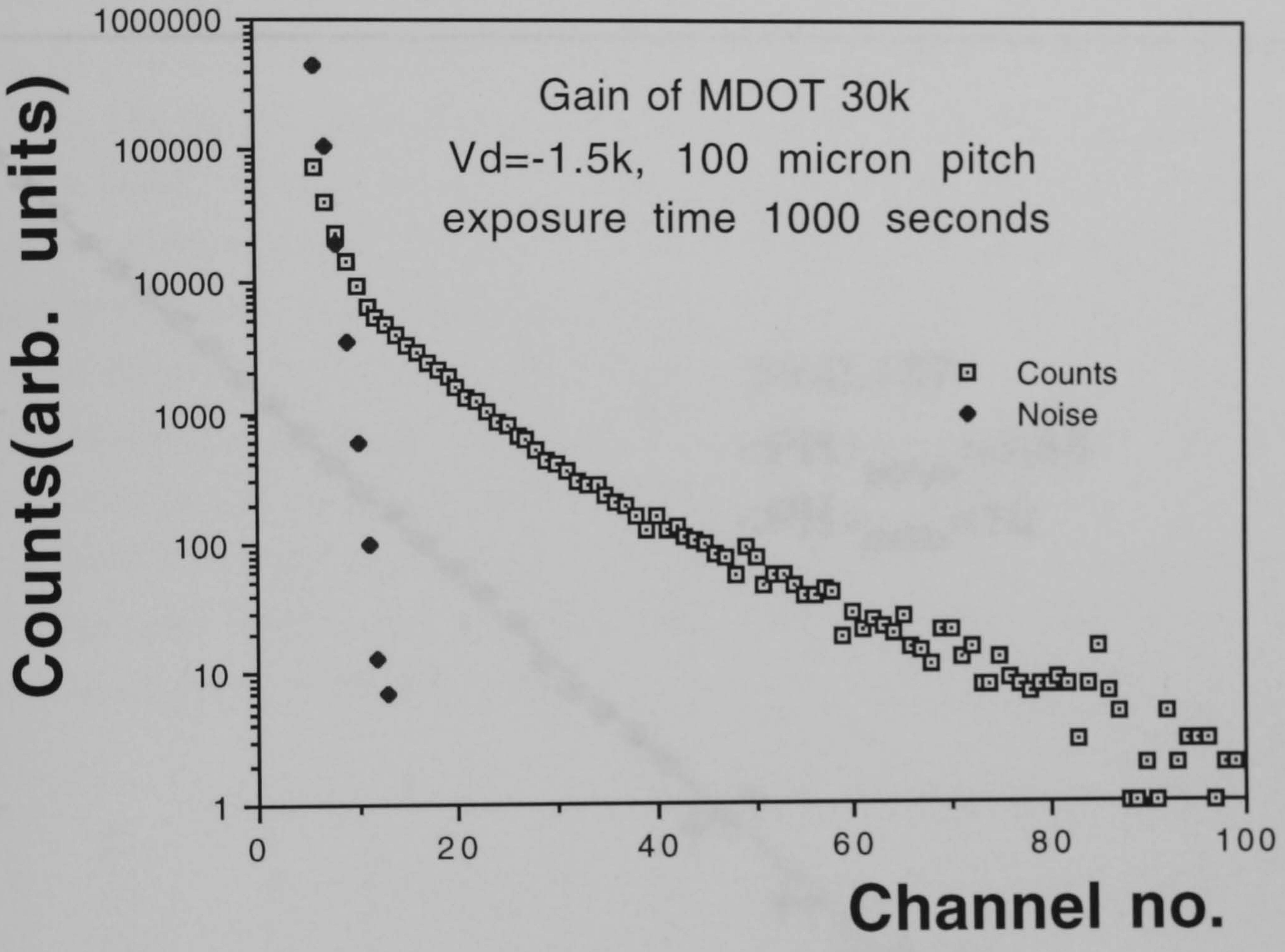

Figure 7.18: Photo electron spectrum obtained with MDOT at gain of 30000.

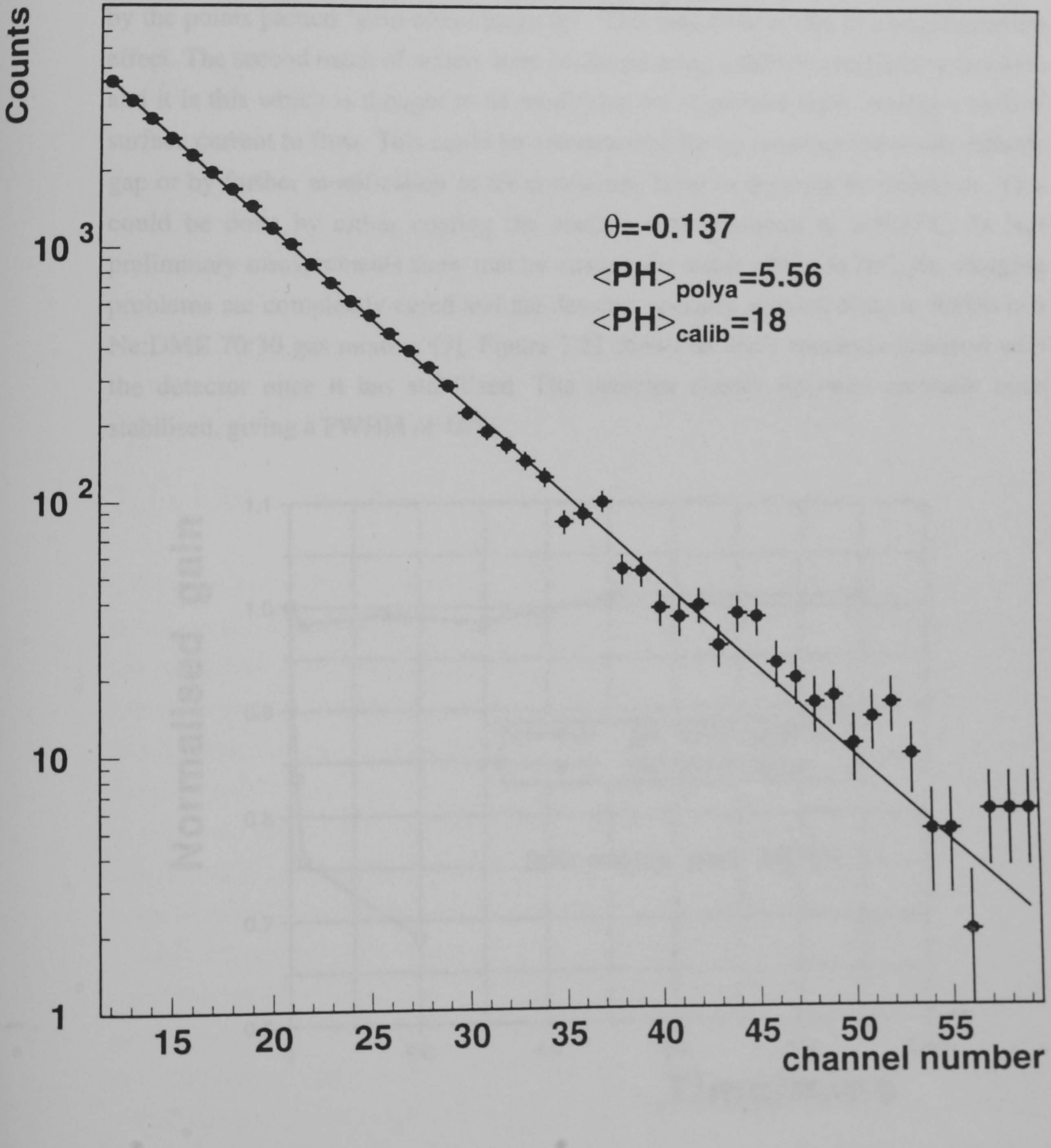

Figure 7.19: Polya fit to spectrum shown in figure 7.18

7.10 200 micron pitch structures

The behaviour of the 200 μm pitch structures in the second batch of wafers is drastically different to those in the first batch. Gains in excess of 50000 have been achieved but the substrate charges up rapidly, shown in figure 7.20. The figure shows that the gain drops rapidly (30% in 20 minutes). It then falls more slowly until reaching ~40% of its original value where it then stabilises. This is shown in the figure by the points plotted "gain after charge up". This behaviour is due to a manufacturing effect. The second batch of wafers were produced using a different implanting machine and it is this which is thought to be modifying the implanted layer causing a lack of surface current to flow. This could be compensated for by reducing the anode cathode gap or by further modification of the conducting layer to decrease its resistivity. This could be done by either coating the surface with diamond or a-Si:H:C. In fact preliminary measurements show that by coating the wafer with a-Si:H:C, the charging problems are completely cured and the detector operates at gains of up to 80000 in a Ne:DME 70:30 gas mixture [9]. Figure 7.21 shows an 8keV spectrum obtained with the detector once it has stabilised. The detector clearly operates normally once stabilised, giving a FWHM of 14%.

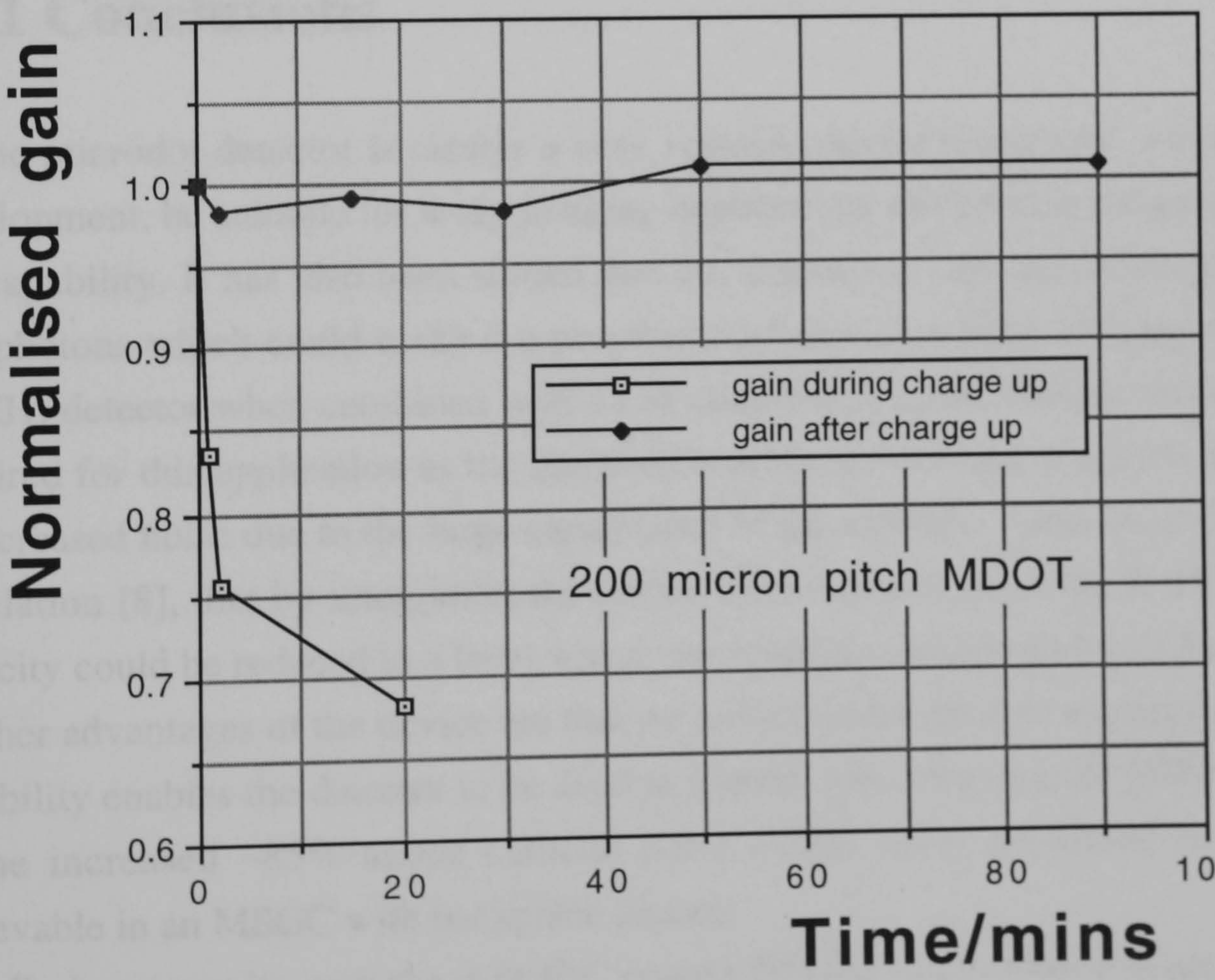

Figure 7.20: "Charge up" of the 200 μm pitch batch 2 microdots.

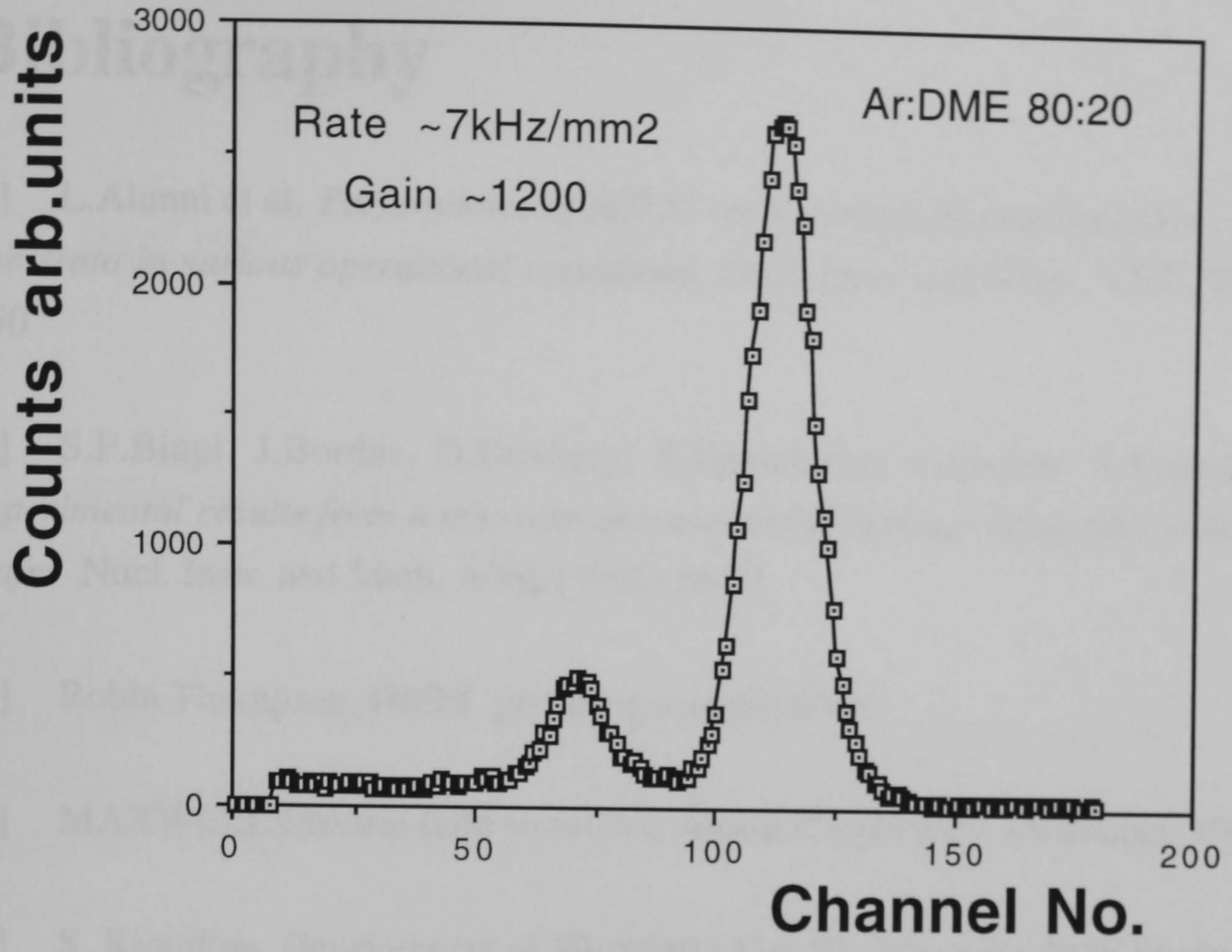

Figure 7.21: 8 keV spectrum obtained with batch 2 200 μm microdot, once the detector has 'charged up'.

7.11 Conclusions

The microdot detector is clearly a very versatile device that could, without further development, be suitable for x-ray imaging applications and particle tracking using the 2D capability. It has also been shown that the detector is capable of detecting single UV photons which could make it a possible candidate as a Ring Imaging Cherenkov (RICH) detector when combined with a CsI coated drift plane. Further work would be required for this application as the integration of the device onto a silicon wafer leads to increased noise due to the large capacitance of the cathode. It has been shown from simulation [8], that by integrating the device onto a quartz substrate that the cathode capacity could be reduced to a level where macroscopic cathode pads can be used.

Other advantages of the device are that no surface passivation is required and the 2D capability enables the detector to be used at a lower gain than in a 2D MSGC because of the increased ~85% anode cathode pulse height ratio, compared to the ~50% achievable in an MSGC with backplane pickup.

Preliminary results with the a-Si:H:C coated 200 μm pitch structures are extremely encouraging and make the prospect of a real time x-ray imaging device for medical imaging a true possibility.

Bibliography

[1] L.Alunni et al. *Performance of MSGC on electronically and ionically conductive substrata in various operational conditions* Nucl. Instr. and Meth. A348 (1994) 344-350

[2] S.F.Biagi, J.Bordas, D.Duxbury, E.Gabathuler, T.J.Jones, S.Kiourkos *First experimental results from a microdot gas avalanche detector integrated onto a silicon wafer* Nucl. Instr. and Meth. A366 (1995) 76-78

[3] Robin Thompson, HMEL private communication.

[4] MAXWELL Electric field simulator, Ansoft Corporation, Pittsburgh, USA.

[5] S. Kiourkos. *Development of Microstrip Gas Chambers for High Energy Physics Experiments* University of Liverpool, PhD thesis 1995.

[6] S.F.Biagi, J.Bordas, D.Duxbury, E.Gabathuler *Further experimental results of gas microdot detectors* Nucl. Instr. and Meth. A392 (1997) 131-134

[7] J.Va'vra Nucl. Instr. and Meth A371 (1996) 33-56.

[8] S.F.Biagi, T.J.V.Bowcock, D.Duxbury, E.Gabathuler *Observation of UV photons with a microdot chamber* Proceedings of the 5th International Conference on Advanced Technology and Particle Physics, Como to be published in Nucl. Instr. and Meth. A

[9] S.F.Biagi, D.Duxbury, E.Gabathuler in preparation.

Chapter 8

Conclusions

For a prospective detector to be considered for use at a synchrotron radiation source certain criteria should first be met. These were outlined in table 1.1. Work has been carried out on four such devices at the university of Liverpool and at the Daresbury laboratory. In the case of the microchannel plate coupled to the multiwire linear detector the results proved to be inconclusive and much more work is needed to evaluate such a device. The microstrip gas chamber and the microgap chamber have proved themselves to be very promising devices. These detectors have been found to possess some of the characteristics given in table 1.1 (see chapters 5 and 6) such as energy resolution <20%, position resolution of $\sim 240\mu m$ and a local count rate performance of $\sim 1\times 10^5 kHz / mm^2$. These measurements were carried out using a single anode readout system specifically designed for time resolved diffraction studies. Measurements taken by reading out a group of anodes have shown the local count rate performance to be $\sim 4MHz / mm^2$ with a variation in gain stability of ~4%, before space charge limitations come in to play where the gain is then reduced. Their response to irradiation has been shown to be uniform and linear over a dynamic range of 10^4. This was limited, along with the count rate performance, by the poor detection efficiency of these devices which is a consequence of having only a 3mm gas gap. This should improve by increasing the gas gap and/or by using a heavier gas such as xenon. The microgap detector has successfully obtained diffraction patterns of collagen from two different beamlines of the SRS but there exist further problems which will have to be solved before such devices can be routinely used. These include their physical size, 2D capability and the problems of ageing.

An exciting new detector, the microdot gas avalanche detector, which is intrinsically two dimensional has also been described and tested. This device whilst possessing all the benefits of the MSGC and MGAP detectors has various other characteristics which are advantageous. These include its inherent pixel like structure. The fact that the structure requires no passivation at the electrode ends enables the whole surface to be used, whereas for MSGCs there is a region of dead area. Also because there is no surface passivation, there is the possibility that the wafers can be cleaned using the same RF oxygen plasma that is used to remove the photoresist during the manufacture of the wafers. Plus the fact that the two dimensional structures enable the tiling together of wafers to form a larger detection area. As well as these advantages, if a discharge occurs in the detector, then only 1 anode dot or cathode ring will be damaged, whereas in the case of the MSGC or MGAP a single discharge will destroy a whole strip.

In conclusion, the exciting prospect of the microdot detector coupled with a readout system such as the recently commissioned RAPID system at Daresbury [1], would enable cutting edge experiments to be performed at the highest fluxes on the latest third generation synchrotron radiation sources.

Bibliography

[1] R.A.Lewis, C.J.Hall, W.Helsby, A.Jones, B.Parker, J.Sheldon. *A 10MHz photon counting detector system for time resolved x-ray diffraction* SPIE 2521 (1995) 290-300

Appendix 1

Chamber construction materials

The table below lists the various materials used in the chamber construction which are in contact with the gas. The components of the gas system are also given.

Component	Material	Comment
Electrodes	Aluminium	1.4 microns thick
Suppot, passivation	Thermal conductive epoxy	EPOTEK 905 [1]
Electrical contacts	Electrically conductive epoxy	EPOTEK 415 [1]
Gas container, window	Noryl, Mylar	window 50 micron
Window O-rings, PCB	Silicone rubber, fibreglass	
Drift plane	Aluminised polyester	50 micron thick
Drift plane spacers	Nylon screws, noryl spacers	
Mass flow meters	HI-TECH BRONKHORST	Vögltin [2]
Tubing	Polyurethane	FESTO PU-4 [3]
Gas Filter	Composition unknown	Nanochem [4]
Regulators, O-rings	Stainless steel, PTFE	

Table A1: Construction materials used for MSGCchamber and components of gas system. Noryl is the trade name for polyphenylene oxide, mylar for polyethylene terephthalate and PTFE for polytetrafluoroethylene.

[1] Epoxy Technology Inc., Billerica, MA, U.S.A.

[2] Vögltin Instruments Ag., Switzerland

[3] Festo PU-4, TÜV GERPÜFT

[4] Nanochem gas purification system, Hercules Inc., Wilmington, U.S.A.